

UiT

THE ARCTIC
UNIVERSITY
OF NORWAY

Faculty of Science and Technology
Department of Physics and Technology

Angular dependence of wide altitude ion line enhancements (WAILEs) during ionospheric heating at the EISCAT Tromsø Facility

—
Zoë Strimbeck Bazilchuk

FYS-3931 Master's thesis in Space Physics, June 2019



Abstract

This thesis presents the first sub-radar beam resolution determination of the angular width of wide altitude ion line enhancements (WAILEs), found to be 0.5 degrees around magnetic zenith, observed during a HF radio wave heating experiment at the EISCAT Tromsø Heating facility on 27 November 2014. The results of ray tracing simulations are detailed. The simulations are based on the hypothesis that WAILEs are caused by ducting of UHF radio waves due to artificial field aligned irregularities and the results of the experiment. Ducting of a 930 MHz radio wave was caused by 15.7% depletions from the background density in an IRI model atmosphere with $fO_2 = 10.04$ MHz. The data analysis and modelling methods used to achieve these results are explained. The fundamentals of HF radio wave interactions in plasma and the theory of incoherent scatter radar are discussed. The thesis concludes with recommendations for further research on WAILEs and field aligned irregularities caused by X-mode heating.

Acknowledgements

First and foremost I'd like to thank my wonderful supervisor, Prof. Björn Gustavsson, for suggesting this topic and thereby introducing me to such a fascinating little area of ionospheric science. Thanks for always having an open door, and for all of the great discussions and sage advice (some of which I even listened to).

I am lucky to have the best family anyone could ever ask for, so it wouldn't do to not thank them all in detail. Thanks to mom for the unconditional love, support, care packages full of baked goods, and the unparalleled proofreading services of Bazilchuk, Ink. Thanks to my sister, Molly for being an actual superhero and a wonderful cheerleader and coach throughout this process, and to my father, Rick for all of the academic tech support, goofyness, and nodding and smiling when I get excited about my work. Thanks to my partner, Endre, for being mental and moral support, a sounding board for my scientific woes, and for sending me puppy videos when I'm sad.

I might be feral and running around the local woods were it not for the support and commiseration of my fellow master's students, Rikke, Henriette, Tinna, Nina and Torbjørn. A special thanks is owed to Torbjørn for joining me on countless ridiculous trips down the rabbit hole in the throes of procrastination and for sharing my love of sticking googly eyes on stuff.

Lastly, a sincere and heartfelt apology is owed to the several acres of trees that were sacrificed for all the paper that was wasted in the writing of this thesis.

Contents

Abstract	iii
Acknowledgements	iv
List of figures	viii
List of tables	ix
List of abbreviations	x
1 Introduction	1
2 Theory	3
2.1 The Ionosphere	3
2.2 Plasma theory	6
2.2.1 Fundamentals of plasma physics	6
2.2.2 Electromagnetic waves in ionospheric plasma	7
2.3 Ionospheric heating	9
2.3.1 Electron heating mechanisms	10
2.3.2 Ionospheric effects of O-mode heating	11
2.3.3 Ionospheric effects of X-mode heating	12
2.3.4 WAILEs	12
3 Instruments and diagnostic methods	15
3.1 Incoherent scatter radar (ISR)	15
3.2 The EISCAT Ramfjordmoen instruments	16
3.3 Ionosondes/Dynasondes	17
3.4 SuperDARN	18
4 Experiment and Observations	19
4.1 Experiment details	19
4.2 Data analysis	22
4.3 Observed WAILEs	27
5 Results and analysis	29
5.1 Estimating WAILE characteristics	29
5.2 Deconvolution	39
5.3 Analysis of deconvolved data	42
5.4 Ray tracing	46

5.4.1	Simulation parameters	46
5.4.2	Results	47
6	Conclusions and outlook	53
6.1	Outlook and further work	53
A	Full results	55
A.1	Temperature observed and modelled data	55
A.2	Observed and modelled electron density at selected heights	58
A.3	Modelled growth, decay and time delay parameters	63
B	Programs written for this thesis	65
B.1	Matlab main file	65
B.2	Superimposed epoch analysis	68
B.3	Parameter optimization	72
B.4	Deconvolution	78
B.5	Ray tracing	80

List of Figures

2.1	Mid-latitude ionospheric profile	3
2.2	Ionospheric profile, Tromsø, 27.11.2014	4
2.3	Heater ray propagation at various launch angles.	9
3.1	IS spectrum sketch	16
3.2	Overview of EISCAT Tromsø facility	17
4.1	Plasma and upper hybrid frequencies, 27.11.2014	19
4.2	Tromsø Dynasonde measurement 11:32, 27.11.2014	20
4.3	Elevation scan pattern and heating cycles	21
4.4	Overview of GUIDAP-analyzed observations, 27.11.2014	21
4.5	Example overview of merged experimental observations	23
4.6	Merged electron density for 76.3 degrees	23
4.7	Merged electron density for 76.6 degrees	24
4.8	Merged electron density for 76.9 degrees	24
4.9	Merged electron density for 77.2 degrees	25
4.10	Merged electron density for 77.5 degrees	25
4.11	Merged electron density for 77.8 degrees	26
4.12	Merged electron density for 78.1 degrees	26
4.13	Merged electron density for 78.4 degrees	27
5.1	Example of model function	30
5.2	Modelled and observed data at individual heights	32
5.3	Observed and modelled data at each scan angle pt. 1	33
5.4	Observed and modelled data at each scan angle pt. 2	34
5.5	WAILE amplitude parameters	35
5.6	Example of modelled temperature	36
5.7	Modelled background densities	37
5.8	Example of growth and decay parameters	37
5.9	Histograms of residuals	38
5.10	Normalized modelled beam pattern within 2 degrees of boresight.	40
5.11	Deconvolved WAILE amplitudes	41
5.12	Deconvolved WAILE amplitudes at and above reflection height	42
5.13	Difference of deconvolved data	43
5.14	Snell's law	45
5.15	Plot of striation percentage sufficient to cause ducting at different f_oF2 values at 0.5° to the vertical scale of the striations.	47
5.16	ray tracing for $f_oF2 = 10.04$ MHz	48
5.17	ray tracing for $f_oF2 = 7.3$ MHz	49

5.18 ray tracing for $f_oF2 = 12$ MHz	50
5.19 ray tracing for $f_oF2 = 5$ MHz	51
A.1 observed and modelled temperatures	56
A.2 observed and modelled temperatures	57
A.3 76.3°	58
A.4 76.6°	59
A.5 76.8°	59
A.6 77.2°	60
A.7 77.5°	60
A.8 77.8°	61
A.9 78.1°	61
A.10 78.4°	62
A.11 Modelled pulse length, electron temperature data	63
A.12 Modelled pulse length, electron density data	63
A.13 Modelled growth and decay, electron temperature data	64
A.14 Modelled growth and decay, electron density data	64

List of Tables

4.1	List of ionospheric parameters and other values used during analysis .	22
5.1	Explanation of model function parameters	30
5.2	Standard deviation and angular width of WAILEs	44

List of abbreviations

AFAI	Artificially induced field-aligned irregularities
EISCAT	European Incoherent Scatter Scientific Association
HFIL	HF-induced ion line enhancements
HFPL	HF-induced plasma line enhancements
HF	High frequency
ISR	Incoherent scatter radar
MF	Medium frequency
OTSI	Oscillating two-stream instability
PDI	Parametric decay instability
RIOE	Radio induced optical emission
SEE	Stimulated electromagnetic emission
UHF	Ultra high frequency
UH	Upper hybrid (frequency, resonance height, ect)
VHF	Very high frequency
WAILEs	Wide altitude ion line enhancements

Chapter 1

Introduction

In 1901, G. Marconi successfully transmitted radio waves across the Atlantic ocean, thereby establishing the existence of the ionosphere as an atmospheric layer that reflects radio waves. Thirty-three years later, a Dutch electrical engineer found the Swiss radio signal he wanted to listen to rudely interrupted and intermingled with that of Radio Luxembourg [Tellegen, 1933], inadvertently discovering the fact that the ionosphere not only reflects radio waves, but causes complex nonlinear interactions between radio waves reflected in the same spot. In the 86 years between this remarkable discovery and now, multiple dedicated high-power HF radio wave research facilities have been built, and scientists have made numerous discoveries on the characteristics of the ionosphere and the manner in which radio waves and plasma interact [Stubbe, 1996a, Robinson, 1989].

Most ionospheric heating research uses HF radio waves of ordinary (O-mode) polarization, as this mode causes resonances that lead to significant modification of ionospheric plasma. Heating with extraordinary (X-mode) polarized radio waves has also become a topic of interest, as a number of ionospheric responses distinct from those produced by O-mode heating have been observed. Many of these responses are currently unexplained. Among these unexplained effects is a source of enhanced backscatter spanning a wide altitude range above the reflection height of the heater observed with the EISCAT Tromsø UHF incoherent scatter radar. This backscatter is known to have an angular width less than 1 degree in elevation from magnetic zenith [Senior et al., 2013], and is the topic of this thesis. An explanation for this phenomenon, suggested by [Rietveld and Senior, 2019] is that density striations known to be caused by HF radio wave heating [Kelley et al., 1995], [Blagoveshchenskaya et al., 2011b], [Blagoveshchenskaya et al., 2011a] cause sufficient changes to the refractive index for the EISCAT UHF radar beam to be ducted along the magnetic field, leading to the observed enhanced backscatter.

The objective of this master's project was to determine the angular width of the wide altitude ion line enhancements (WAILEs) observed during an ionospheric modification experiment at the EISCAT Heating facility on November 27th, 2014. According to the hypothesis that WAILEs are caused by ducting of the UHF radar beam, ray tracing simulations were run to determine the amplitude of depletions sufficient to cause ducting that matched the observed results. These simulations were extrapolated to other ionospheric conditions.

Ionospheric modification by HF radio wave heating is an interesting and useful ground-based method of studying the ionosphere, because it allows the ionosphere itself to be treated as a sort of in-situ plasma lab. This allows the study of the characteristics and composition of ionospheric plasma, how it reacts to changes in the geomagnetic field and how it interacts with radio waves. Few studies have examined ionospheric modification with X-mode radio waves. However, as has been the case with O-mode heating, a better understanding of the details of interactions that occur between this wave mode and the ionosphere will improve our understanding of plasma in the ionosphere, and help improve radio communication both on the ground and to space.

Chapter 2

Theory

This chapter provides the background knowledge necessary for understanding ionospheric heating and the experiments detailed in this thesis. It explains the fundamental causes and effects of ionospheric heating.

2.1 The Ionosphere

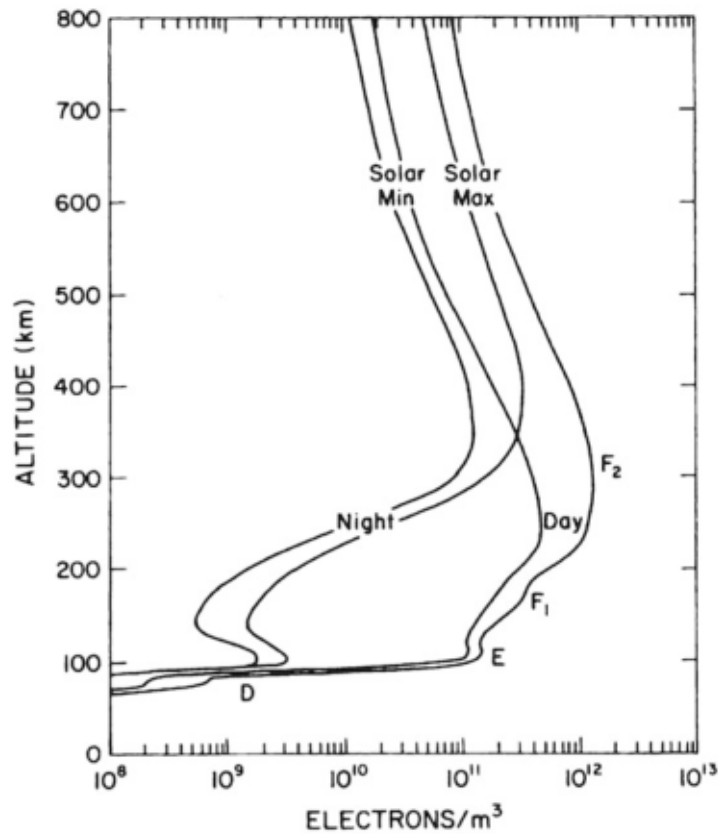


Figure 2.1: Typical ionospheric profiles at mid-latitude. From [Brekke, 2013]

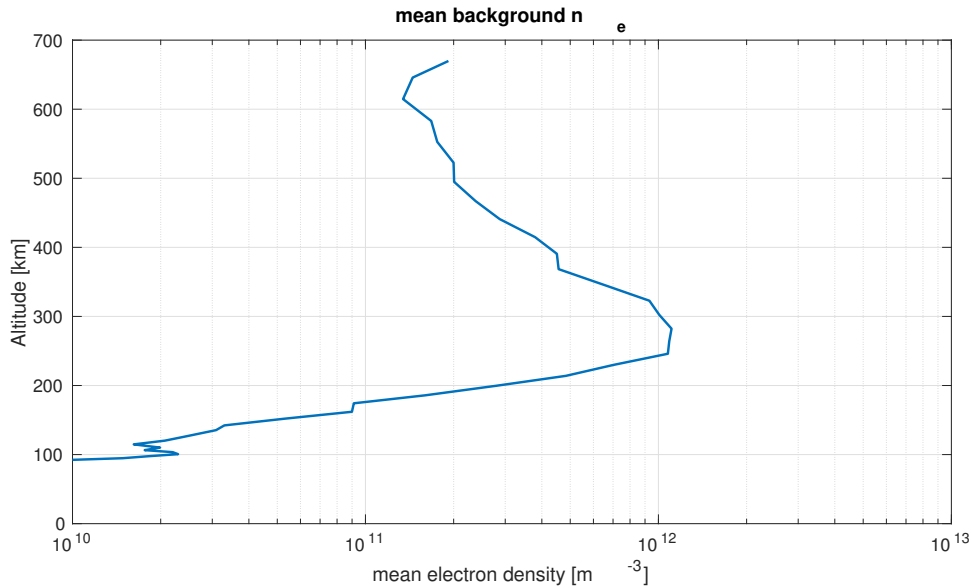


Figure 2.2: Background density for the ionosphere over Tromsø during the experiment

Researchers have known since the early 1900s that the upper portion of the atmosphere interacts with electromagnetic waves. This is because solar radiation propagating through the thermosphere and ionosphere ionizes sufficient amounts of atoms and molecules for the ionosphere to act as a plasma. The composition and characteristics of the ionospheric regions vary according to latitude and time of day due to photoionization rates and neutral densities. It generally spans 60-1000 km [Schunk and Nagy, 2009] and is divided into the D, E, F1 and F2 regions, characterized by differing chemical compositions and dominant ionization and loss processes. Following the description in [Schunk and Nagy, 2009]:

The F region is the uppermost region of the ionosphere, and is the region of interest for this thesis. It generally spans 150-1000 km. Chemical recombination rates in the F region ionosphere are very low, which makes it the ionospheric region of highest electron density. The chemistry of the F region ionosphere is simple, with O^+ being the only ion of any significant concentration. A distinct F1 region can be seen at mid-latitudes during the daytime. At high latitudes, such as over Tromsø, the F1 region is rarely seen as the ionosphere is coupled to the magnetospheric tail and is therefore more variable due to the higher energies of precipitating particles.

The E region spans 90-150 km. Although it is subject to the highest photoionization rates in the atmosphere, the electron density is lower than the F region due to more complex chemistry with higher chemical recombination rates of two species of dominant molecular ions, NO^+ , O_2^+ . The E region remains distinct during the nighttime, although with significantly lower charged particle densities than during the daytime, unless in the case of auroral precipitation.

The D region is the lowest region of the ionosphere, spanning 60-90 km. Some of the energy of MF and HF radio waves is absorbed by D region plasma due to the high collision rates on this region. For good F region ionospheric heating

conditions, it is therefore important to have low charged particle densities in the D region, and thus low D region absorption. The chemistry of this region is very complex, with both positive and negative molecular ions at significant densities. The collision rates and recombination rates are very high, and photoionization rates are low, meaning that it is only distinct during the daytime.

2.2 Plasma theory

2.2.1 Fundamentals of plasma physics

The following section presents the basic concepts of plasma physics necessary for understanding the manner in which ionospheric plasma will interact with radio waves. It then describes the fundamentals of these interactions.

A plasma can be defined as a *quasineutral gas of charged and neutral particles which exhibits collective behavior* [Chen, 2006]. Defining these terms, quasineutrality is when the distribution of positive and negative charges on a macroscopic level is approximately equal [Inan and Golkowski, 2010], i.e. globally, $N_e = N_i$, and local deviations from this are small. Collective behavior is the set of wave modes that occur in a plasma. For these to occur, quasineutrality and the following conditions on charge densities, length scale and collision frequency need to be fulfilled [Chen, 2006]:

$$\lambda_D \ll L \quad (2.1a)$$

$$N_D \gg 1 \quad (2.1b)$$

$$\omega_{pe} \cdot \tau > 1 \quad (2.1c)$$

where L is the length scale of the plasma, ω_p is the plasma frequency, τ is time between collisions, and λ_D, N_D are the length scale and number of charges in a Debye sphere, which is the scale of the electrical potential shielding in the presence of an external electric field. All of this essentially means that a plasma must be a gas with a significant density of charged particles distributed over an volume such that the mean free path allows oscillations to take place.

One of the central traits of a plasma is that it will have a macroscopic response to electromagnetic fields. If the electrons in a cold, unmagnetized plasma are displaced relative to the ions, restoring forces will lead to the electron oscillating with frequency [Chen, 2006]:

$$\omega_p = \sqrt{\frac{n_e q_e^2}{\epsilon_0 m_e}} \quad (2.2)$$

These oscillations are electrostatic, meaning that they only cause a fluctuating electric field. In warm plasmas, this same displacement leads to propagating Langmuir waves with dispersion relation [Chen, 2006]:

$$\omega^2 = \omega_p^2 + 3k^2 \frac{KT_e}{m} \quad (2.3)$$

which has a cutoff at ω_p . In the case of a magnetized plasma, there is also an electrostatic wave mode with a cutoff at [Schunk and Nagy, 2009]:

$$\omega_h = \omega_p^2 + \omega_c^2 \quad (2.4)$$

where ω_p is the aforementioned plasma frequency, and ω_c is the electron gyrofrequency. Similar wave modes arise for ions as well, known as the ion acoustic and lower hybrid frequencies. However, because ions are much heavier than electrons, these frequencies are much lower. Therefore, ions are considered to be stationary to the first order relative to electrons for plasma interactions with HF radio waves, because the plasma frequencies of typical ionospheric plasmas are in the HF range.

Single particle motion is governed by the momentum equation [Inan and Gołkowski, 2010]:

$$\frac{d\mathbf{v}}{dt} = q(\mathbf{E} + \mathbf{v} \times \mathbf{B}) \quad (2.5)$$

Considering a single electron in a static, uniform B-field, this reduces to $m \frac{d\mathbf{v}}{dt} = q\mathbf{v} \times \mathbf{B}$. Solving this DE shows that an electron will gyrate with electron gyrofrequency [Inan and Gołkowski, 2010]:

$$\omega_c = \frac{q_e \mathbf{B}}{m_e} \quad (2.6)$$

2.2.2 Electromagnetic waves in ionospheric plasma

In order to understand the effects of HF radio wave heating it is necessary to know the propagation of electromagnetic waves in plasma. In general, waves in a nonmagnetized plasma will be reflected when the frequency of the transmitted wave matches the ambient plasma frequency, $\omega = \omega_p$. Although the ionosphere is a magnetized plasma, it is nonetheless important to note that in general, waves with a frequency below the peak plasma frequency of the ionosphere, $f_O F2$, will be reflected by the ionosphere [Inan and Gołkowski, 2010].

The waves transmitted from heating facilities can be linearly or circularly polarized. The fundamental wave modes in a magnetized plasma are left- and right-hand circularly polarized, so the propagation of these modes is important. One method of examining their propagation at an arbitrary angle θ , following the explanation in [Davies, 1990], is to use the Appleton-Hartree equation, which describes the refractive index of a radio wave with frequency ω at an angle to the background field a magnetized plasma:

$$n^2 = 1 - \frac{\omega_p^2/\omega^2}{1 - \frac{\omega_c^2 \sin^2 \theta}{2(\omega - \omega_p^2)} \pm \left[\left(\frac{\omega_c^2 \sin^2 \theta}{2(\omega^2 - \omega_p^2)} \right)^2 + \frac{\omega_c^2}{\omega^2} \cos^2 \theta \right]^{1/2}} \quad (2.7)$$

The Tromsø Heating facility is at high latitude, so the radio waves are transmitted at small angles to the geomagnetic field, B_0 . This allows $\sin \theta \approx 0$, $\cos \theta \approx 1$, to be

approximated, which gives the quasi-longitudinal (QL) approximation of equation 2.7:

$$n^2 = 1 - \frac{X}{1 \pm Y} \quad (2.8)$$

where $X = \frac{\omega_p^2}{\omega^2}$ and $Y = \frac{\omega_c}{\omega}$. The heating wave will be reflected where $n = 0$, so according to 2.8 this should be when $X = 1 \pm Y$. This is the case for left-hand polarized extraordinary (X-mode) waves where Y is negative (since the left-handed polarization oscillates opposite to electron motion). However, because the right-hand polarized ordinary (O-mode) wave nears the height where $\omega = \omega_p$, the magnetic field causes the wave to bend to the point where it becomes quasi-transverse to the geomagnetic field, in which case the quasi-transverse approximation (QT) is:

$$n^2 = 1 - X \quad (2.9)$$

and the wave is reflected at $X = 1$, that is $\omega = \omega_p$, so the O-mode wave is reflected at the same height as waves in nonmagnetized plasma (hence the name). If the O-mode wave is exactly parallel to the background magnetic field near the reflection height, the previously explained refraction will not occur and the wave will continue to propagate to the height where $X = 1 + Y$. This propagation is known as Z-mode.

Waves launched away from vertical propagate at an angle to the refractive index gradient, causing them to gradually refract as they propagate upwards. As the refractive index decreases with higher plasma frequency (and thus altitude), the gradient means that the wave phase speed will be higher at higher altitudes, and the wave will tend to refract away from zenith before reaching the true reflection height. This occurs for waves propagating outside the 'spitze' cone of angles around zenith, where the wave will still reach $X = 1$. This range of angles is given by:

$$\sin \phi_c = \sqrt{\frac{Y}{1 + Y}} \cos I \quad (2.10)$$

where I is magnetic dip angle (approx 77.5° for Tromsø). The spitze angle varies between 6 - 8 degrees in Tromsø, depending on the heater frequency.

As an EM heater wave approaches reflection height, its group velocity goes to zero. Because Poynting flux is generally conserved (except due to absorption and beam widening, which are both small effects), the wave electric field will increase [Bryers et al., 2013]. When the wave electric field becomes large enough, non-linear effects dominate wave-plasma interactions, leading to excitation of various plasma waves and turbulence. This coupling can occur for Langmuir and ion acoustic waves at the reflection height of the heating wave, as well as with upper hybrid waves at the height where $\omega^2 = \omega_p^2 + \omega_c^2$, the upper hybrid resonance height. Coupling maximizes when the HF wave electric field is perpendicular to

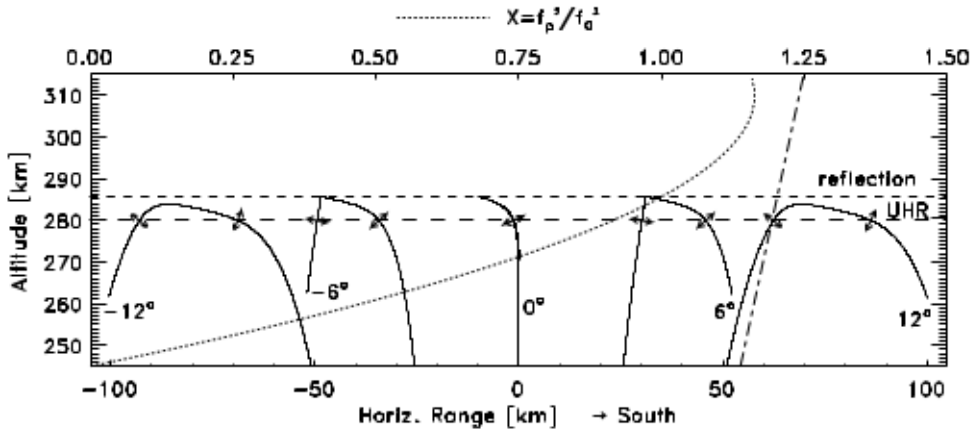


Figure 2.3: Ray tracing of O-mode heater waves for various aspect angles. The direction of the wave electric field at UH resonance height is indicated by the arrows. From [Rietveld et al., 2003].

the background magnetic field [Stocker et al., 1992], but will only happen for O-mode waves, as X-mode waves will be reflected below the height where frequencies match.

2.3 Ionospheric heating

The science of ionospheric modification by high power radio waves, or heating, was born in the 1930s when a Dutch electrical engineer discovered mixing between a Swiss radio station in Beromunster and an intruding signal from Luxembourg [Tellegen, 1933]. The ionosphere had previously been believed to be a hard mirror for electromagnetic radio waves, but this effect, later dubbed the Luxembourg effect, or ionospheric cross-modulation, [Huxley and Ratcliffe, 1949] showed that nonlinear effects occur at the reflection height of radio waves. Since this discovery, several dedicated research facilities aimed at studying the characteristics of ionospheric plasma, as well as for the study of nonlinear plasma phenomena [Stubbe, 1996b] have been constructed.

As outlined in the previous section, HF radio waves will generally be reflected by plasma of the same plasma frequency, or by frequencies close to this. Equation 2.2 shows that the plasma frequency is proportional to the square root of the electron density of the plasma, so the height at which a radio wave will be reflected is dependent on the electron density profile. The highest frequency radio wave that can be reflected by the ionosphere is determined by the peak electron density in the ionosphere. This is in the F2 region, generally at around 250 - 300 km, and the frequency corresponding to this height is referred to as f_oF2 [Schunk and Nagy, 2009]. In cases where the heater frequency is below f_oF2 , the ionosphere is termed overdense. During heating in overdense conditions, the heater waves will be reflected or to a certain extent absorbed, and resonant heating can occur [Bryers et al., 2013]. Conversely, if the ionosphere is such that the heater frequency is above the F2 critical frequency, it is termed underdense, and

only collisional heating should occur.

2.3.1 Electron heating mechanisms

Heating of ionospheric electrons by radio waves occurs by two mechanisms. Heating rates are dependent on the heating wave frequency, polarization and power, while cooling rates depend on the reflection height of the heating wave, and the subsequent density and conductivity [Gustavsson et al., 2010].

Collisional heating

Electrons are accelerated and decelerated by the electric field of the pump wave. In the absence of collisions, this motion is ordered and the induced current will be 90° out of phase with the wave electric field, and no wave energy is transferred. When collisions occur, electron motion is randomized and the current will be phase shifted, having a component in phase with the wave electric field, causing wave energy dissipation to electrons, or collisional heating [Shoucri et al., 1984]. This process is independent of resonance, and therefore occurs for both X- and O-mode heating, as well as for both underdense and overdense ionospheres. A detailed study and model of collisional heating for an underdense atmosphere is presented in [Gustavsson et al., 2010], which reported temperature increases up to 800k above background. Collisional heating makes up approximately 25% of the electron temperature increase during O-mode heating [Bryers et al., 2013], but should be the only source of temperature enhancement during X-mode heating. Collisional heating will be slightly more efficient for X-mode heating, as a significant amount of the pump power for O-mode heating is lost in resonant processes [Bryers et al., 2013].

Resonant heating

The other mechanism of electron heating occurs as a result of upper hybrid resonance, which will be referred to in this thesis as resonant heating. Based on [Bryers et al., 2013]: when coupling occurs between the heater wave and upper hybrid waves, the upper hybrid waves can become trapped in density depletions, leading to focusing of heater waves and increased excitation of UH-waves, which further expand the depletions. This feedback loop leads to efficient energy dissipation from heater waves to ambient electrons, because they have a low group velocity and propagate perpendicular to the background magnetic field. Since this occurs at the upper hybrid resonant height, only O-mode waves should be able to cause resonant heating, as X-mode waves are reflected below this height. Coupling maximizes when the heater wave electric field is perpendicular to the background magnetic field [Rietveld et al., 2003] (see figure 2.3 for an example of this geometry). Resonant heating also shows some dependence on frequency, with minima occurring near harmonics above the 2nd gyroharmonic [Rietveld et al., 2003]. [Bryers et al., 2013] present a comparison of the effects of resonant and collisional

heating, finding that resonant processes account for 2-5 times more electron heating than collisional heating.

2.3.2 Ionospheric effects of O-mode heating

The coupling of heater waves to upper hybrid and Langmuir waves at the UH resonance and reflection heights leads to a number of interesting phenomena. Based on the explanation in [Rietveld et al., 1993]:

Coupling between the heater wave and plasma wave modes near the heater reflection height leads to the parametric decay instability (PDI) and oscillating two stream instability (OTSI). The former results in the production of a Langmuir and an ion acoustic wave, which are measured by incoherent scatter radar as enhanced ion and plasma lines (HFIL and HFPL). The latter also produces a Langmuir wave, but the second decay product is a non-propagating periodic structure that manifests in incoherent scatter data as an echo offset from the radar frequency and an ion line peak at zero frequency.

Stimulated electromagnetic emissions (SEE) are the result of upper hybrid and Langmuir waves generated during heating that scatter off electrostatic waves and convert to HF electromagnetic waves [Rietveld et al., 1993]. The frequency shift of these emitted waves is characteristic of the relation between the heater frequency and local gyroharmonics. A number of different SEE effects can be observed at different pump frequencies and gyroharmonics, which are discussed in detail in [Thidé et al., 1983, Leyser, 2001].

Radio induced optical emissions (RIOE, or artificial aurora) are caused by electrons that are accelerated to several eV. These accelerated electrons eventually emit primarily at 6300\AA and to a lesser extent 5577\AA and other emissions with higher excitation thresholds [Gustavsson and Eliasson, 2008], depending on the reflection height and power of the heater.

Ionospheric heating can also induce or amplify density irregularities (artificially induced field-aligned irregularities, AFAI) [Rietveld et al., 1993, Blagoveshchenskaya et al., 2011b, Kelley et al., 1995] by coupling of heater waves to upper hybrid waves at the upper hybrid resonance height. The resulting resonant heating at this height leads to pressure gradient forces generate or enhance field aligned density irregularities, generally on the scale of meters to tens of meters across the magnetic field, tens of km along the magnetic field, and depletions up to 12% [Kelley et al., 1995].

Thermal self focusing [Rietveld et al., 1993, Gurevich et al., 2002] can also be the cause of density irregularities. Initially small density fluctuations refract heater waves, leading to focusing of the beam and focused heating in the region of the irregularity. Collisional heating and ponderomotive forces lead to an increased plasma pressure in the density depletions, expelling plasma from the focused region and causing the perturbation to grow [Gurevich et al., 2002].

2.3.3 Ionospheric effects of X-mode heating

All of the effects explained in the previous section occur due to coupling of heater waves with ambient plasma waves, which, as has been discussed, should not happen during X-mode heating. The only significant effect that should be observed during heating in X-mode should be collisional electron heating. However, [Blagoveshchenskaya et al., 2018], [Blagoveshchenskaya et al., 2014], [Blagoveshchenskaya et al., 2011b], [Blagoveshchenskaya et al., 2011a], [Senior et al., 2013] present evidence of AFAI, RIOE, and possibly SEE occurring during X-mode heating. [Blagoveshchenskaya et al., 2018] show evidence of HFIL/HFPL during X-mode heating, although it seems that this may be due to O-mode leakage, as is seen in [Senior et al., 2013]. Note that [Blagoveshchenskaya et al., 2018] does not discuss O-mode leakage as a possible cause of their results. Some work has been done to characterize the growth and decay times of AFAI observed during X-mode heating [Blagoveshchenskaya et al., 2011b, Blagoveshchenskaya et al., 2011a], finding that these striations occur at a frequency range between $f_{\text{O}}F2$ and up to 1 MHz above $f_X F2$ [Blagoveshchenskaya et al., 2018], and with growth times of 1-3 minutes and relaxation times of 20-30 minutes [Blagoveshchenskaya et al., 2011a]. It has been theorized that these AFAI may be caused by thermal self-focusing [Blagoveshchenskaya et al., 2011b], although there is no conclusive explanation for the causes of all of the observed effects, and the body of research is quite limited.

2.3.4 WAILEs

It is briefly noted in [Blagoveshchenskaya et al., 2011b], [Blagoveshchenskaya et al., 2011a] that they observed apparent electron density enhancements during their experiments at a wide altitude extent above the reflection height of the heater. These apparent enhancements are limited to experiments where the EISCAT UHF radar is oriented along the magnetic field (approximately 77.5 degrees), and are seen primarily during X-mode experiments, but can also be seen during O-mode heating for experiments with pulses of alternating polarization, as presented later in this thesis (a nice example of this is also seen in figure 4 of [Blagoveshchenskaya et al., 2018], although it is not commented on). [Senior et al., 2013] examined these wide altitude extent ion line enhancements (WAILEs) further, showing that the effect occurs only within a small angular range around magnetic zenith. They also observed that the apparent density enhancements were not accompanied by a corresponding shift of the plasma line frequency, and that the tristatic receivers in Sodankylä and Kiruna did not observe the any enhancements at all, effectively proving that this cannot be an actual density enhancement, but rather some unknown source of enhanced radar backscatter.

The current hypothesis regarding the cause of WAILEs is that AFAIs generated during X-mode heating modify the refractive index enough to cause critical or total internal refraction of the EISCAT UHF radar beam. This would happen at an incident angle $\theta \leq \sin^{-1} \frac{n_2}{n_1}$ (from Snell's law), where n_1 and n_2 are the refractive indexes on either side of the interface of a density striation. This thesis

estimates the range of angles at which WAILEs are observed during a specific heating experiment, and uses this to calculate the amplitude of the corresponding AFAIs.

Chapter 3

Instruments and diagnostic methods

This chapter explains the different diagnostic instruments used during heating experiments, and discusses the capabilities of each instrument as they relate to heating experiments. It also provides a brief overview of the physics of incoherent scatter radar and the technical specifications of the EISCAT Tromsø facility.

3.1 Incoherent scatter radar (ISR)

This section is based on the description of incoherent scatter radar in [Schunk and Nagy, 2009, Bjørnå, 2005]. So far the discussion has focused on the interactions between radio waves and plasma with frequencies close to the local plasma frequency. Radio waves of much higher frequency than ionospheric plasma will not be reflected or directly excite plasma turbulence. However, a small fraction of the wave energy will be *scattered* by irregularities in the plasma, which turns out to be a very useful property for studying the ionosphere.

Incoherent scatter radars work by transmitting VHF or UHF radio waves into the atmosphere. Although these waves are of frequencies high enough to propagate through the ionosphere, density fluctuations and plasma waves will still scatter part of the wave energy, with electrons acting as the actual scatterers. The subsequent received signal will be an incoherent addition of coherent backscatter from multiple "wavelets" of these plasma modes. This process is known as incoherent scatter because it was first assumed that electrons would act as individual stochastic scatterers, with the influence of plasma wave not being considered. Although this is not the dominant scattering mechanism, the name stuck.

A commonly used method of analyzing the received signal from an incoherent scatter radar is to autocorrelate the signal, which provides a power density spectrum (PDS) of a characteristic shape and contains information about characteristics of the plasma in the scattering volume. In basic terms, the power of the returned signal is proportional to the electron density, so this parameter can be found by integrating the received PDS over all frequencies. However, any other

cause of increased backscatter may also be naively interpreted (at least initially) as electron density enhancements, as in the case for WAILEs, the topic of this thesis. The height of the 'shoulders' of the ion spectrum compared to the central 'valley' provides information about the ratio between the electron and ion temperatures, and ion temperatures can be determined from the width of the ion line. The ion drift velocity is given by the Doppler shift, i.e. the ion spectrum frequency offset from zero. The plasma lines, when detected, provide information about the plasma waves in the scattered volume, and also provide independent information about the electron density [Senior et al., 2013]. Data from the EISCAT radars is analyzed using the GUIDAP software [Lehtinen and Huuskonen, 1996] with the assumption that standard incoherent scatter theory accurately describes the scattering volume.

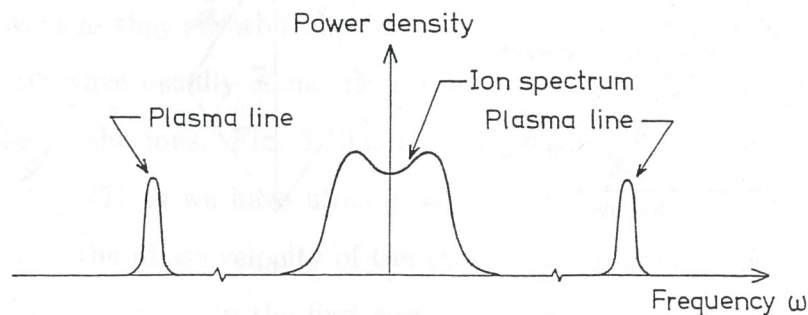


Figure 3.1: Sketch of incoherent scatter spectrum. from [Bjørnå, 2005] showing the general shape of the ion and plasma lines.

When measuring with an incoherent scatter radar, the time delay between a transmitted pulse and received signal will determine the altitude at which the scattering occurs. This allows an altitude profile to be constructed with different range increments corresponding to subsequent time steps between samples. However, this limits the range resolution to the length of each pulse. This problem is solved by transmitting long pulses, but alternating the phase of the transmission into subpulses [Lehtinen and Häggström, 1987]. Each range gate will therefore be distinguished after one full radar cycle by phase and lag. Although shorter sub-pulses allow for higher range resolution, they will subsequently decrease the signal-to-noise ratio.

3.2 The EISCAT Ramfjordmoen instruments

The EISCAT Heating facility [Rietveld et al., 1993], [Rietveld et al., 2016] is located at Ramfjordmoen (69.6°N, 19.2°E, L = 6.2), on the same site as the EISCAT UHF and VHF incoherent scatter radars, as well as a number of other ionospheric research instruments. The Heating facility consists of three arrays, and is capable of transmitting between 4-8 MHz with a maximum effective radiated power (ERP) of 300 MW. The transmitted beam can be steered in the north-south direction by varying transmitter phases. Arrays 2 and 3 can be steered about $\pm 30^\circ$ from zenith, while array 1 is limited to about 20° .

The EISCAT UHF incoherent scatter radar, fully described in [Rishbeth and Van Eyken, 1993], is located on the same site as the heating facility. The antenna is a fully steerable 32m parabolic dish operating at 930MHz. The EISCAT radars have a number of standard experiments that can be run with different sampling rates, time resolution, and for different altitude coverage, all of which are fully described in [Tjulin, 2015]. Two identical receiving antenna are located at remote sites in Kiruna, Sweden and Sodankylä, Finland. These receivers ceased operation at 930 MHz in 2011 [Senior et al., 2013], meaning that the UHF radar currently is monostatic. One of the experiments discussed in this paper was done prior to 2011, when the tristatic radar was still operating at 930 MHz.

Among the various other instruments located at the EISCAT Ramfjordmoen site is a dynasonde which typically operates at 1-12 MHz with a normal peak power of 10 kW, range resolution around 0.1 km and a typical sweep time of 3 minutes, although it is fully programmable [Rietveld et al., 2008].

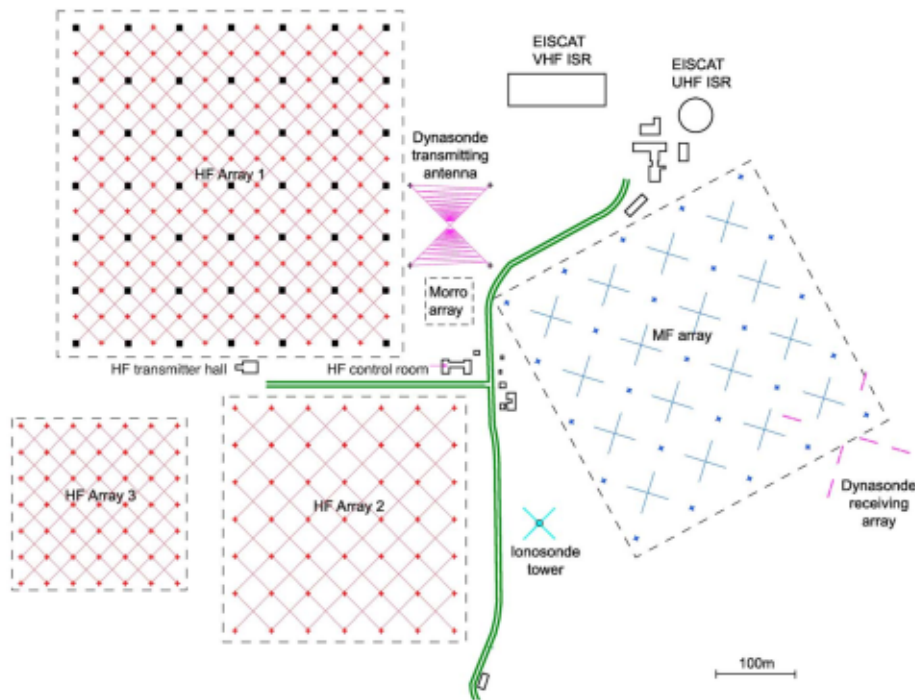


Figure 3.2: Overview of the EISCAT Tromsø site. From [Rietveld et al., 2016]

3.3 Ionosondes/Dynasondes

Dynasondes are another type of diagnostic instrument for ionospheric plasma. A dynasonde operates on the previously described principle that HF radio waves will be reflected by a plasma of the same frequency. An accurate profile of the ionosphere in terms of plasma frequency can be constructed by sending out pulses over a range of frequencies and measuring the time delay before the reflected signal returns [Schunk and Nagy, 2009]. This is important to ensure correct calibration

of ISR measurements, because the electron density profile is used to find the correct scaling factor for the ISR power-to-density conversion. Having an accurate density profile is also important in determining appropriate heater frequencies at any given time. The power of the received signal also provides information about D-region absorption. Dynasondes can be used as a diagnostic tool for the ionosphere in their own right, but are limited in that they will only provide data for the ionosphere up to FOf2, but not above [Rietveld et al., 2008].

3.4 SuperDARN

The Super Dual Auroral Network is a network of Doppler backscatter radars in the northern and southern polar hemispheres. A single Doppler backscatter radar is able to detect ionospheric density irregularities as regions of enhanced backscatter at the length scale of $L = \lambda/2$. Specifically, the SuperDARN network radar located in Hankasalmi, Finland has Tromsø in its field of view, and has, in a number of studies [Blagoveshchenskaya et al., 2011a, Blagoveshchenskaya et al., 2011b, Blagoveshchenskaya et al., 2018] been used to study AFAIs caused by X-mode heating in Tromsø. The radar operates at frequencies between 8-22MHz, with 16 beams at an azimuthal separation of 3.24° . The radar network as a whole allows for a number of different polar magnetospheric processes to be measured, such as the structure and dynamics of global convection, MHD waves and substorm evolution, all of which are detailed in [Chisham et al., 2007].

Chapter 4

Experiment and Observations

This chapter presents observations from an ionospheric heating experiment conducted on 27 November 2014. The aim of this experiment was to study the angular dependence of WAILEs excited during heating. It describes the details of the ionospheric modification experiment and UHF IS-radar observation scheme as well as the ionospheric conditions during the experiment. It also details the methods developed to determine the spatial characteristics of WAILEs.

4.1 Experiment details

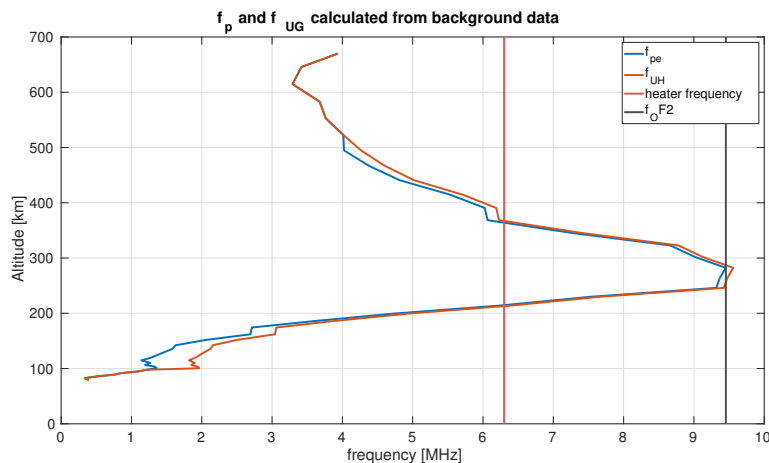


Figure 4.1: Plasma and upper hybrid frequency profiles calculated from background electron density measured by the EISCAT UHF radar. The red line indicates the heater frequency for the duration of the data we will use, and the black line denotes f_oF2 .

From 11:31-13:19 UT, the Tromsø Heating facility array 1 [Rietveld et al., 1993] was operated in a 150s on, 85s off cycle, alternating between X- and O-polarization, transmitting with the beam pointed along the direction of the magnetic field (77.5° elevation). The pump wave was transmitted at a frequency of

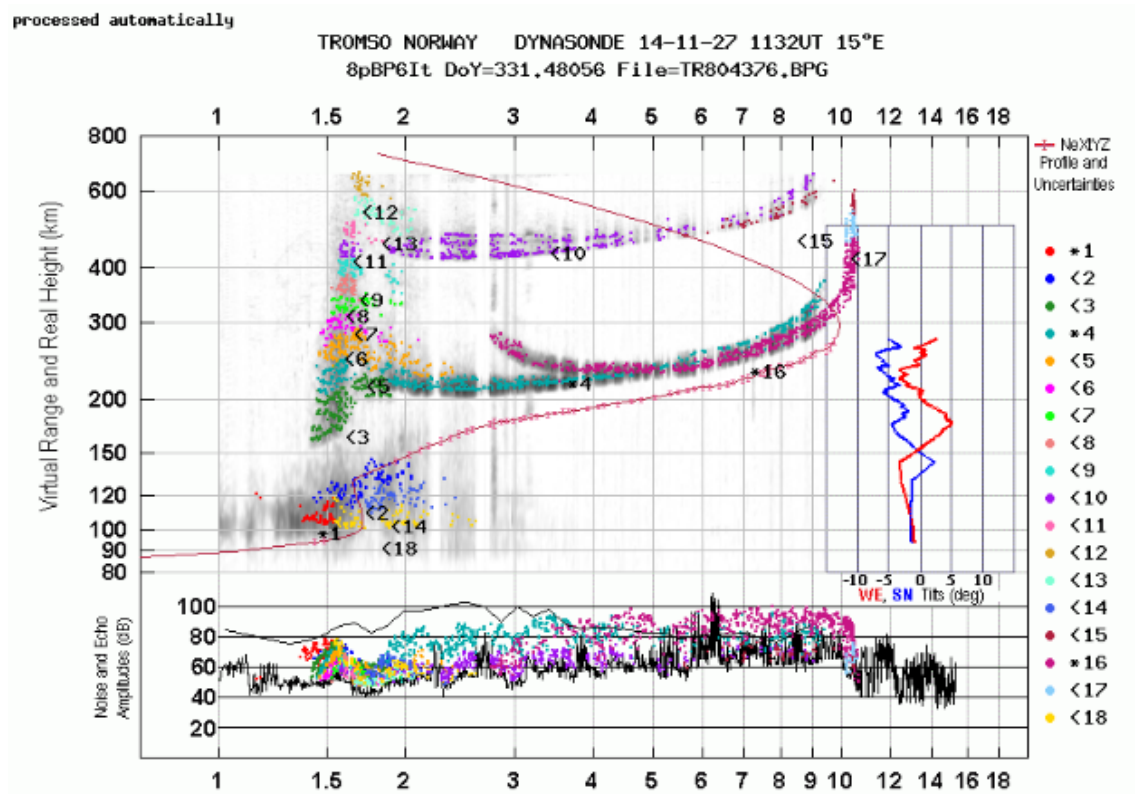


Figure 4.2: Dynasonde measurement from 11:32, shortly after the beginning of the experiment. The strong second hop seen in purple above 400km is an indication of low D-region absorption, meaning favorable conditions for F-region heating experiments. Retrieved from <https://dynserv.eiscat.uit.no/> 6 May 2019.

6.3MHz and 960kW total power. The time of a heating cycle was therefore 470s: one 150s O-mode pulse, 85s off, one 150s X-mode pulse, 85s off.

The EISCAT UHF radar was operated in a 14-step, 8-position scan cycle, scanning in elevation around approximately 2 degrees of magnetic zenith (77.5), with a 5-second dwell time in each position. The radar ran the Beata experiment [Tjulin, 2015], which provides range coverage between 49 and 693km and a time resolution of 5 seconds. The geomagnetic conditions were quiet and stable. f_oF2 during the beginning of the experiment was 10.04 MHz, and the heater reflection height at 6.3MHz was around 200 km. The same heating cycle continued from 13:20 - 14:45 at 5.423 MHz as f_oF2 had decreased to 8.5 MHz.

One heater cycle corresponds to 94 5s scan steps, i.e. 6 full scan cycles plus 10 additional steps in the radar elevation scan. As can be seen in figure 4.3, this means that the radar scan pattern during each heating cycle was out of phase with the previous cycle. The stable ionospheric conditions meant that the response from the first 10 heating cycles were all very similar (see figure 4.4), which allows the use of superimposed epoch analysis to re-organize the GUIDAP-analyzed data of these cycles into a composite data set over a full heating cycle for each altitude, elevation (scan angle) and time after heater on.

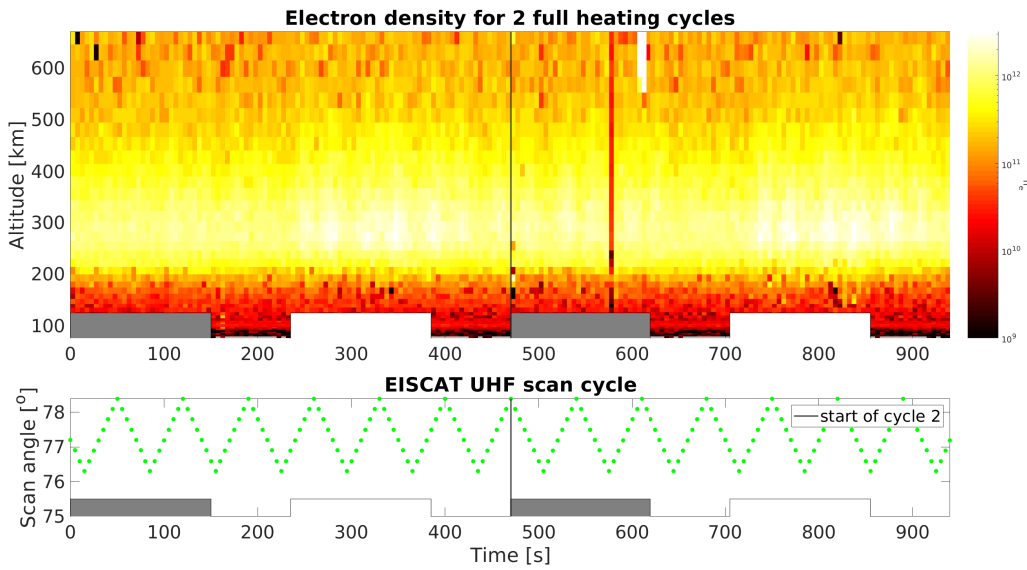


Figure 4.3: Electron density data of the first two full heating cycles. The radar is in the mid-point of the elevation scan at the beginning of the first cycle, and at the highest elevation of the scan at the beginning of the second cycle. The grey boxes mark the O-mode pulses and the white boxes denote the X-mode pulses.

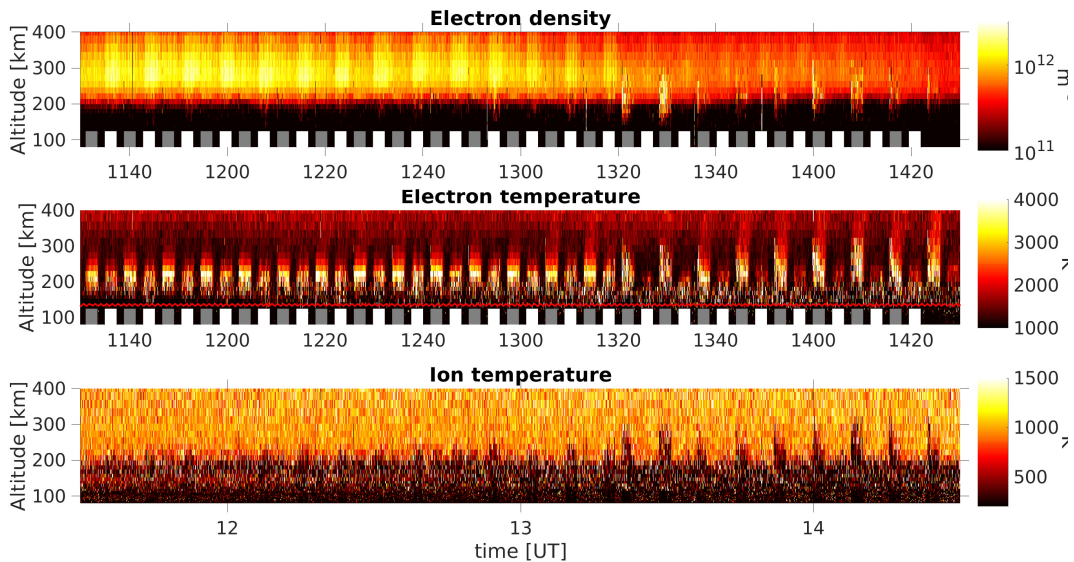


Figure 4.4: Top panel shows measured electron density, middle panel shows electron temperature and bottom panel shows ion temperature. The grey boxes indicate O-mode pulses, while the white boxes indicate X-mode pulses. The scan cycle is plotted in red in the middle panel along with electron temperature. The difference between the response of X- and O-mode heating can clearly be seen in the electron temperature data. No significant response in ion temperature can be seen for the duration of the experiment used (until 13:20 UT).

4.2 Data analysis

Studying the characteristics of WAILEs and their angular width around magnetic zenith requires a cohesive set of data for the time evolution of a heating cycle at each radar scan angle. The particularly stable ionospheric conditions and nonsynchronous heater/radar scan cycles allow just such a data set to be compiled. The ionospheric parameters at each altitude and time are sorted into a 3-dimensional array according to the time after heater on and the scan angle of the radar. The number of data values measured at the same time and scan angle are kept, allowing the averaging of time-position-altitude sets with multiple measurements. The exact process is shown in `HF20141127_dataread.m` in Appendix B.

The rearranged arrays contain data values in 94-5s time steps, 42 range gates between 50-693 km and 8 radar scan angles between 76.3-78.4 degrees, with arrays for electron density, electron temperature as well as the standard deviation at each point for each of these parameters, and background density and temperature data compiled from the last 20 s of data prior to the beginning of the main experiment. These arrays are split to separate the data during the X- and O-mode pulses. Examples of the resulting data sets can be seen in figures 4.5 and 4.6 through 4.13. The main focus of the following analysis is the electron density data from both X- and O-mode pulses.

Parameter	Value
$n_e X$	Total electron density during X-mode pulse
$n_e O$	Total electron density during O-mode pulse
$T_e X$	Electron temperature during X-mode pulse
$T_e O$	Electron temperature during O-mode pulse
$n_{e bg}$	Background electron density
$T_{e bg}$	Background electron temperature
$\sigma_{n_e}/\sigma_{T_e}$	Standard deviation of data point as analysed by GUISDAP
h	Altitude
el	Radar scan angle
$f_o F^2$	Maximum ionospheric plasma frequency
B_0	Geomagnetic field

Table 4.1: List of ionospheric parameters and other values used during analysis

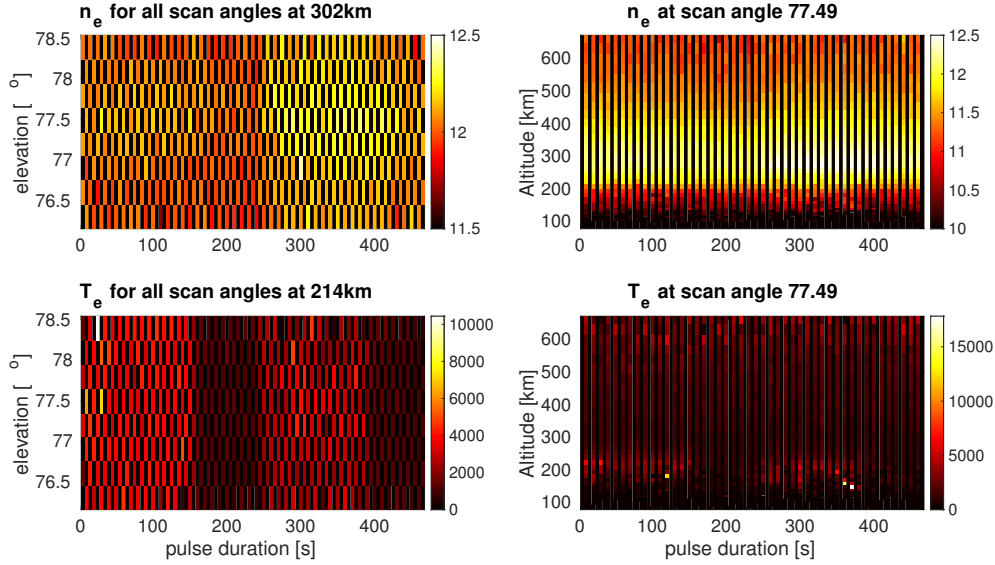


Figure 4.5: Left panels: Electron density at 214 km and electron temperature at 302 km for all scan angles, after superimposed epoch analysis. Right panels: Electron density and temperature altitude profiles for UHF radar elevation 77.5° , magnetic zenith. All panels show the full scan cycle of one X- and one O-mode pulse. As is obvious here, data are missing for some scan angles and times. This makes the plots rather difficult to look at. Subsequent plots of measured ionospheric parameters use a function to fill NaN-values [D’Arrico, 2012b].

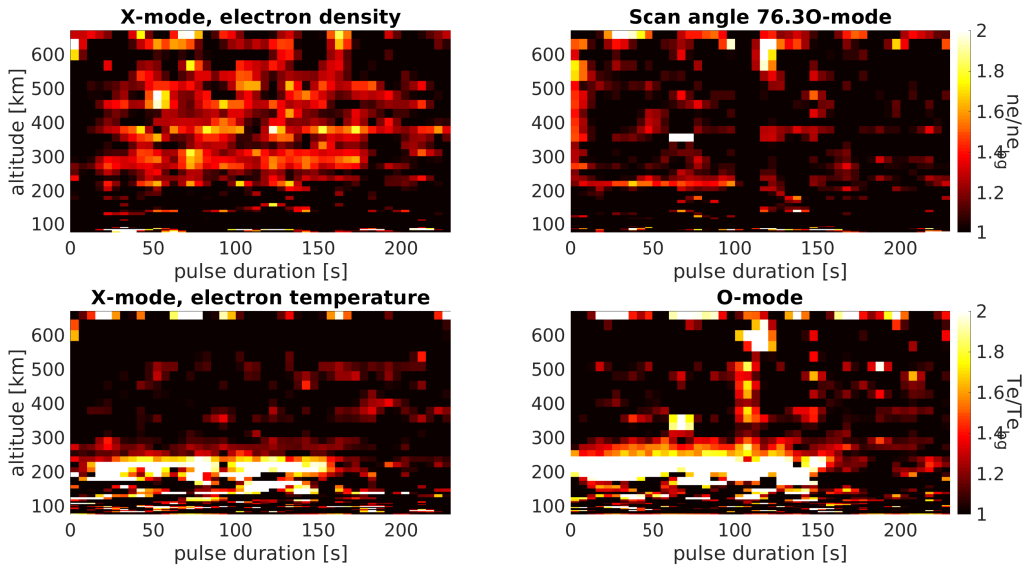


Figure 4.6: Density as ratio of background value and temperature data for X-mode (left) and O-mode (right), scan angle 76.3. NaN values filled using `inpaint_nans`

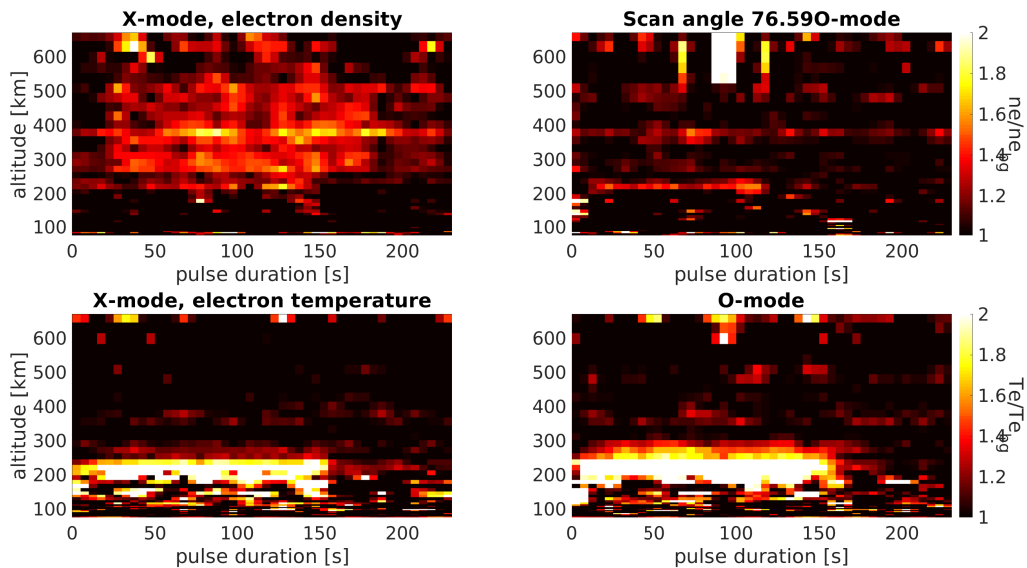


Figure 4.7: Density as ratio of background value and temperature data for X-mode (left) and O-mode (right), scan angle 76.6. NaN values filled using `inpaint_nans`

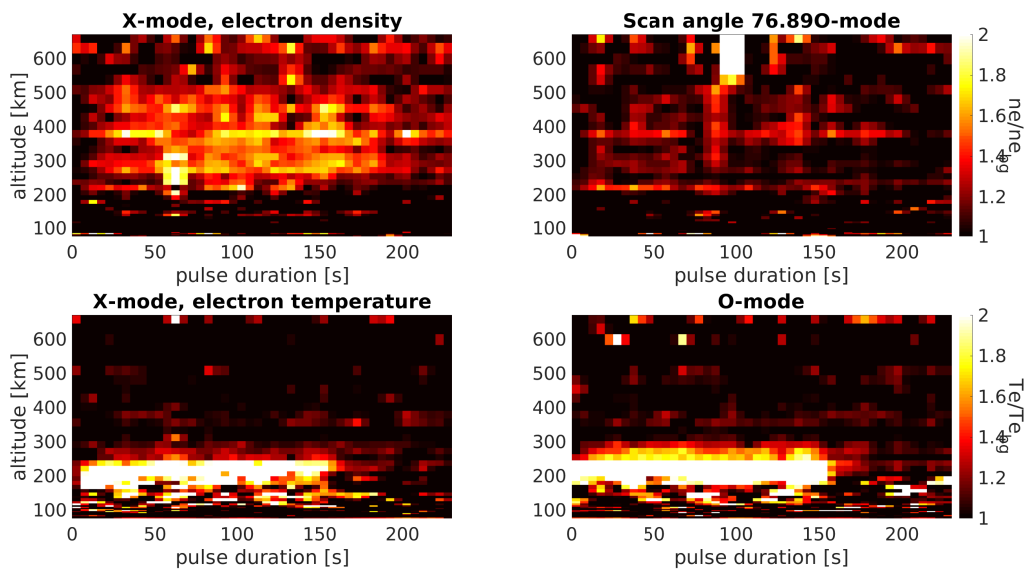


Figure 4.8: Density as ratio of background value and temperature data for X-mode (left) and O-mode (right), scan angle 76.9. NaN values filled using `inpaint_nans`

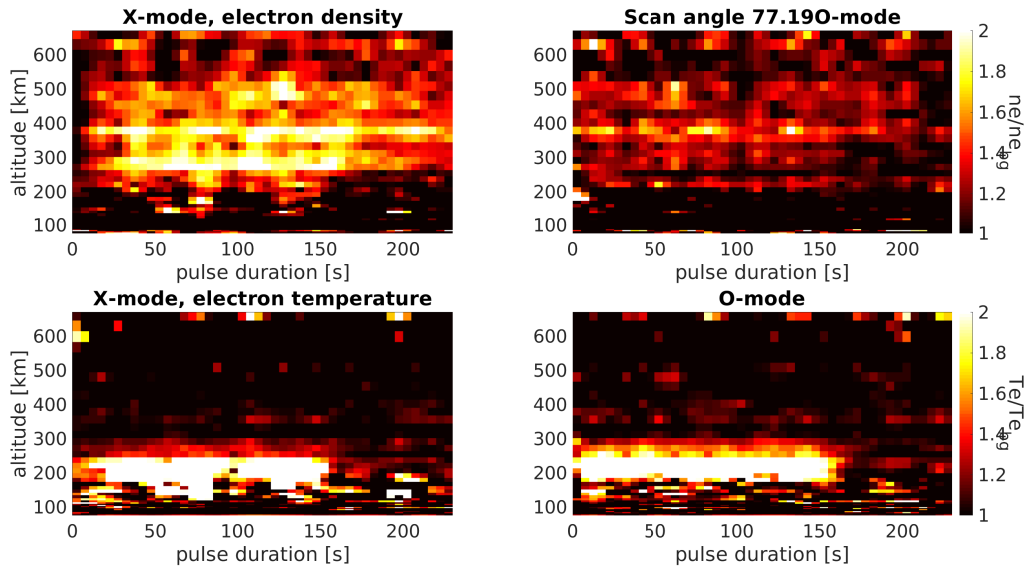


Figure 4.9: Density as ratio of background value and temperature data for X-mode (left) and O-mode (right), scan angle 77.2. NaN values filled using `inpaint_nans`

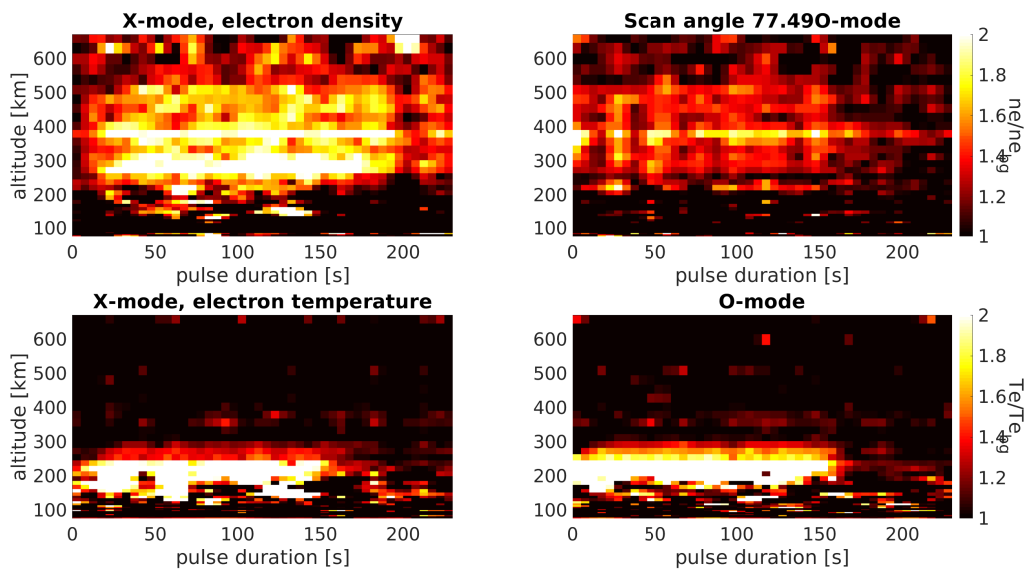


Figure 4.10: Density as ratio of background value and temperature data for X-mode (left) and O-mode (right), scan angle 77.5. NaN values filled using `inpaint_nans`

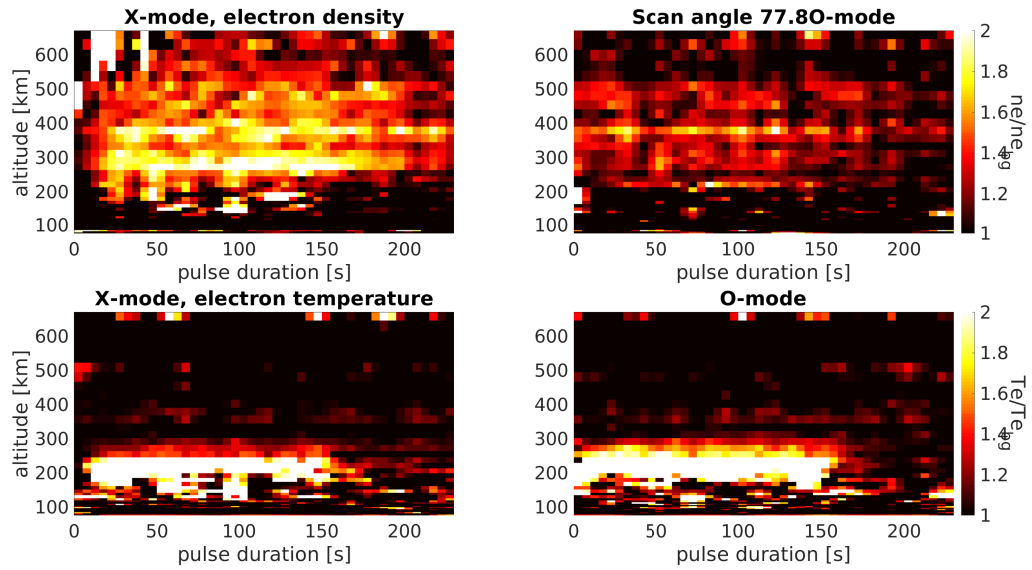


Figure 4.11: Density as ratio of background value and temperature data for X-mode (left) and O-mode (right), scan angle 77.8. NaN values filled using `inpaint_nans`

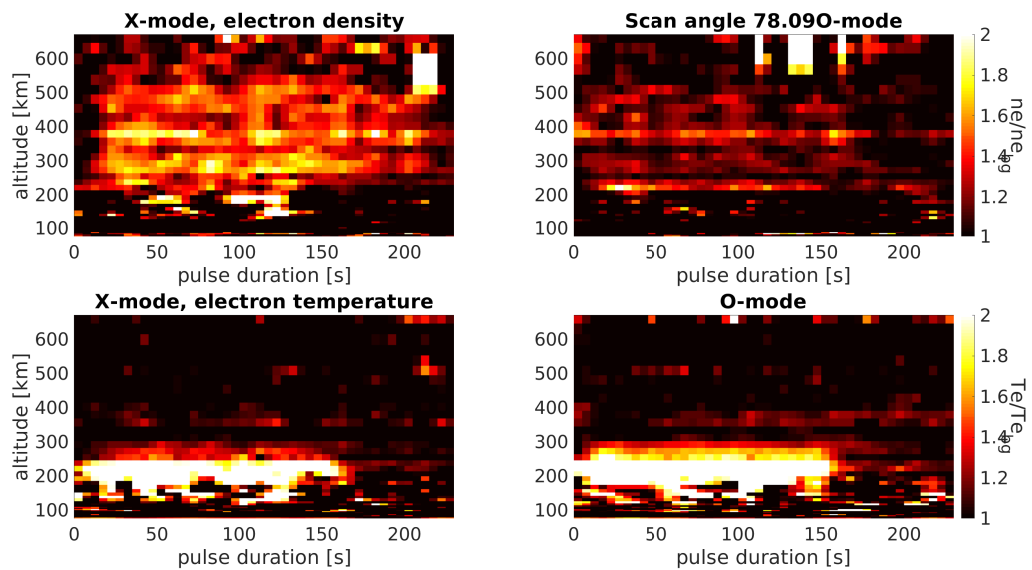


Figure 4.12: Density as ratio of background value and temperature data for X-mode (left) and O-mode (right), scan angle 78.1. NaN values filled using `inpaint_nans`

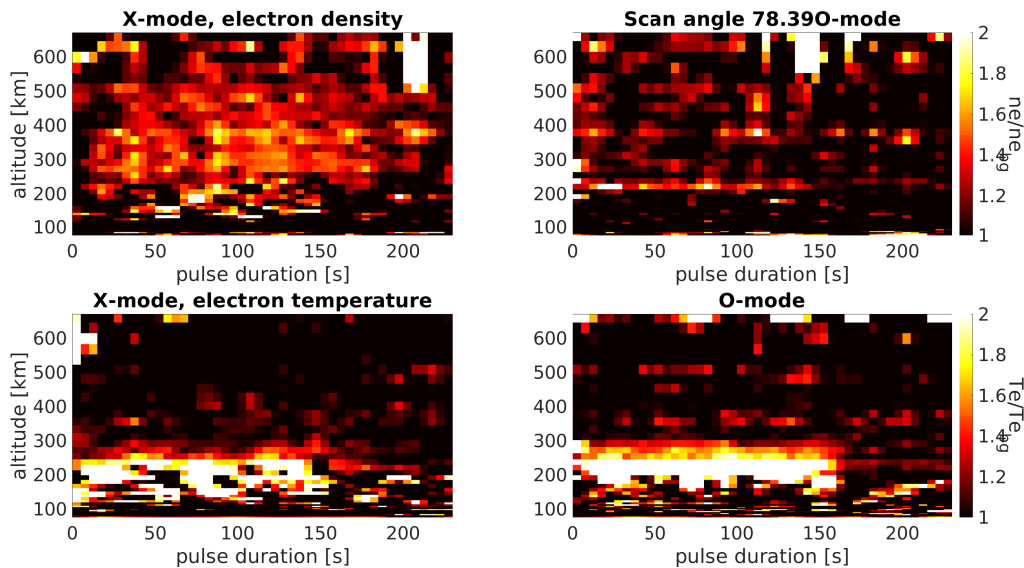


Figure 4.13: Density as ratio of background value and temperature data for X-mode (left) and O-mode (right), scan angle 78.4. NaN values filled using `inpaint_nans`

4.3 Observed WAILES

Figures 4.6-4.13 clearly show the WAILE excitation up to about 500 km and centrally at 77.2-77.8 degrees for both X- and O-mode pulses, but with some WAILES occurring at all scan angles for the X-mode data. The maximum amplitude of the WAILES is between 1.5-2 times background density for the X-mode pulse, and between 1.2-1.7 times the background density. The electron temperature is fairly uniform for all scan angles, with the heated region reaching about 250 km for the X-mode pulse and just below 300 km for the O-mode pulse. The maximum temperatures observed during heating were 20300K for X-mode and 28500K for O-mode. The SuperDARN Hankasalmi radar was operating in a mode that was not favorable for detecting AFAI during the experiment, so the length scale and growth/decay times of AFAI excited during the experiment are not known.

Chapter 5

Results and analysis

This chapter presents the data analysis methods used to study the characteristics of the WAILEs observed during the experiment. The main objective was to estimate the angular width of the WAILES observed during the experiment. The results and uncertainties of the model used are presented. The hypothesis that WAILEs are caused by the refraction of the UHF-radar beam on AFAIs is used to estimate depletion depths corresponding to the measured elevation width of the WAILEs using ray tracing.

5.1 Estimating WAILE characteristics

In order to determine the characteristics of WAILEs, estimates of the WAILE amplitude as well as its growth and decay times are needed. A parametric model was created of the time development of a heating pulse with simple characteristics that can be fit to observed data at each altitude and elevation. Assuming that the growth and decay characteristics are approximately exponential, the model function, illustrated in figure 5.1 takes the form:

$$f(t) = n_e + \delta n_e \left(1 - e^{\left|\frac{t}{\tau_g}\right|} \cdot e^{-\frac{t - \Delta t_{off}}{\tau_d}}\right) \quad (5.1)$$

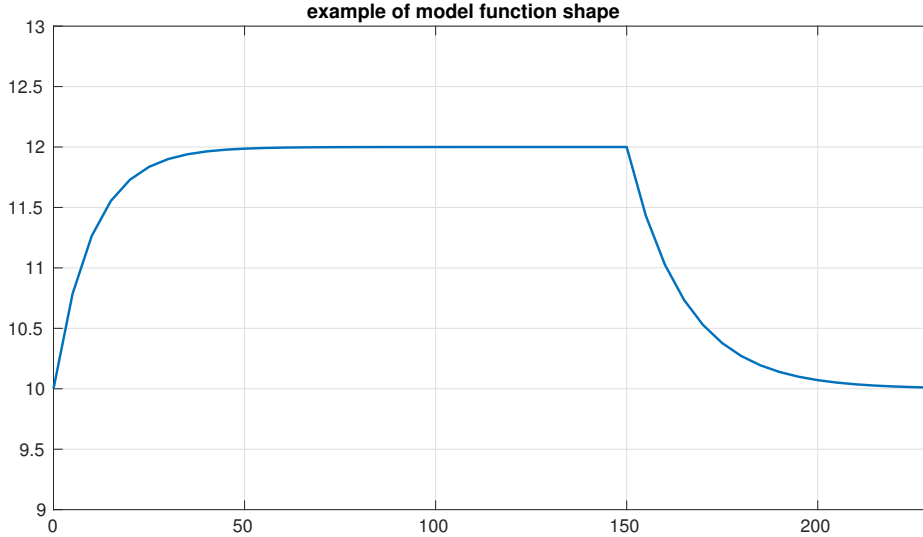


Figure 5.1: Example of output of model function 5.1, here for parameters $n_e = 10$, $\delta n_e = 2$, $\tau_g = 10$, $\tau_d = 15$, $t_{off} = 150$

Parameter	Represented value
n_e	background electron density
δn_e	WAILE amplitude
τ_g	growth parameter
τ_d	decay parameter
Δt_{off}	time to end of heater pulse

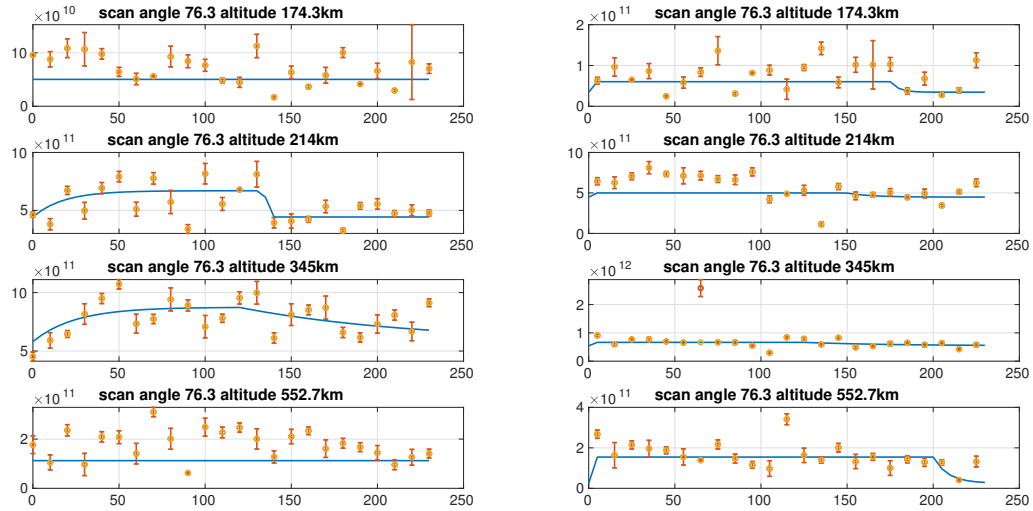
Table 5.1: Explanation of model function parameters

Finding the model parameter values that best fit the data requires finding the minimum square error of the model function and the data for each altitude-elevation set. This is done by running an optimization algorithm to find parameters that minimizes:

$$err = \sum_{t_i} \frac{(n_{model}(t_i, h, \theta) - n_{data}(t_i, h, \theta))^2}{\sigma_{n_e(t_i, h, \theta)}^2} \quad (5.2)$$

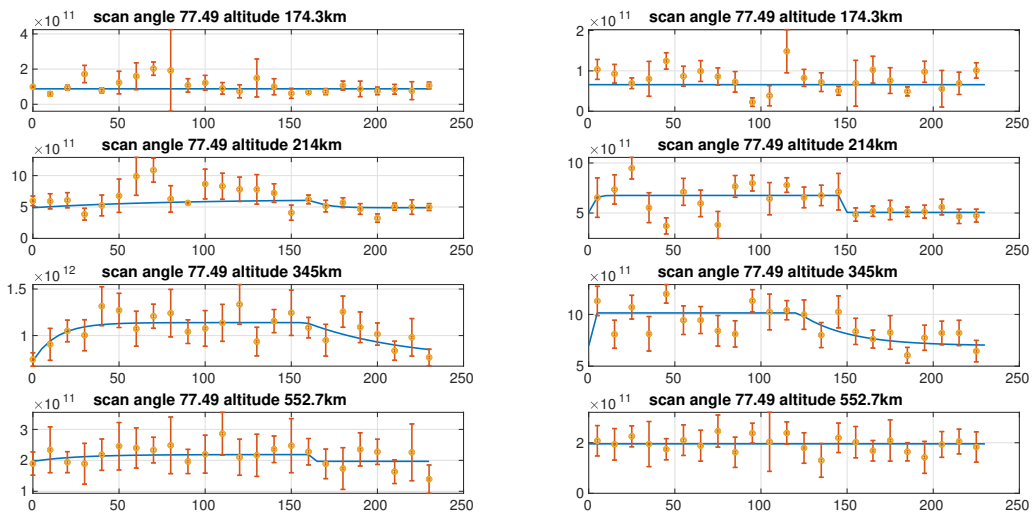
The parameter search was done using the Nedler-Mead simplex algorithm [Lagarias et al., 1998]. The average background values and max value of each data set were used as starting guesses for n_e and δn_e , and upper and lower bounds were set to be within $3 \times$ the starting guesses, which helped prevent the algorithm from diverging. Certain data values in the upper range gates and at the reflection height where HFIL could be seen were removed and replaced with nearest mean values. Examples of this can be seen in figure 5.2. The maximum number of iterations was set to 15000, and the tolerance was set to 1×10^{-4} . The optimization algorithm found a solution within the tolerance for all altitude-elevation pairs. The primary parameter of interest is δn_e , the electron density amplification, as this will show the heights and scan angles at which WAILES occur.

It is important to note when considering this data that the short integration time used in the GUIDAP analysis means that the signal-to-noise ratio is rather low, and further that the error estimates provided by the GUIDAP analysis have particularly high variability. This means that robustly fitting all parameters is a lot to ask of this relatively simple model.



(a) X-mode, scan angle 76.3°

(b) O-mode, scan angle 76.3°



(c) X-mode, scan angle 77.5°

(d) O-mode, scan angle 77.5°

Figure 5.2: Modelled and observed data with GUIDAP analyzed error at heights below and at reflection, as well as centrally where WAILEs occur and at the upper range limit of the radar. The yellow data points are instances where an outlier data value was removed and replaced with a nearest mean value. Similar plots for all scan angles can be found in Appendix A.

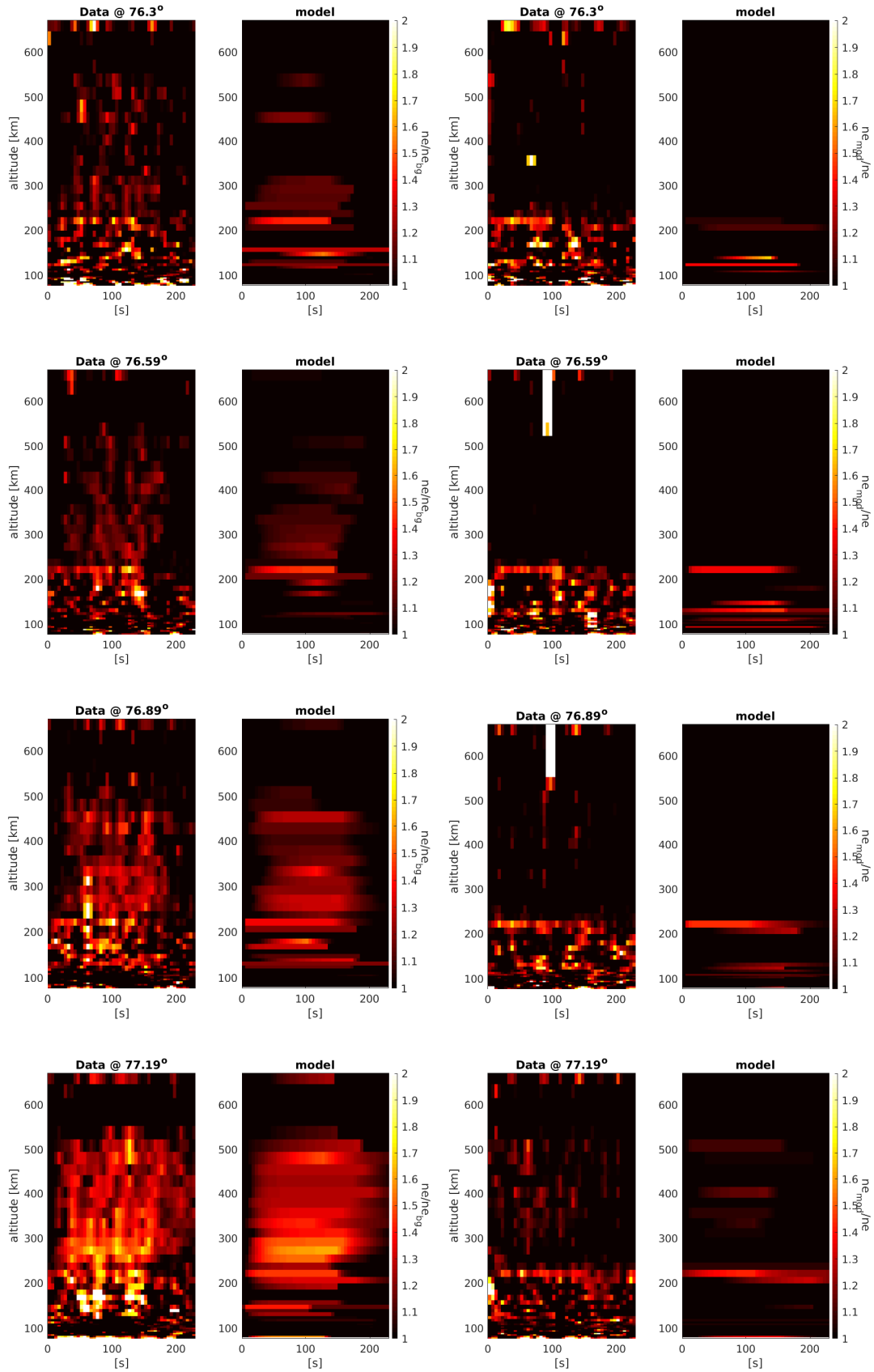


Figure 5.3: Observed and modelled electron density as ratio to background for first four scan angles. X-mode observed and modelled data on the left, O-mode on the right. The height extent of the WAILE amplitude in the modelled and observed data match fairly well.

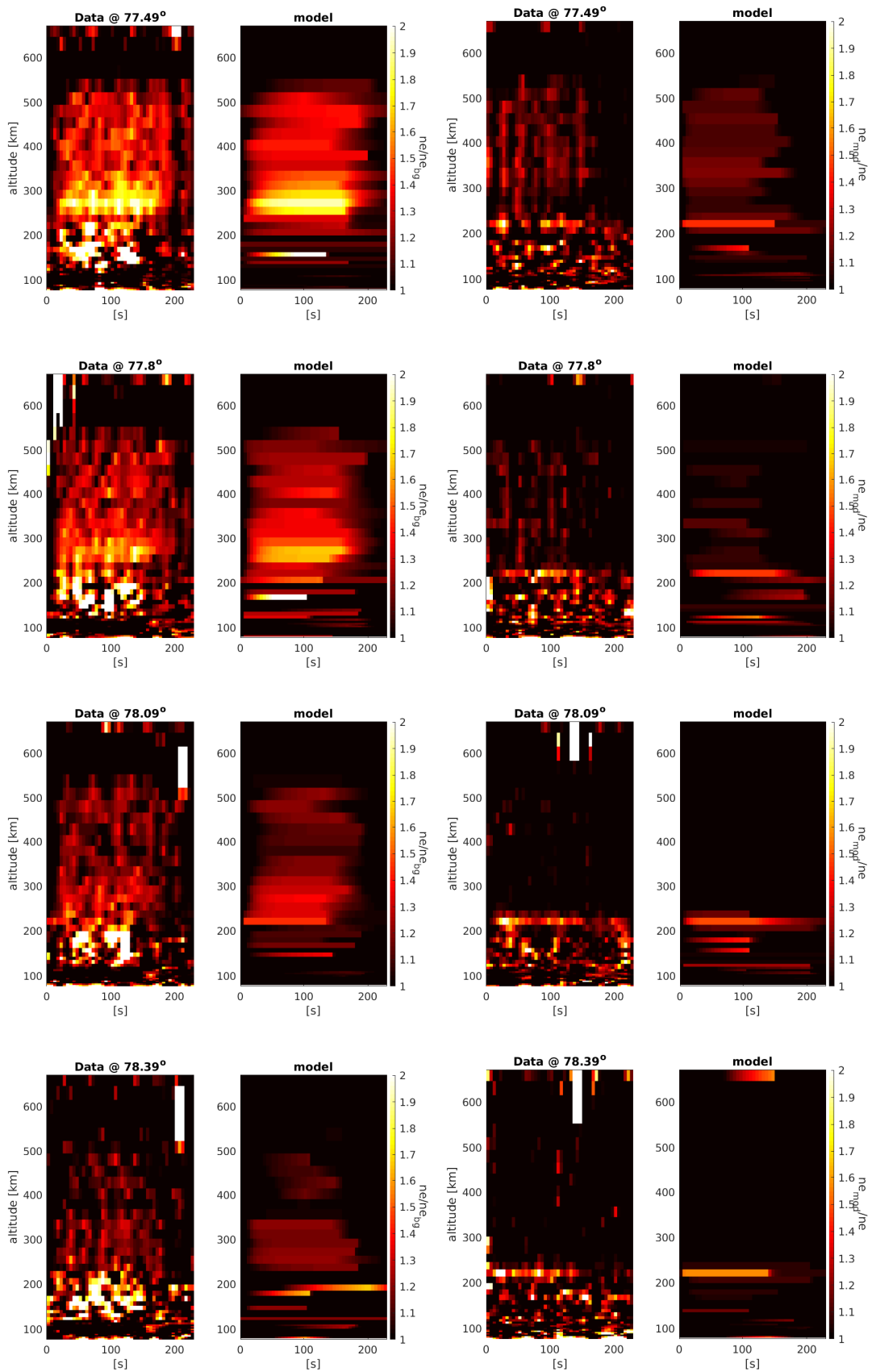


Figure 5.4: Observed and modelled electron density as ratio to background for remaining scan angles.

Figures 5.3 and 5.4 show that the modelled and observed electron density data overall match reasonably well above the reflection height and at the central radar scan angles where WAILEs are most visible. Overall, the relatively small amount of data with low SNR ratio and low time resolution means that it is not possible to create an ideally fitted simple model. However, the important point for this analysis is that the length of the pulses allows the WAILE amplitude parameters to be fairly well estimated independent of time. This provides important information on the altitudes and scan angles at which the apparent density enhancements occur.

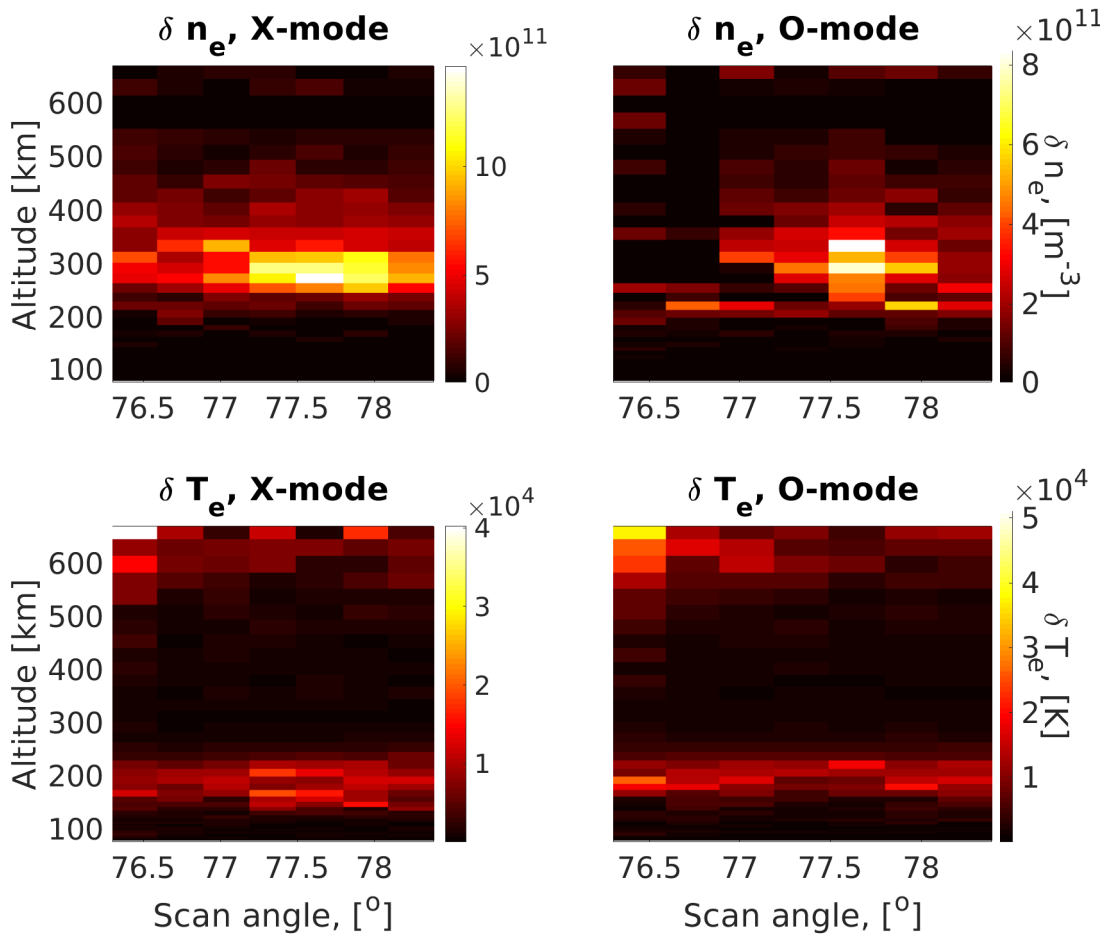


Figure 5.5: Model δn_e and δT_e parameters, plotted for each altitude and scan angle. The figure shows that the apparent density enhancement parameters are scan angle dependent, while the temperature enhancement parameters remain uniform for all scan angles, and significant enhancement only occur near reflection height.

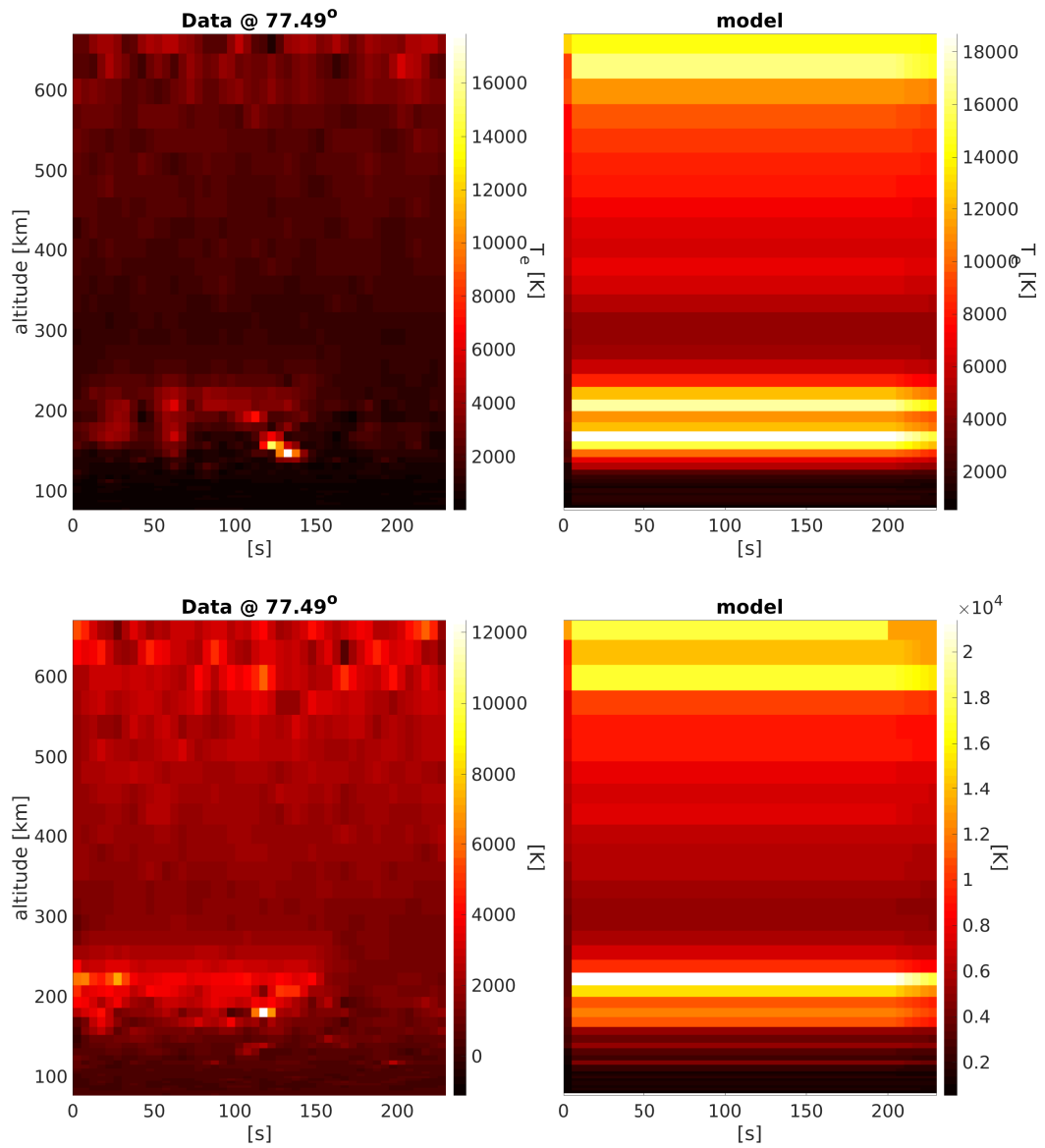


Figure 5.6: Top: X-mode temperature and model. Bottom: O-mode temperature and model. Example of temperature observations and model. Due to the poor fit of the model, electron temperature characteristics during heating will not be discussed further in this thesis.

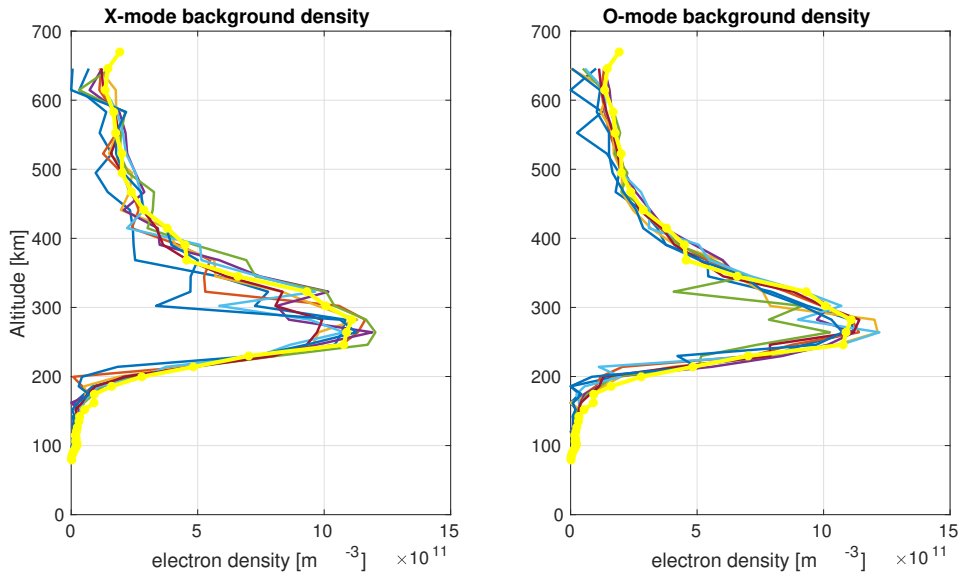


Figure 5.7: Modelled background densities for each scan angle, with average background density calculated from the last 20s before the beginning of the experiment.

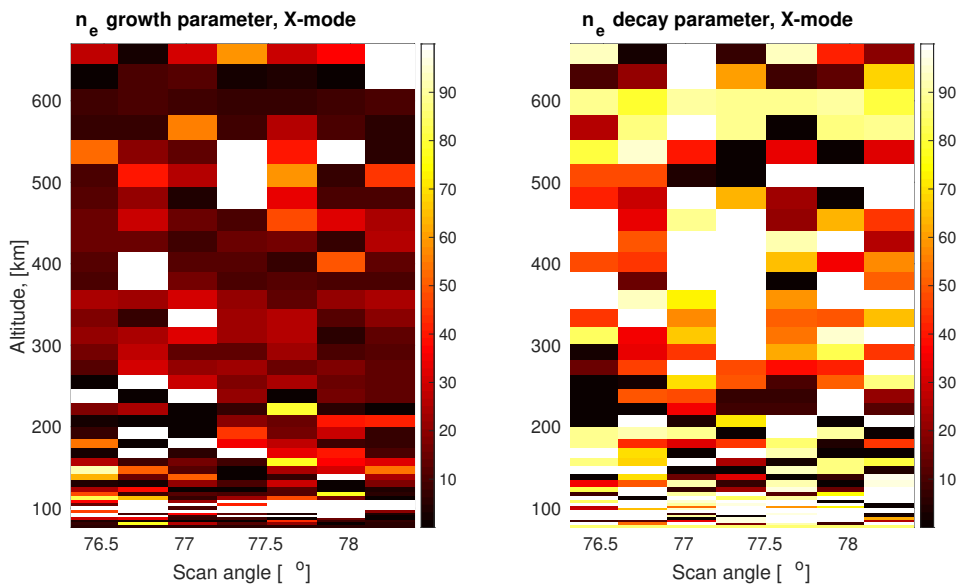


Figure 5.8: Electron density growth and decay parameters. The growth and decay parameters unfortunately show no clear systematic pattern for any of the data sets, so will not be further considered in this thesis.

The model function used was not particularly successful in fitting the electron temperature observations, as seen in figure 5.6. For this reason, electron temperature data will not be considered further in this thesis. The time resolution of the data is not good enough for any clear patterns to be seen in the growth and decay parameters. Although these parameters are not central to this thesis work, having a good estimate of the growth and decay times may have allowed for the

horizontal length scale of the hypothesized AFAIs to be determined based on [Frolov et al., 1997] (or similar work).

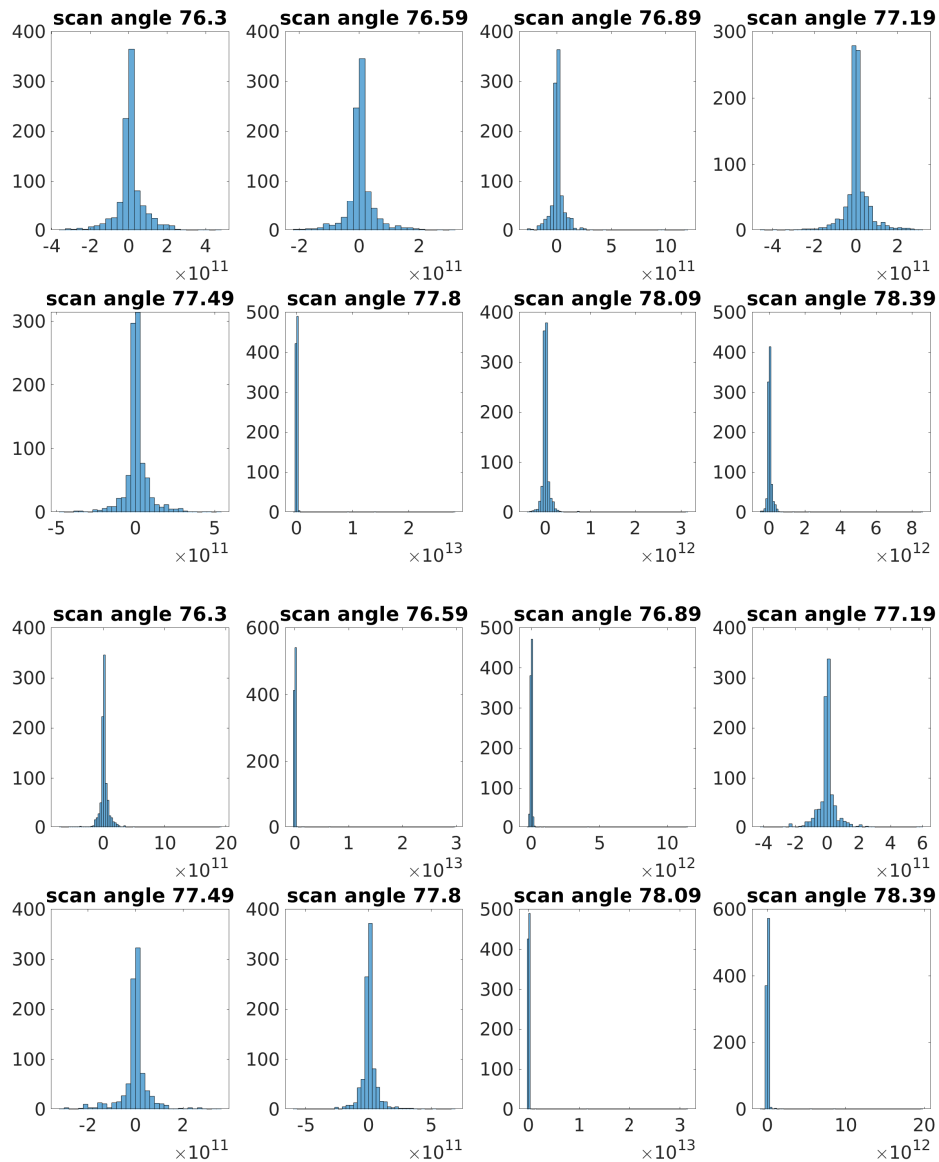


Figure 5.9: Top: X-mode residuals. Bottom: O-mode residuals Histogram of residual between observed and modelled data over all altitudes and for each elevation. The clear non-Gaussian shape of the histograms indicates that the model is over-fit, meaning that trends will not be accurately predicted. This over-fitting is likely due to the low SNR of the data adding too much variability for parameters to be accurately predicted.

5.2 Deconvolution

WAILEs only occur within a narrow region around magnetic zenith [Senior et al., 2013]. What is not known is just how narrow this region is. The angular scan steps are smaller than the 0.6° half-power beam width of the UHF radar, so it is important to consider the effect of the power of the UHF radar beam on the received signal. The ISR measured apparent electron density is the average of the electron density weighted by the antenna beam pattern:

$$ne_{ISR}(\theta_r) = \frac{\int_{-\infty}^{\infty} ne(r(\beta)) \cdot B_{ISR}(\beta - \theta_r) d\theta}{\int B_{ISR}(\beta - \theta_r) d\beta} \quad (5.3)$$

where B_{ISR} is the antenna pattern of the radar and θ_r is the angle of centre of the radar beam. In this form the observed density data is the convolution of the apparent ionospheric density variation/WAILE with elevation and the beam pattern of the radar. This can be undone to some extent using deconvolution techniques. As convolution is equivalent to multiplication in the Fourier domain, time domain deconvolution is formally equivalent to Fourier domain division. To remove the effect of the antenna pattern from the modelled data, both signals were Fourier transformed, then the apparent density data was divided by the antenna pattern. and the resulting signal was reverse Fourier transformed back to the time domain. This is the deconvolved WAILE amplitude for each altitude-elevation point, and gives an accurate depiction of the angular width of the WAILEs observed during the experiment. The radar beam pattern was approximated based on a Bessel function of the first order [Mahafza, 2000], giving an aperture factor:

$$E(\beta) = \pi r^2 \frac{2J_1(kr \sin \beta)}{kr \sin \beta} \quad (5.4)$$

Where β is the angle from boresight, r is the radius of J_1 is the first order Bessel function and $k = \frac{2\pi}{\lambda}$ (λ being the radar wavelength).

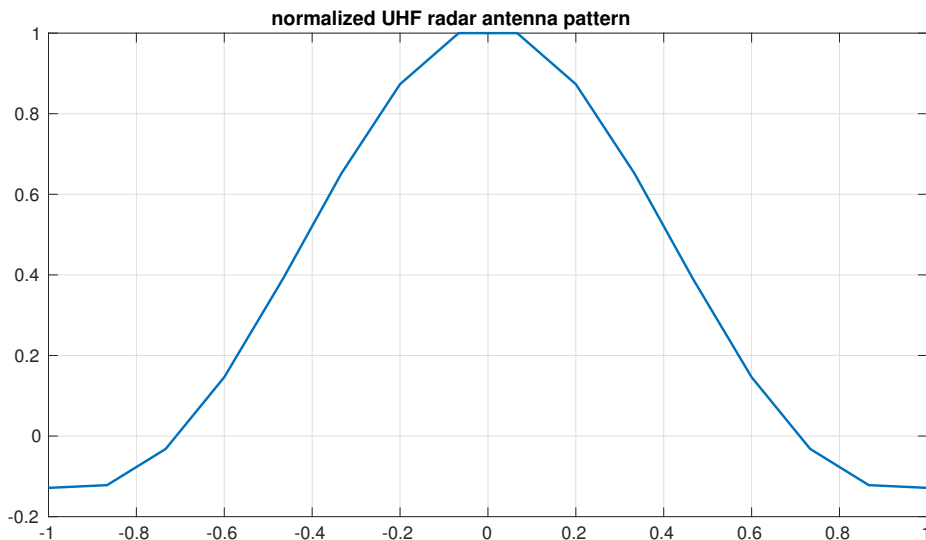


Figure 5.10: Normalized modelled beam pattern within 2 degrees of boresight.

This was implemented using the function `radar.beampattern.m` (see Appendix B), which is an adapted version of the `circ_aperture.m` function described in [Mahafza, 2000]. The modelled data was interpolated in terms of elevation from 8 to 16 data points to achieve a cleaner deconvolved result. The deconvolution was done with normalized modelled data and beam power functions, using `deconvolution.m` by [Kalkan, 2017]. The full process of deconvolution is found in `HF20141127_deconv.m` in Appendix B.

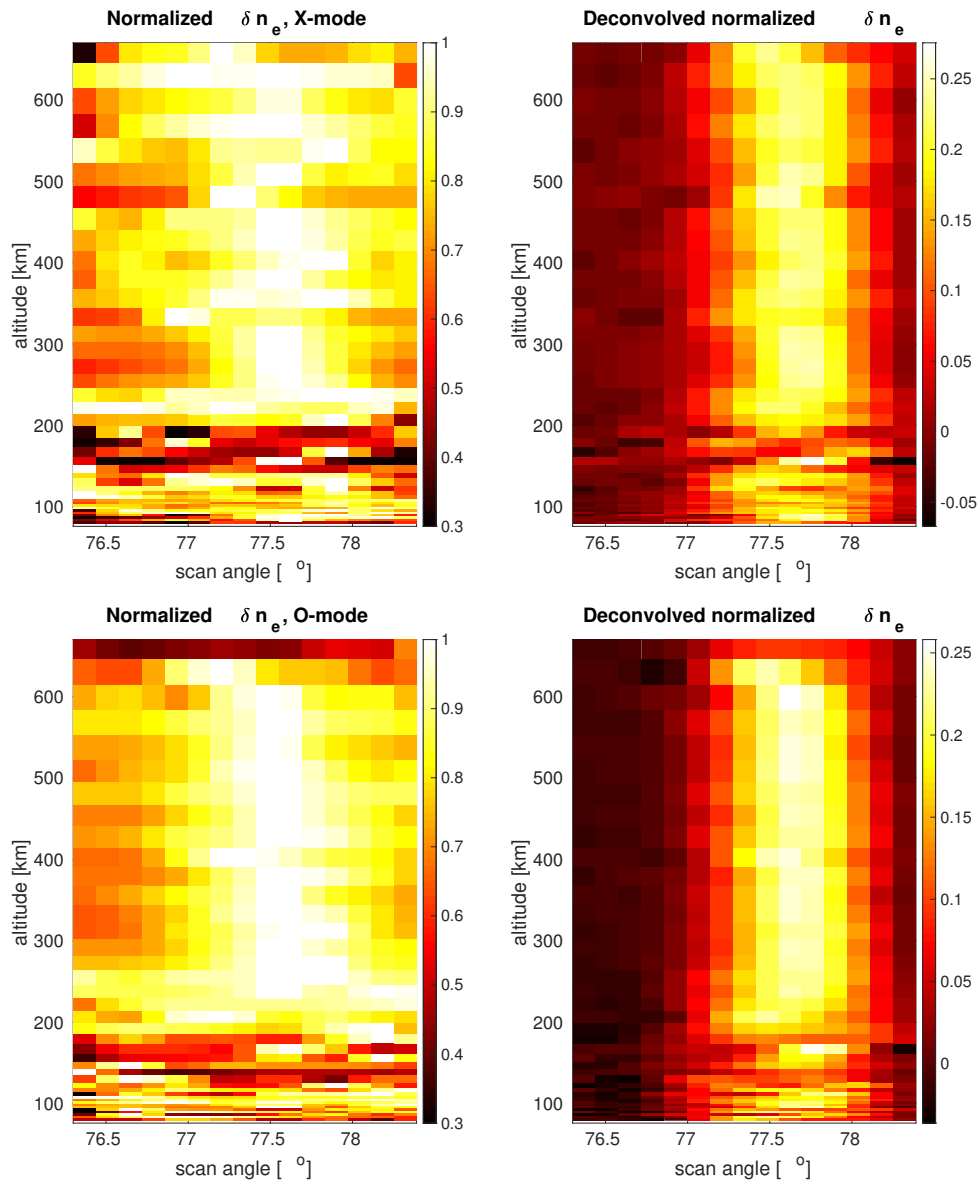


Figure 5.11: WAILE amplitudes in terms of elevation, before and after deconvolution, for X-mode (top) and O-mode (bottom).

5.3 Analysis of deconvolved data

The angular width of the the WAILEs was found to be within 0.5 degrees of magnetic zenith based on the standard deviation of the deconvolved data, as shown in table 5.2 and figure 5.12. Taking the difference of the deconvolved X- and O-mode data, both the angular width of the WAILEs and their altitude extent (see figure 5.13) are very similar for both polarization modes.

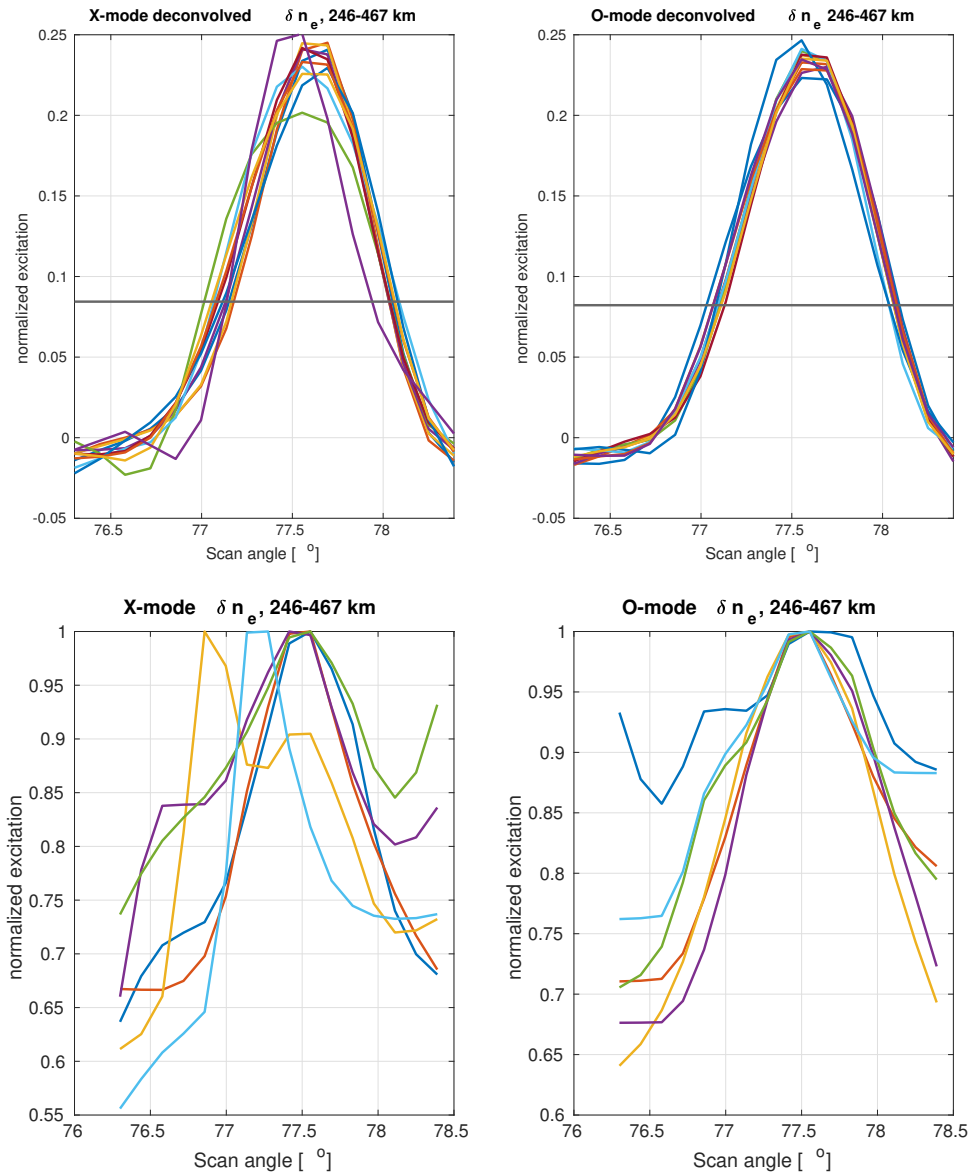


Figure 5.12: Top: Deconvolved data of WAILE amplitude in terms of scan elevation for range gates near the heater reflection height to near the upper range of the radar. The black horizontal line indicates the mean standard deviation of the amplitude, showing the approximate range of angles where the excitation occurs. Bottom: WAILE amplitude parameters at same height range as top image, before deconvolution.

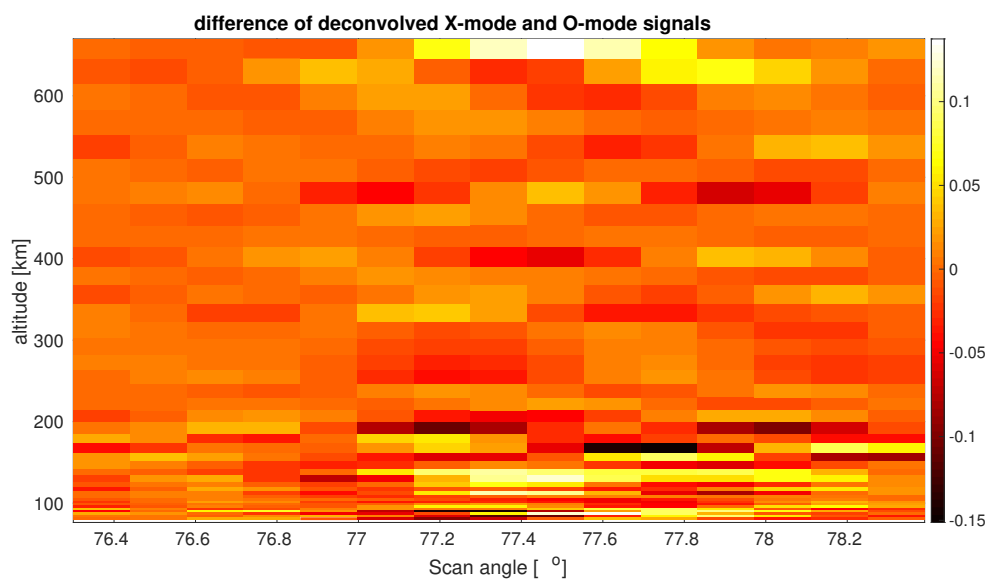


Figure 5.13: Difference of X- and O-mode deconvolved data. This shows that the angular width of the excitation is very similar for both X- and O-mode heating.

Altitude [km]	X-mode σ	X-mode angle [°]	O-mode σ	O-mode angle [°]
76.299	NaN	1.254	NaN	1.254
79.212	0.055123	0.97533	0.0647	1.254
82.662	0.085413	0.418	0.088808	1.1147
86.006	0.093046	0.836	0.062507	0.55733
88.923	0.09763	0.97533	0.089252	1.1147
91.841	0.079706	1.1147	0.061285	1.3933
94.76	0.084003	1.254	0.087431	0.836
97.679	0.074572	1.1147	0.081489	0.97533
100.6	0.073094	1.1147	0.088969	1.1147
103.52	0.069353	1.254	0.081268	1.254
106.44	0.078755	1.1147	0.076029	1.254
110.14	0.076314	1.254	0.081724	0.55733
114.77	0.071646	1.254	0.076615	1.1147
120.18	0.075429	0.836	0.069311	0.69667
126.56	0.09143	1.254	0.055228	1.254
135.4	0.087812	1.254	0.0435	1.1147
142.25	0.060548	0.97533	0.06777	1.254
152.02	0.10228	0.27867	0.068757	0.836
161.97	0.063015	0.55733	0.090273	0.27867
174.26	0.062535	1.3933	0.059516	1.3933
185.76	0.05783	0.69667	0.077032	1.254
199.58	0.082739	1.1147	0.090182	1.254
213.97	0.090194	1.1147	0.087008	1.254
229.79	0.092061	1.254	0.091289	1.1147
245.97	0.093301	0.97533	0.092955	1.254
263.99	0.094326	0.97533	0.093946	1.1147
282.25	0.094744	0.97533	0.093852	0.97533
302.22	0.093633	0.97533	0.093269	1.1147
322.74	0.087499	1.1147	0.095373	0.97533
344.98	0.094038	1.1147	0.094256	0.97533
368.46	0.094172	0.97533	0.094239	1.1147
390.68	0.090222	1.1147	0.096581	0.97533
414.73	0.093323	1.1147	0.093475	1.1147
440.93	0.092614	1.1147	0.093637	0.97533
467.05	0.094454	0.97533	0.093849	0.97533
494.81	0.093279	0.97533	0.095989	0.97533
522.63	0.089023	1.1147	0.094945	0.97533
552.66	0.095645	0.97533	0.093494	0.97533
582.97	0.090222	0.97533	0.095665	0.97533
614.69	0.094856	1.254	0.089939	1.1147
645.8	0.086674	1.1147	0.042698	1.254
669.8	NaN	1.254	NaN	1.254

Table 5.2: Standard deviation of deconvolved data and corresponding angular width around zenith for each range gate. The angular widths were calculated by finding the closest values in the data to the standard deviation at each altitude and then taking the difference of the corresponding elevations. Because of the limited elevation resolution of the data, this does not provide 100% accurate values, but does provide a close indication.

With the observed angular width in mind, the next step is to find the characteristics of density depletions that, according to the hypothesis, are ducting the UHF radar beam and creating WAILEs with a width of 0.5 degrees around magnetic zenith. The edge of the angular width of the excitation will correspond to $90^\circ - \theta_{crit}$, the critical angle for which a ray is refracted parallel to the interface of refractive indexes (as shown in figure 5.14, when Snell's law becomes

$$\frac{n_2}{n_1} = \sin \theta_{crit} \quad (5.5)$$

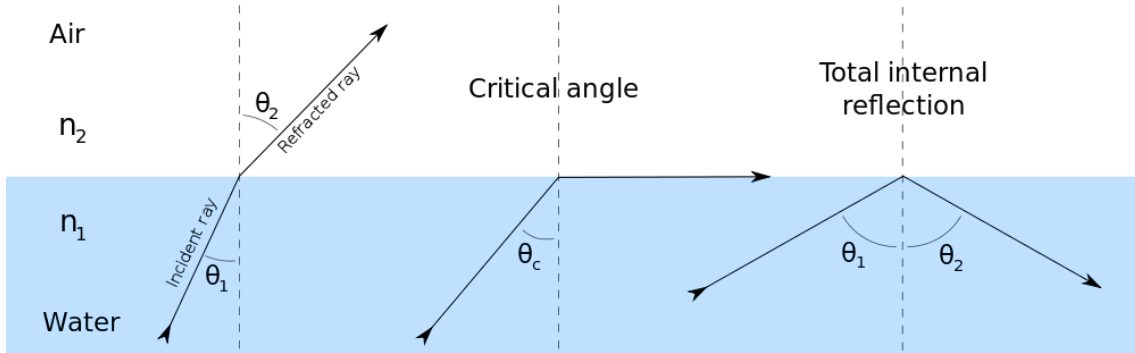


Figure 5.14: Refraction according to Snell's law, from <https://commons.wikimedia.org/wiki/File:RefractionReflexion.svg>, by Wikimedia Commons author Josell7, used under CC 3.0 license

Combining this with equation 2.9, the simplified Appleton-Hartree equation, the plasma frequency necessary for a striation to cause refraction can be calculated from:

$$f_{p2} = \sqrt{\left(1 - \left(\sin \theta_{crit} \cdot \left(\sqrt{1 - \frac{f_{p1}^2}{f_{UHF}^2 + \frac{f_c}{f_{UHF}}}}\right)\right)\right)^2} \cdot \left(1 + \frac{f_c}{f_{UHF}}\right) \cdot f_{UHF}^2 \quad (5.6)$$

Using $f_c = 1.35$ MHz [Rietveld et al., 1993], $f_{UHF} = 930$ MHz [Tjulin, 2015], $f_{p1} = 10.04$ MHz (f_oF2 during experiment) and $\theta_{crit} = 89.5$, the plasma frequency sufficient to refract the UHF radar beam along the magnetic field at f_oF2 would be about 12.89 MHz. At the X-mode heater reflection height for the experiment, the plasma frequency was 5.58 MHz, and the corresponding frequency required for refraction would be 9.85 MHz. These values are approximately 30-60% of the background plasma frequencies, and thus electron densities. Considering the results of [Kelley et al., 1995], where the largest striations observed were about 12%, as well as the energy transferred during heating found in [Stocker et al., 1992, Bryers et al., 2013], it seems improbable that striations with such large amplitudes occur as a result of heating. This is most likely due to an unknown source of error in the calculations that could not be identified, and these theoretical amplitudes will not be considered further.

5.4 Ray tracing

The next step is to run a ray tracing simulation based on the hypothesis that WAILEs result from AFAIs known to occur during heating [Kelley et al., 1995, Blagoveshchenskaya et al., 2011b] (and others) leading to sufficient refractive index modulations for UHF radio waves to be refracted along the magnetic field. A ray tracing program provided by Dr. Juha Vierinen [Vierinen, 2019] was used. This program generates electron density profiles with the international reference ionosphere (IRI) model using the Pyglow library [Duly, 2016], with striations that have a user definable horizontal length scale and amplitude. A model radio wave is then propagated according to the simplified Appleton-Hartree equation (equation 2.9), with the refractive index gradient around the ray being calculated at user defined vertical intervals. The simulation generates vertical striations, rather than striations at magnetic zenith, 12° . This significantly simplifies the geometry, and would likely not have a significant effect on the results, assuming that the ionospheric profile does not vary significantly horizontally, aside from the field aligned striations. Ray tracing is only physically applicable under conditions for ray optics, meaning in cases where the striations have a much larger horizontal length scale than the radar wavelength. Ray optics may be borderline applicable for the AFAIs observed in [Blagoveshchenskaya et al., 2011b, Blagoveshchenskaya et al., 2011a], as these were observed at a horizontal length scale of 10-15m, and the wavelength of the UHF radar is approximately 0.3m. Interactions with smaller scale striations would need to be calculated by solving Maxwell's equations for the non-uniform ionosphere.

5.4.1 Simulation parameters

Striations at depletions between 5-10% were initially used in the ray tracing simulations, based on the results of [Kelley et al., 1995]. These results were used because the theoretical calculations described in the previous section did not provide reasonable values. Additional simulations were run with larger depletion amplitudes as shown in figures 5.19-5.16. The horizontal scale length of the striations was set to 500m to prevent the simulation step size from interfering with the results. This is quite a bit larger than the AFAI measured in [Blagoveshchenskaya et al., 2011b, Blagoveshchenskaya et al., 2011a]. However, because the edge of the striation is the area of interest, the horizontal scale should not, in theory, impact our results. The horizontal length scale of the simulated ionosphere was 5 km in either direction from the origin of the ray. As array 1 has a beam width of 7 degrees [Rietveld et al., 1993], the heated region at 300 km spans tens of kilometers horizontally, so AFAIs within 5 km of the heating facility are entirely reasonable. f_oF2 was 7.3 MHz in the IRI profile at 12:00 UT on the day of the experiment. This was scaled to match f_oF2 of 10.04 MHz, the value measured by the dynasonde. The original profile and scaled profile for f_oF2 of 5 MHz and 12 MHz were also run.

In this simulation, ducting occurred when the gradient of the refractive index was largest, at the interface of a striation and the background atmosphere within a cer-

tain altitude range of f_oF2 . Naturally, this means that for ducting to occur, the ray needs to be at the edge of a striation at some point within this height range. The fixed model ionosphere used in these simulations works fine for categorizing the amplitude of the striations necessary to cause ducting at a certain fixed angle of incidence. It is however, not sufficient for finding the range of incident angles that can be ducted by a striation of a certain amplitude and how this varies, because the change in incident angle means a change in the horizontal position of the ray around f_oF2 . Creating a model ionosphere with a striation strategically placed at the horizontal position where a ray of a certain angle meets the height of f_oF2 would likely be a solution to this, and is an interesting prospect for further study.

5.4.2 Results

For the measured f_oF2 of 10.04 MHz, 12% depletions were sufficient to duct a 930 MHz radio wave, with 11% causing total internal reflection but not further directing the ray upwards. f_oF2 of the IRI model profile for 12:00 UT over Tromsø was 7.3 MHz. The corresponding depletions that led to UHF ray ducting were 15.7% or higher. Scaling the IRI profile to $f_oF2 = 12$ MHz, 10% depletions caused ducting with 9% leading to total internal refraction similarly to 11% depletions for 10.04 MHz. At $f_oF2 = 5$ MHz, 21% depletions caused ducting.

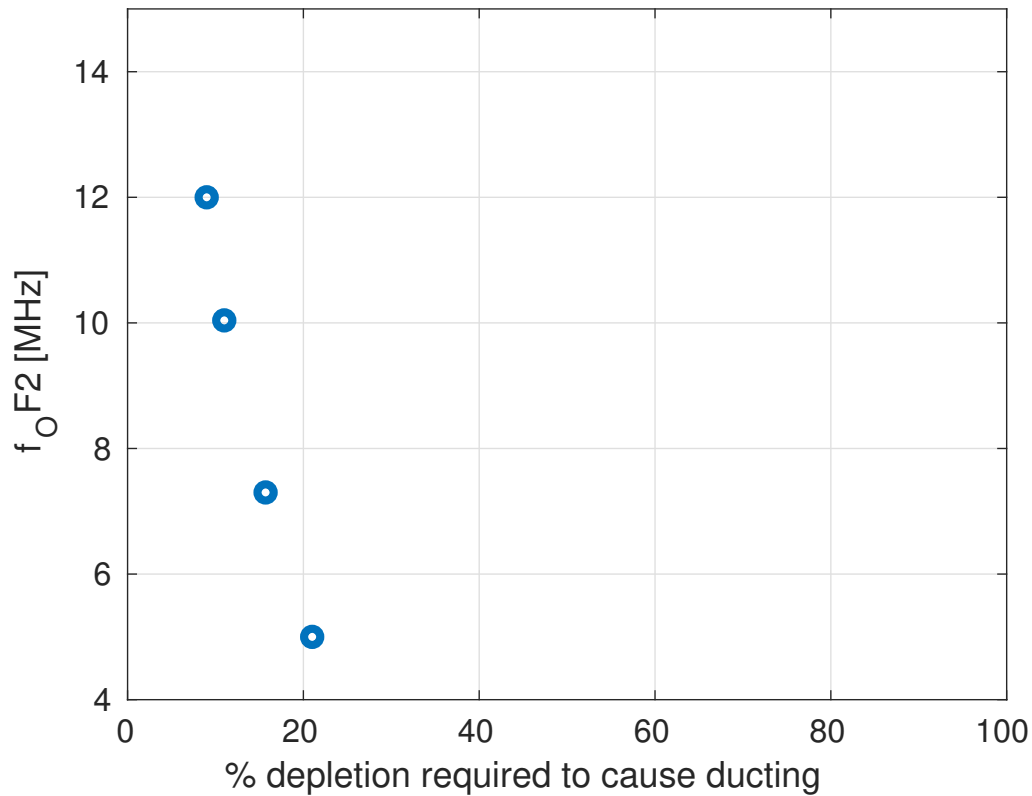
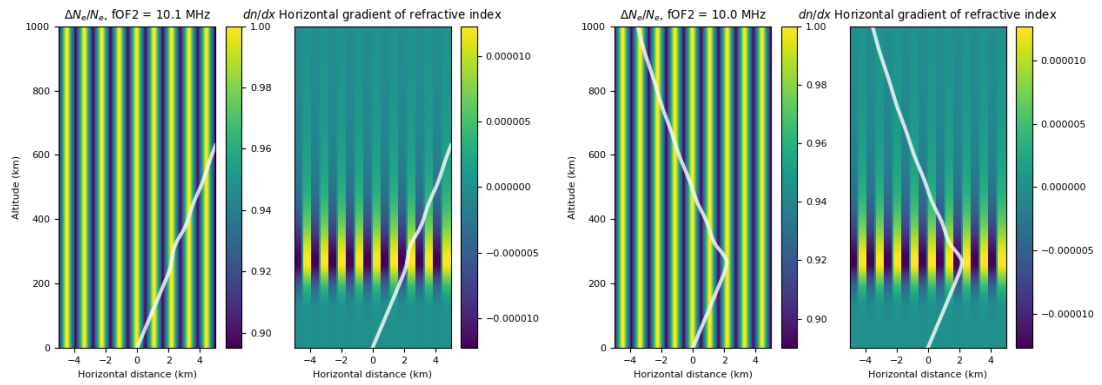
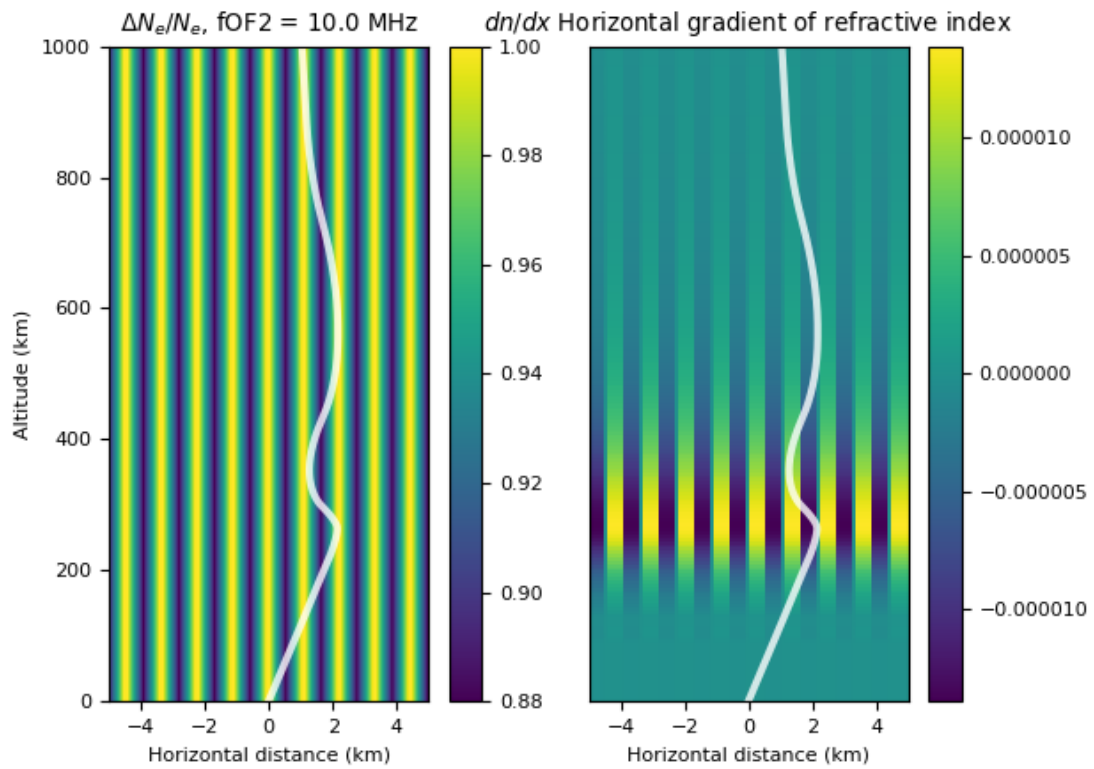


Figure 5.15: Plot of striation percentage sufficient to cause ducting at different f_oF2 values at 0.5° to the vertical scale of the striations.



(a) 10.5% depletions

(b) 11% depletions



(c) 12% depletions

Figure 5.16: $f_oF2 = 10.04$ MHz, where 12% striations are able to cause ducting, and 11% causing total internal reflection, completely redirecting the ray.

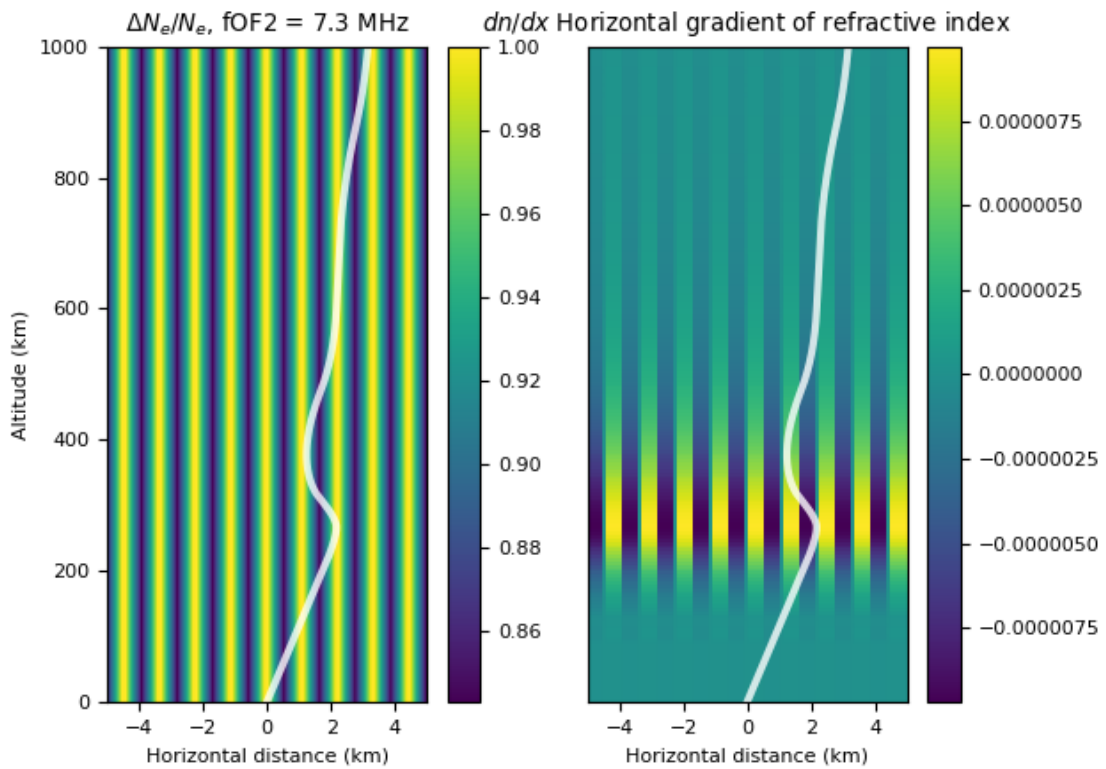
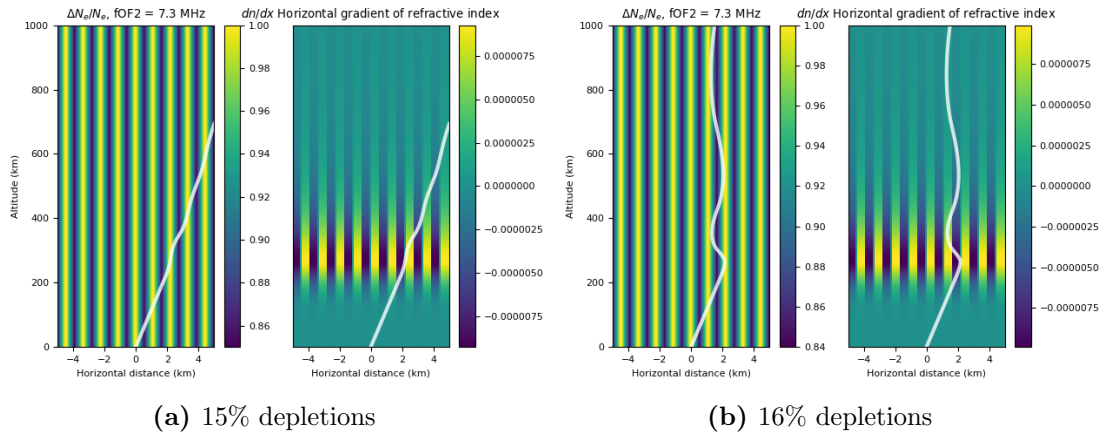


Figure 5.17: $f_oF2 = 7.3$ MHz, where 15.7% striations are able to duct the ray. 15% is able to slightly modify the ray path, but not enough to propagate along the striation.

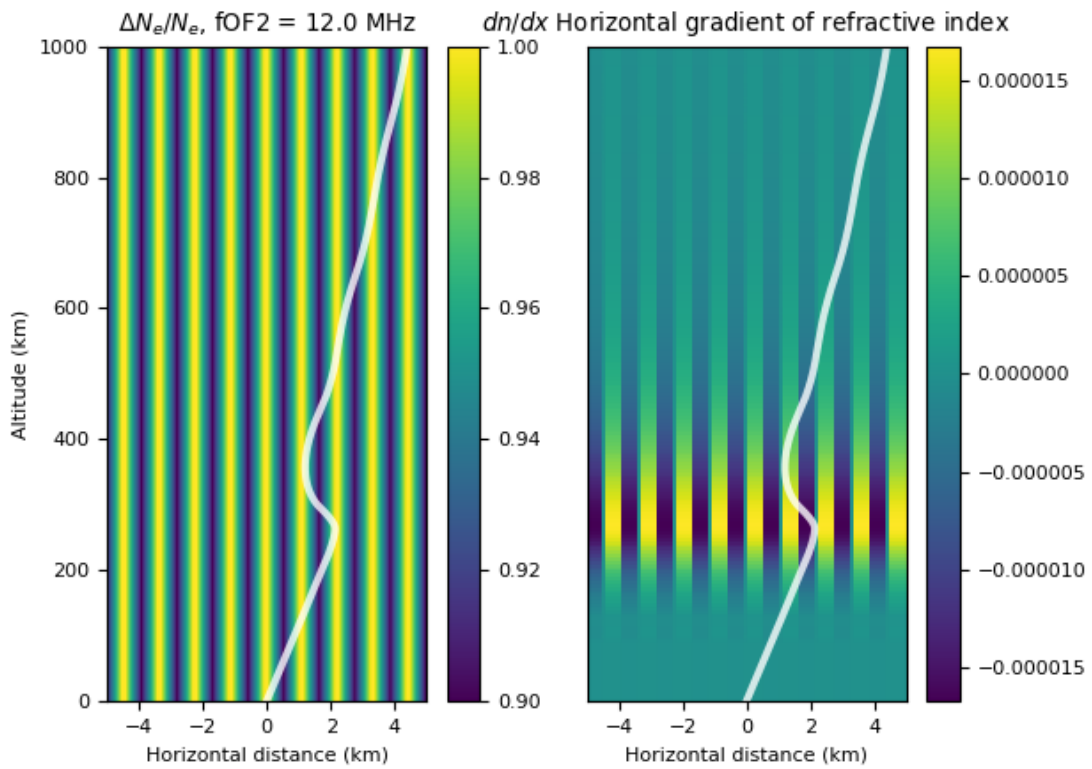
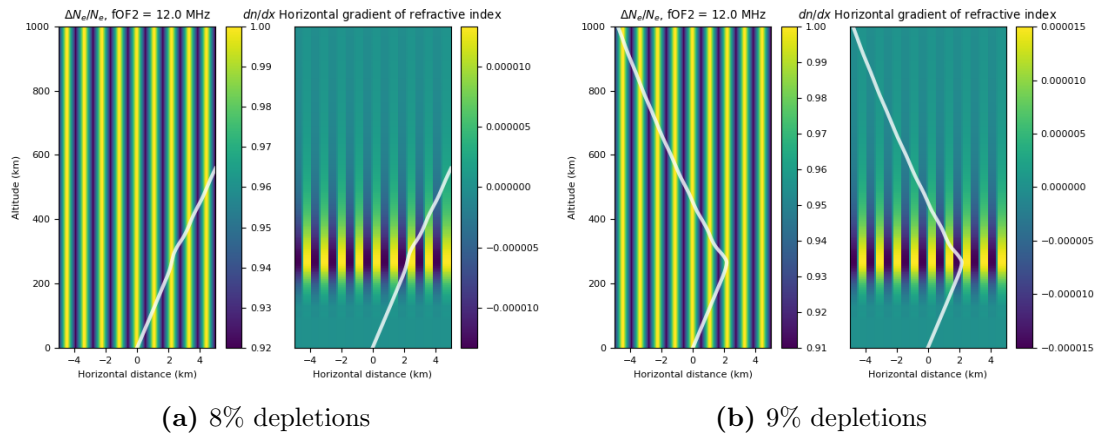


Figure 5.18: $f_oF2 = 12$ MHz. Similar to figure 5.16, 9% depletions cause total internal reflection, while 10% is able to duct the ray.

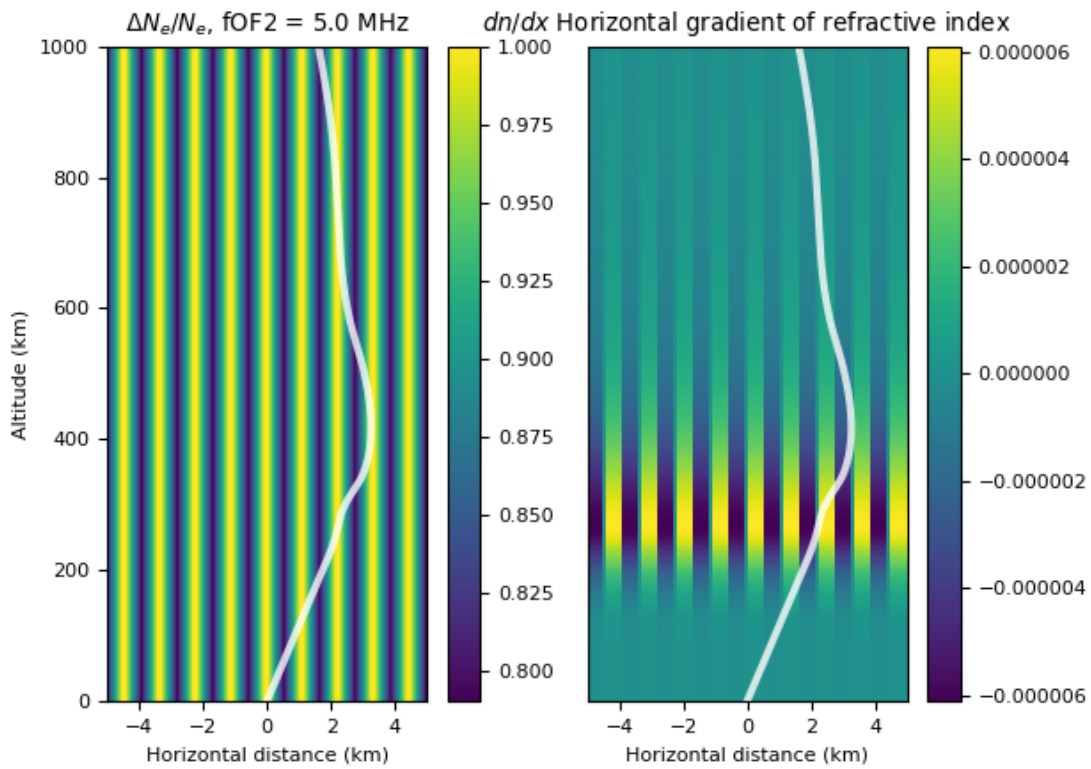
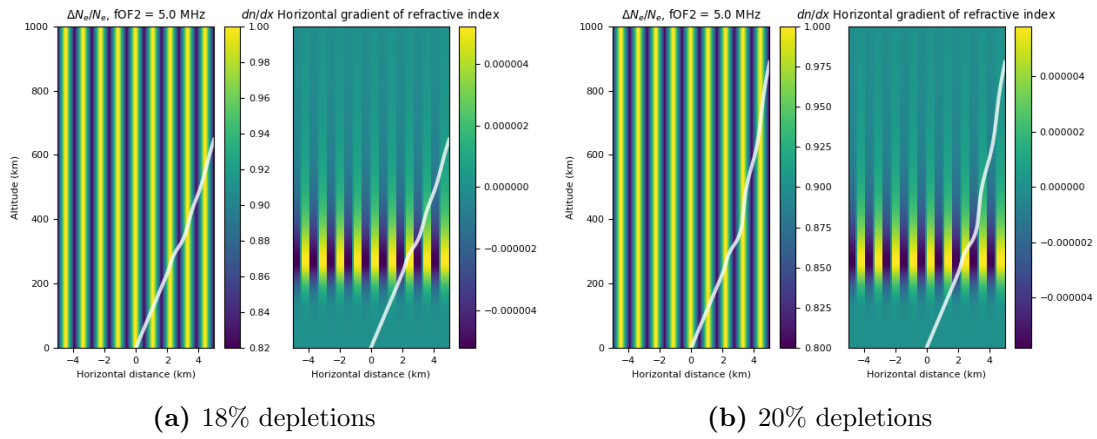


Figure 5.19: $f_oF2 = 5$ MHz. 21% striations are necessary to cause ducting, although 20% depletions also significantly modify the ray path.

Chapter 6

Conclusions and outlook

The aim of this thesis was to study the characteristics of WAILEs observed during a heating experiment at the EISCAT Tromsø Heating facility on 27 November 2014. It was found that WAILEs were excited within 0.5 degrees of magnetic zenith, both during X- and O-mode heating. This is the first sub radar beam resolution determination of the elevation extent of this phenomenon.

WAILEs as a phenomenon are suggested to be caused by AFAIs generated during heating, which cause sufficient modifications in refractive index to duct the UHF radar waves, leading to the observed enhanced backscatter [Rietveld and Senior, 2019]. A ray tracing simulation was done based on this explanation, using the IRI model from the time of the experiment, with striations between 5-20% and a horizontal length scale of 500m. This simulation showed that 12% density depletions were sufficient to refract a 930 MHz radio wave propagated at 0.5 degrees to magnetic zenith along the interface of the depletion and the background ionosphere at $f_oF2 = 10.04$ MHz, which was the measured value for the time of the experiment.

The low temporal resolution and low SNR of the data meant that it was not possible to determine any trends in the growth and decay times of the excitation. The electron temperature data from the experiment was also modelled. However, the model function was not able to fit the time evolution of electron temperatures during heating, so electron temperature results are not presented.

6.1 Outlook and further work

This study was able to find the first sub-antenna beam resolution results for the angular width of WAILEs observed during heating. The phenomenon on the whole, however, remains somewhat of a mystery, and is an intriguing topic for further investigation. First and foremost, more experiments of similar design under different conditions and with measurements from other diagnostic instruments such as the SuperDARN Hankasalmi radar would allow for the creation of a better model, which could help determine the viability of the suggested explanation of UHF radar beam ducting, determine characteristic growth and decay time of

WAILEs, and investigate any relations between f_oF2 and angular width. WAILEs are preferentially excited during X-mode heating, but under certain circumstances (such as the experiment detailed in this thesis) are also observed during O-mode heating. Studying the characteristics of WAILEs observed during O-mode heating and the conditions necessary for them to be generated would also be a very interesting line of study. A natural continuation of this thesis work would be to further develop the ray tracing simulation, including characterizing the refractive index gradient required to cause ray ducting, and studying the variation in the range of angles ducted by striations of different amplitudes. WAILEs are suggested to be correlated to AFAIs generated during X-mode heating, but this phenomenon is also unexplained. Gaining a better understanding of the mechanisms that generate AFAIs during X-mode heating is therefore very important for shedding light on the cause of WAILEs. An in-situ experiment similar to that detailed in [Kelley et al., 1995] for X-mode heating at a high latitude facility such as the Tromsø Heating facility or HAARP (Gakona, Alaska) would be very interesting and enlightening regarding the characteristics of X-mode AFAIs.

Appendix A

Full results

A.1 Temperature observed and modelled data

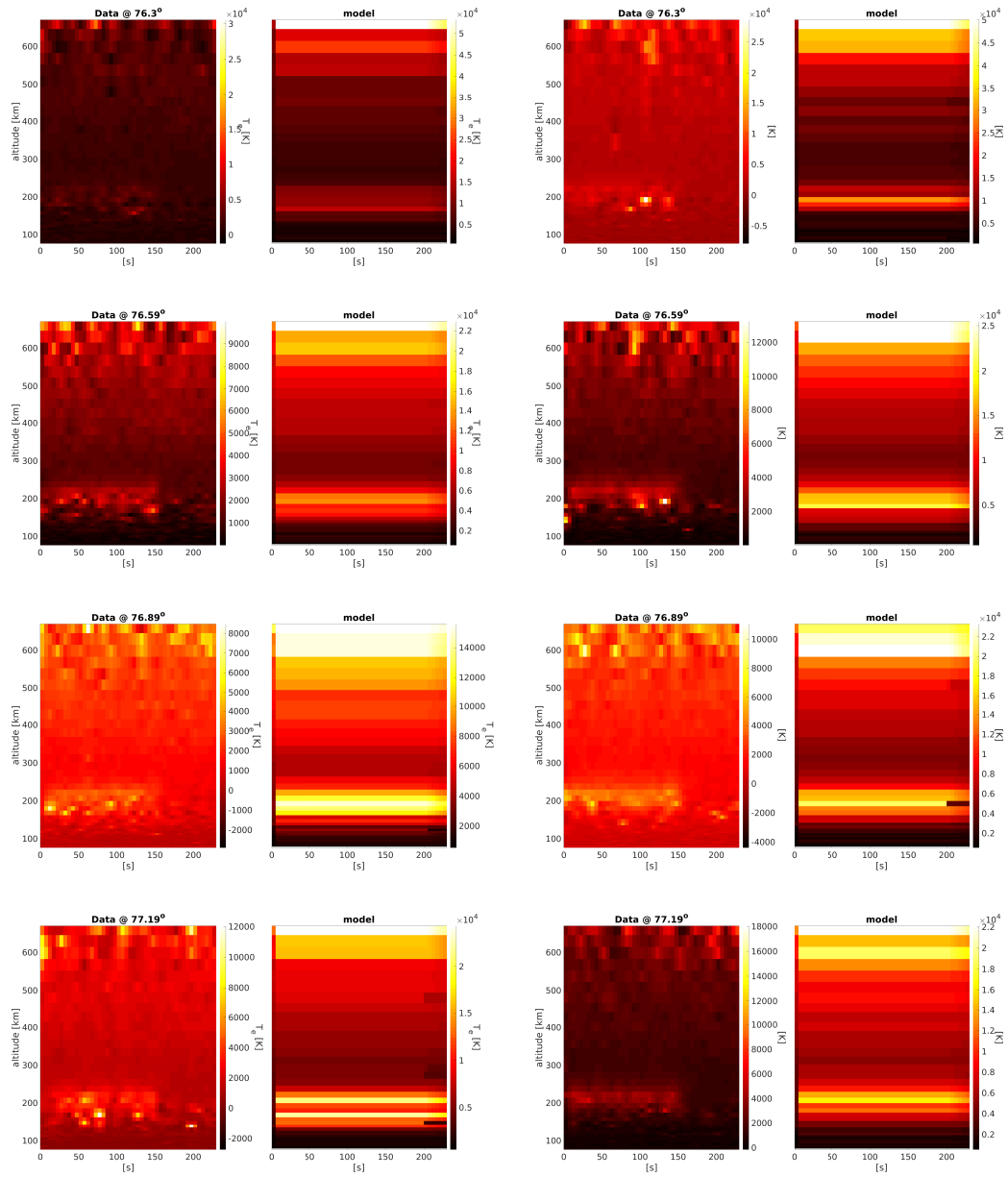


Figure A.1: Data and modelled electron temperature as ratio to background for first four scan angles

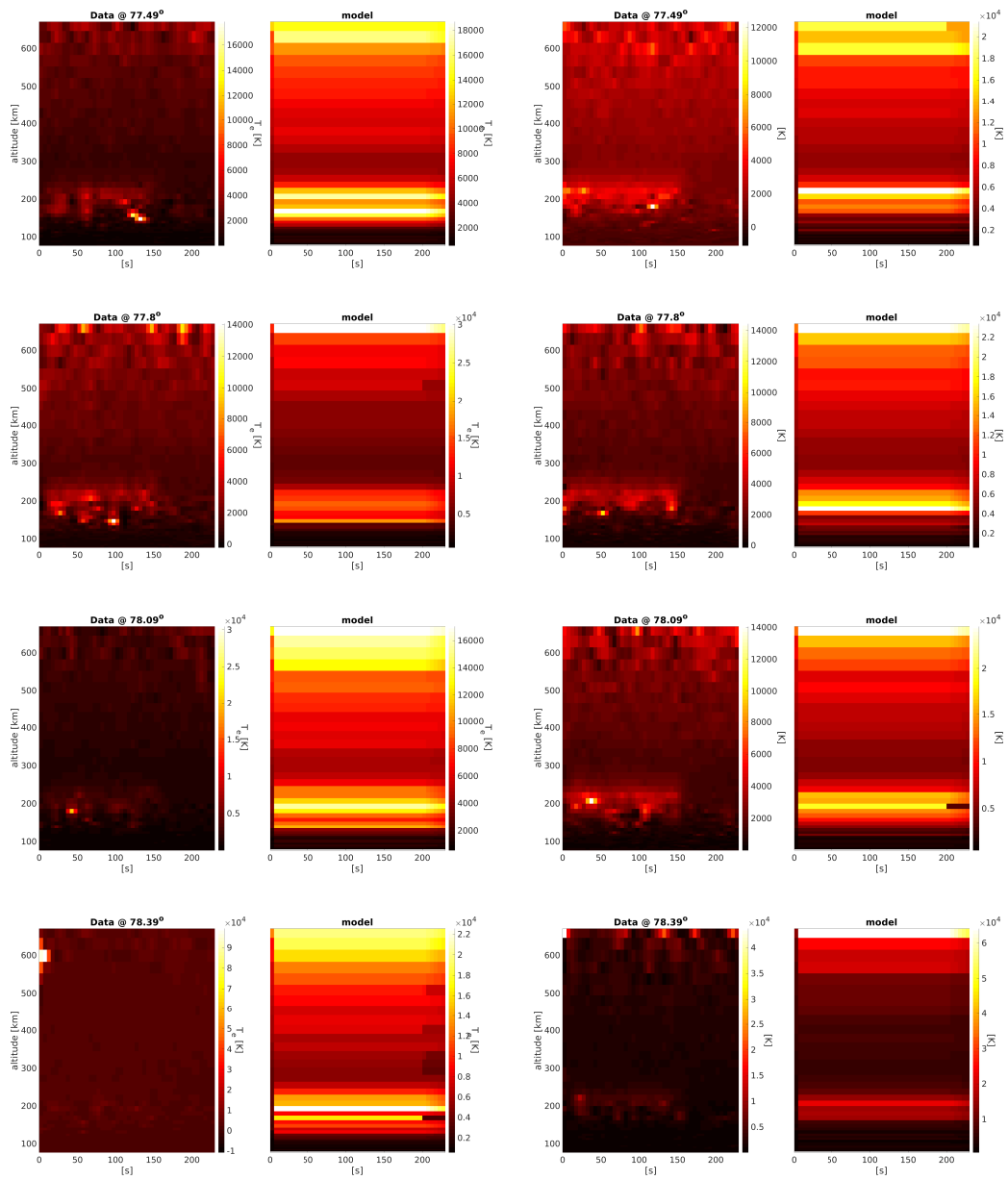


Figure A.2: Data and modelled electron temperature as ratio to background for remaining scan angles

A.2 Observed and modelled electron density at selected heights

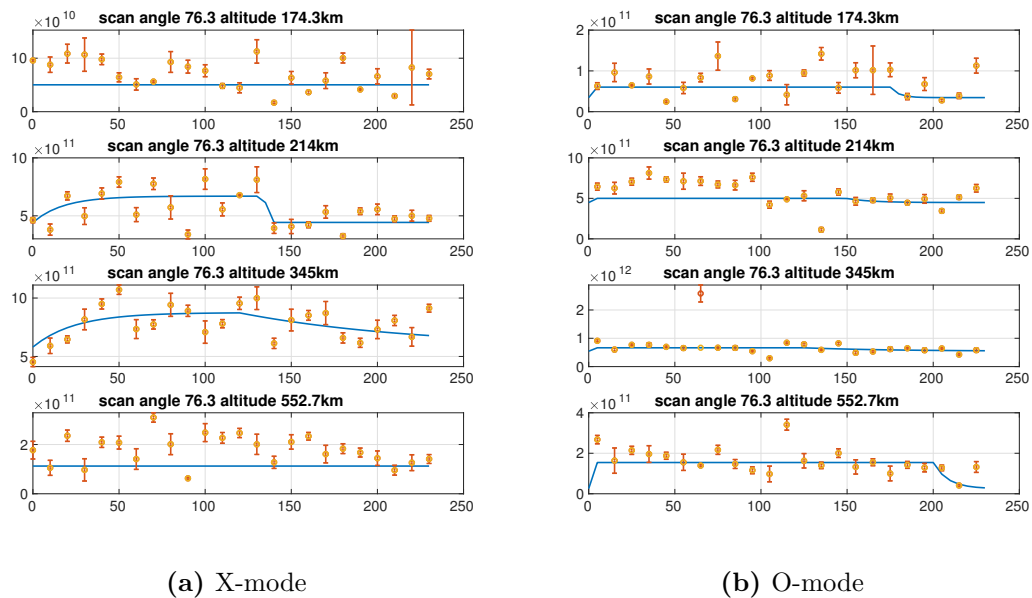


Figure A.3: 76.3°

A.2. OBSERVED AND MODELLED ELECTRON DENSITY AT SELECTED HEIGHTS⁵⁹

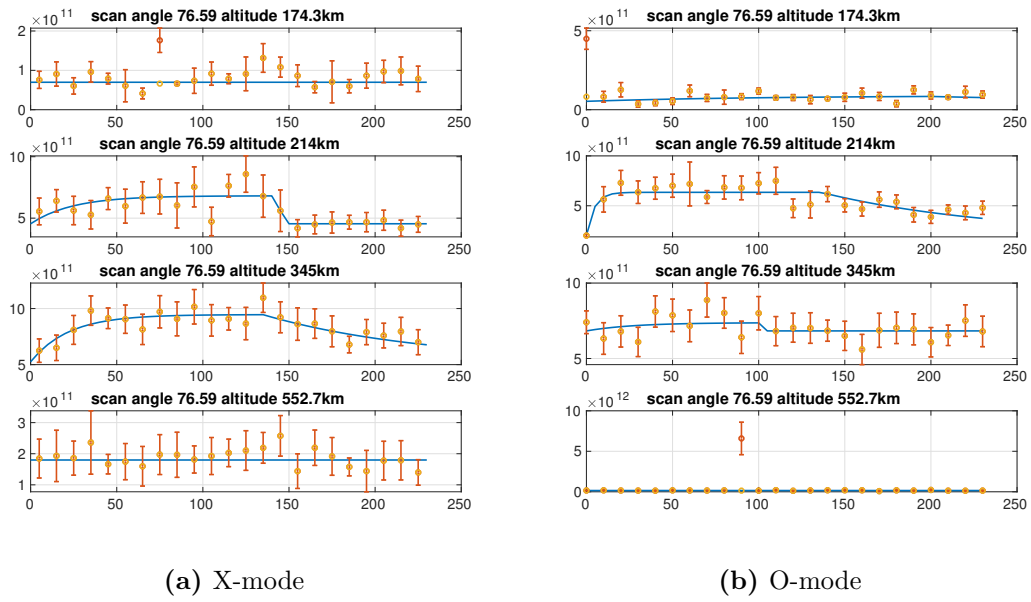


Figure A.4: 76.6°

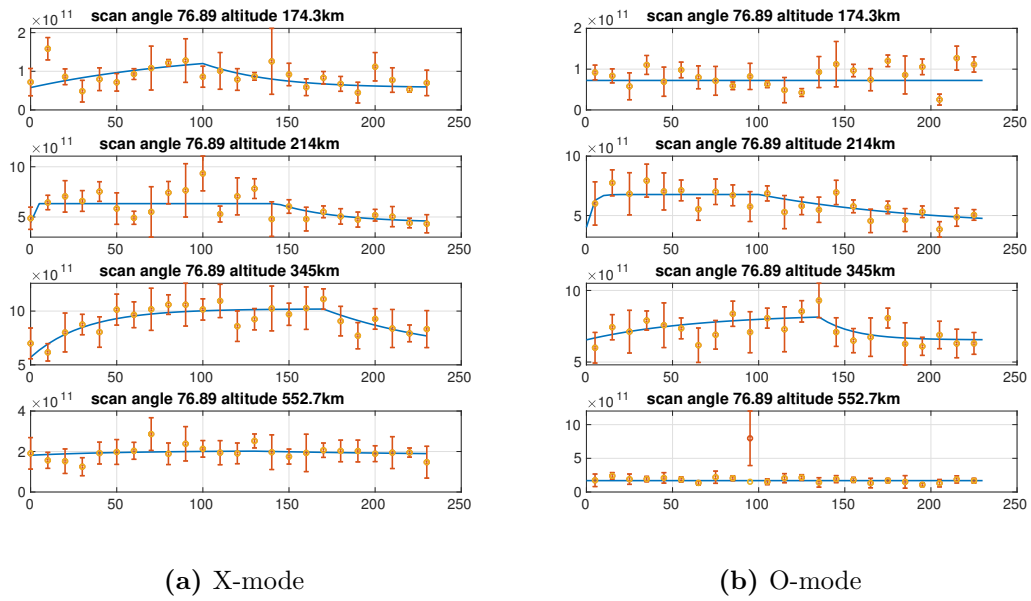


Figure A.5: 76.8°

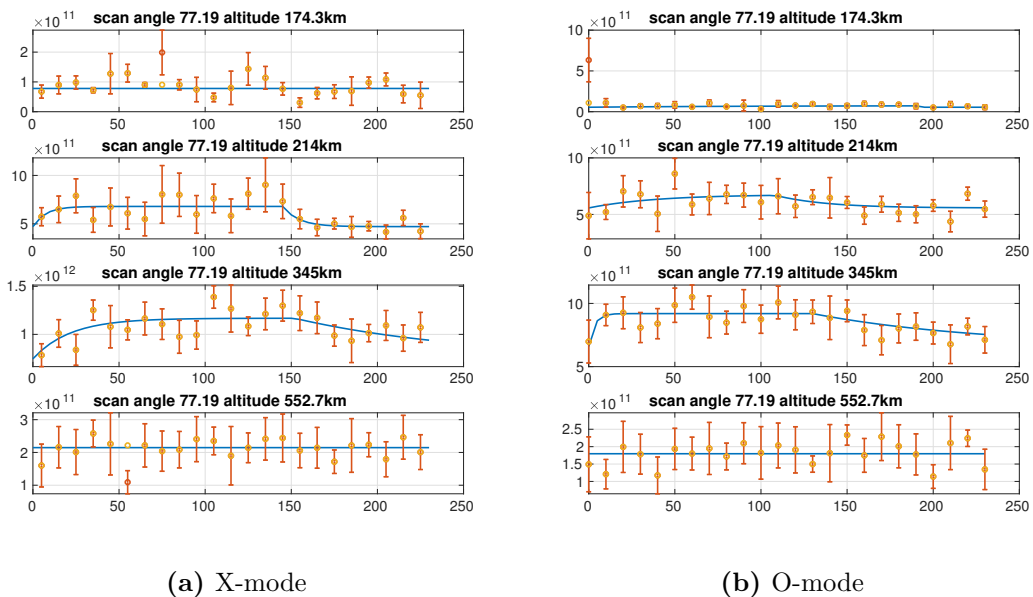


Figure A.6: 77.2°

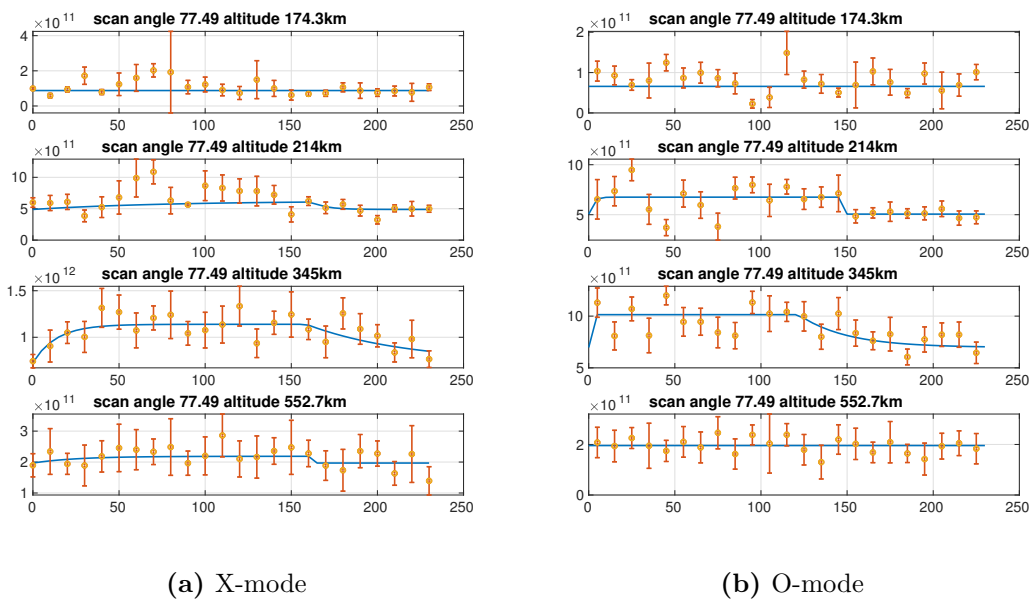


Figure A.7: 77.5°

A.2. OBSERVED AND MODELLED ELECTRON DENSITY AT SELECTED HEIGHTS61

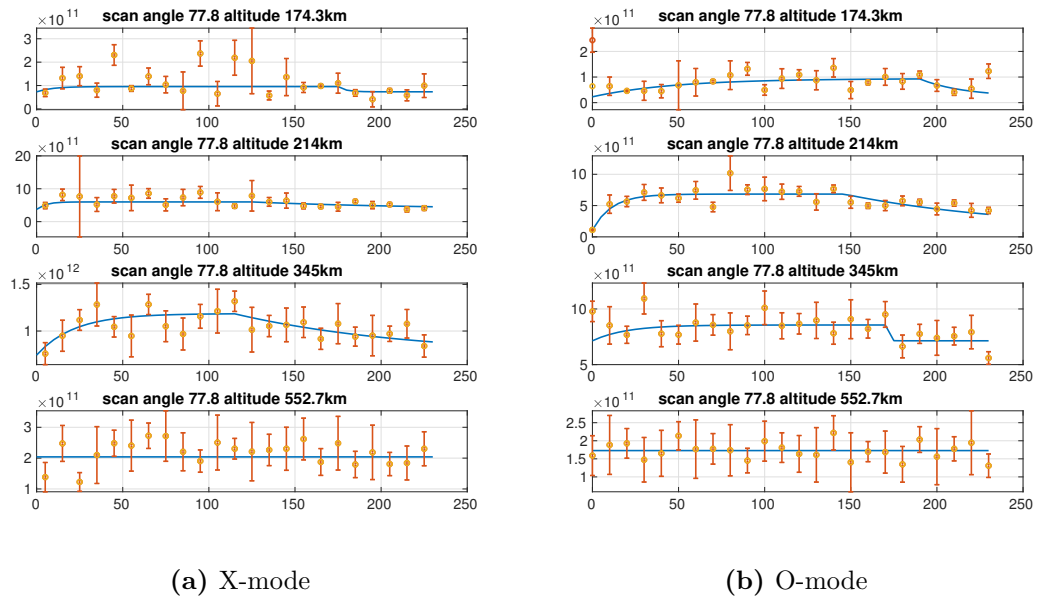


Figure A.8: 77.8°

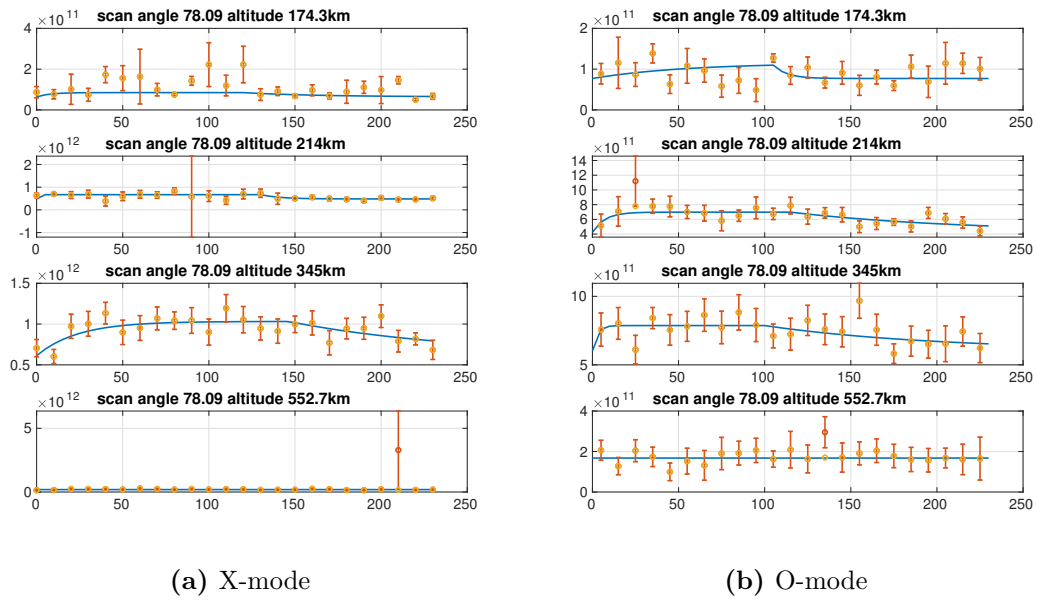
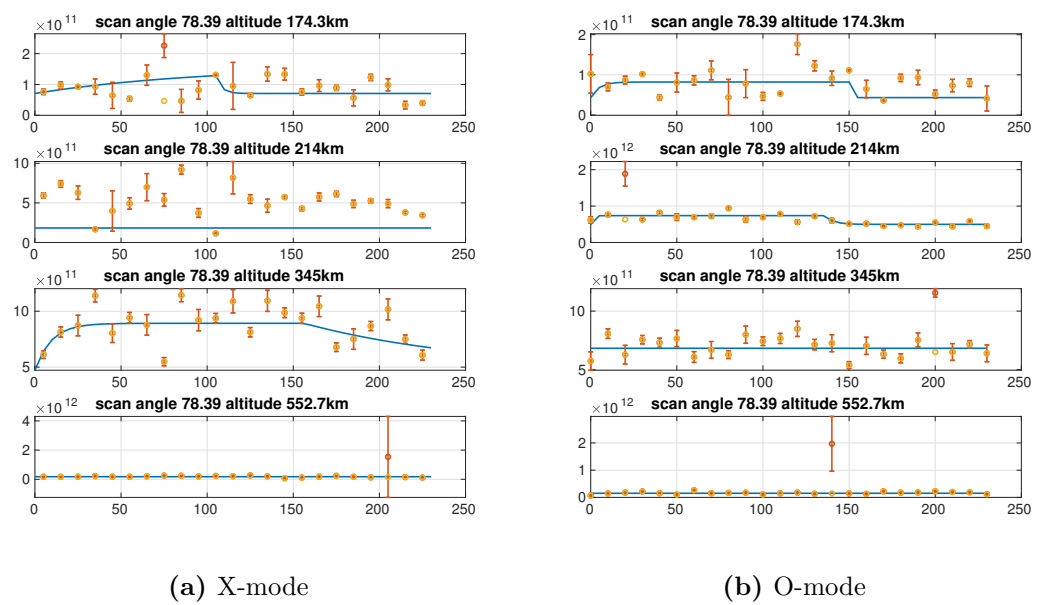


Figure A.9: 78.1°

Figure A.10: 78.4°

A.3 Modelled growth, decay and time delay parameters

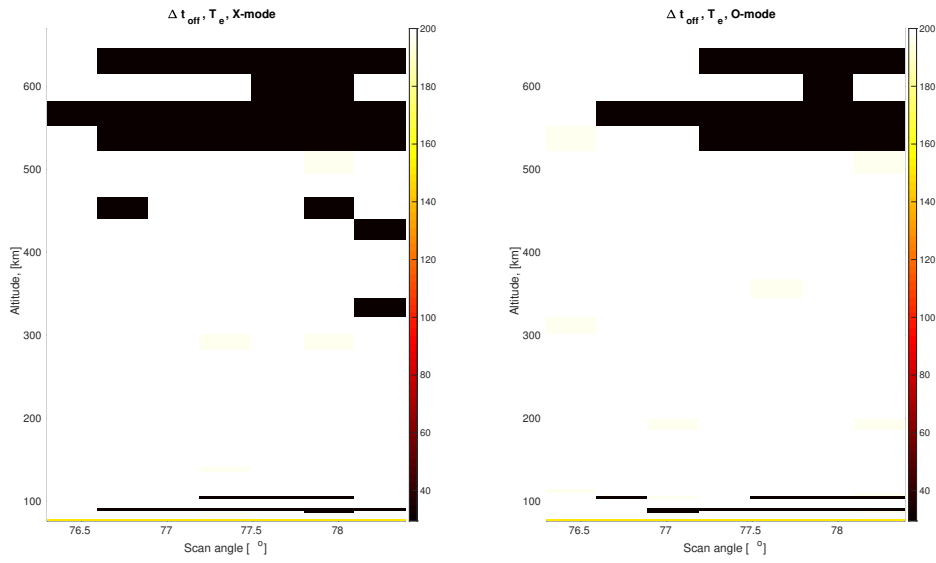


Figure A.11: Modelled pulse length, electron temperature data

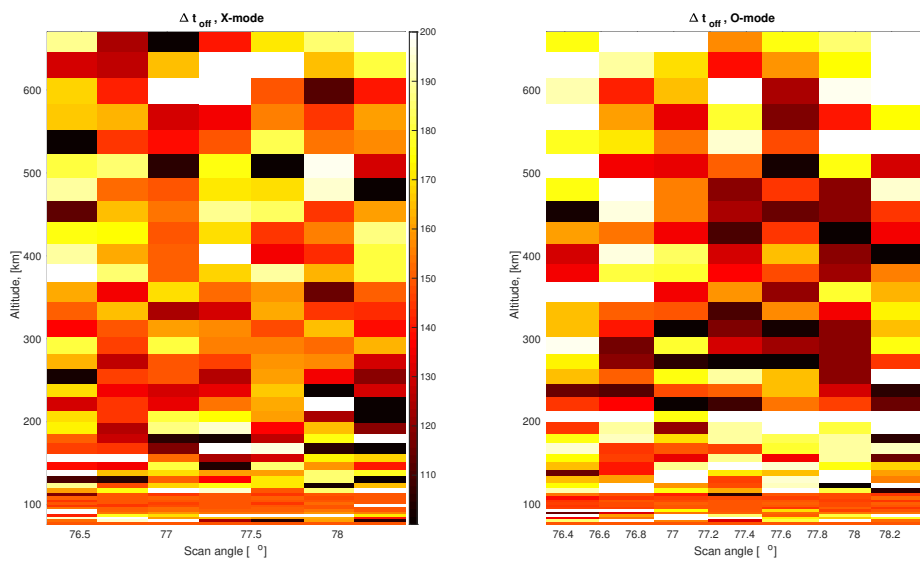


Figure A.12: Modelled pulse length, electron density data

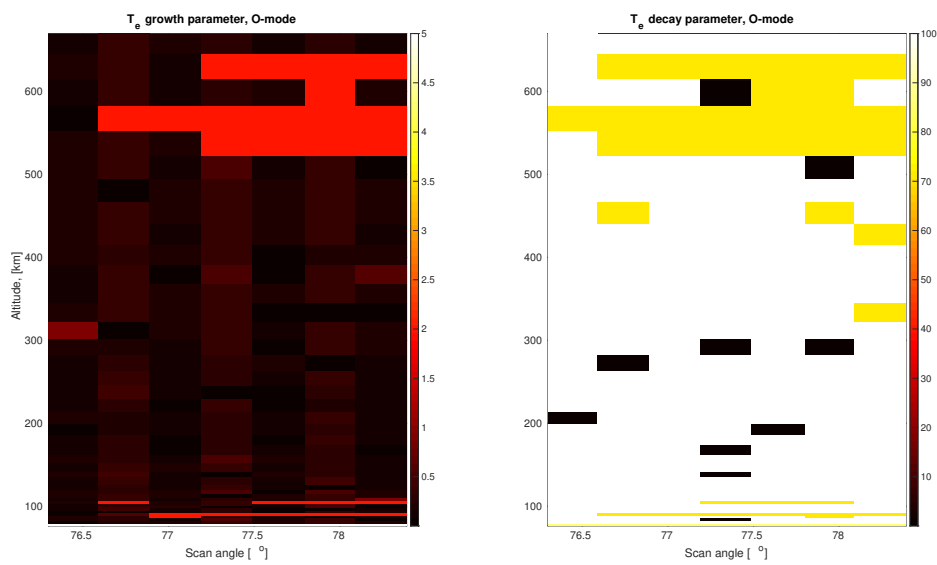


Figure A.13: Modelled growth and decay, electron temperature data

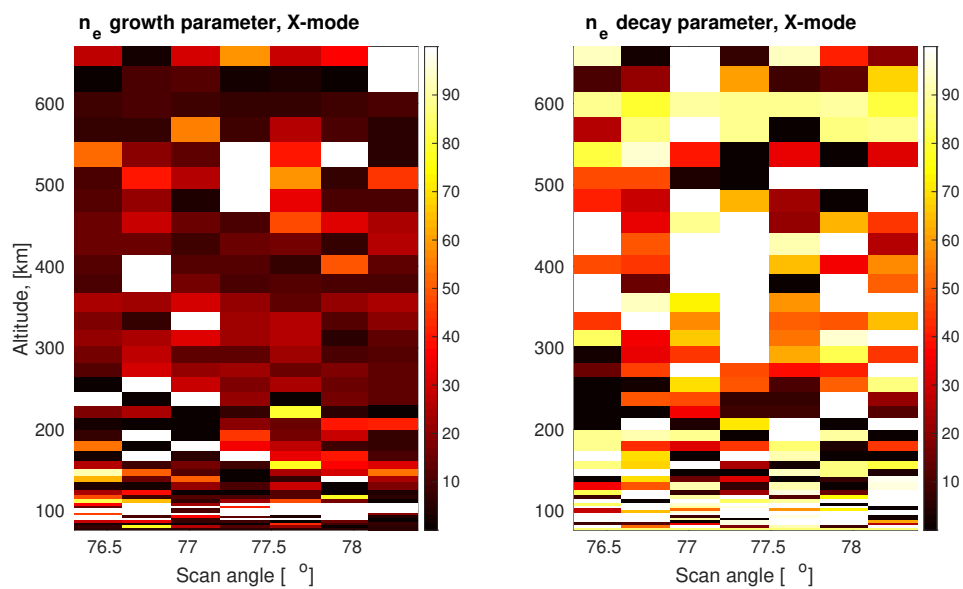


Figure A.14: Modelled growth and decay, electron density data

Appendix B

Programs written for this thesis

B.1 Matlab main file

HF20141127_main.m runs the superimposed epoch analysis, parameter optimization and analysis of WAILEs.

```
%% Script for the 20141127 Heating-experiment
% During this experiment EISCAT Heating was operated in
% a 150 s on
% 85 s off cycle, while the EISCAT UHF-radar ran beata
% in an
% 8-position 14-step long scan cycle with 5 s dwell-time
% on each
% position.
%
% This script requires the guisdap_param2cellregular tool
% function to run,
% in addition to EISCAT data in an appropriate directory
% , and the files
% HF20141127_dataread, HF20141127_wailes_paramfitne, and
% HF20141127_wailes_paramfitTe in the MATLAB path.

%% Adding data directories
work_dir = '/home/zoesaur/Documents/MATLAB/heating/
HF_20141127';
metadata_dir = [work_dir, '/Meta-data/'];
ISRdatadir = '/media/zoesaur/DATA/heating/2014-11-27
_beata_5@uhfa';
ionlinesdir = [ISRdatadir, '/rerun2_HF20141127/2014-11-27
_beata_5@uhfa'];
figdir = '/home/zoesaur/Documents/MATLAB/figs';

%% Load and format the EISCAT UHF-data
% outputs merged datasets
```

```

HF20141127_dataread

%% running fminsearch:
% outputs fitted parameters for a 5 parameter model of
  the data (function
% that gets fit is modelfunc_WAILEs)
HF20141127_wailes_paramfitne
HF20141127_wailes_paramfitTe

%% Splitting our modeled parameters up into separate data
  sets:
% where ***bg_mod is the model background value (par1)
% d***_mod is the modelled excitation (difference from
  background, par2)
% tau***_growth/decay are the modelled growth and decay
  times of the excitation
% dt*** is the decay point of the excitation
% ***max_mod is the modelled total value of the
  excitation (this is the one
% you wanna use to find ratio to background)

ne0bg_mod = squeeze(pars_bin_ne0(:, 1, :));
dne0_mod = squeeze(pars_bin_ne0(:, 2, :));
taune0_growth = squeeze(pars_bin_ne0(:, 3, :));
taune0_decay = squeeze(pars_bin_ne0(:, 4, :));
dt_ne0 = squeeze(pars_bin_ne0(:, 5, :));
ne0max_mod = ne0bg_mod + dne0_mod;

neXbg_mod = squeeze(pars_bin_neX(:, 1, :));
dneX_mod = squeeze(pars_bin_neX(:, 2, :));
tauneX_growth = squeeze(pars_bin_neX(:, 3, :));
tauneX_decay = squeeze(pars_bin_neX(:, 4, :));
dt_neX = squeeze(pars_bin_neX(:, 5, :));
neXmax_mod = neXbg_mod + dneX_mod;

Te0bg_mod = squeeze(pars_bin_Te0(:, 1, :));
dTe0_mod = squeeze(pars_bin_Te0(:, 2, :));
tauTe0_growth = squeeze(pars_bin_Te0(:, 3, :));
tauTe0_decay = squeeze(pars_bin_Te0(:, 4, :));
dt_Te0 = squeeze(pars_bin_Te0(:, 5, :));
Te0max_mod = Te0bg_mod + dTe0_mod;

TeXbg_mod = squeeze(pars_bin_TeX(:, 1, :));
dTeX_mod = squeeze(pars_bin_TeX(:, 2, :));
tauTeX_growth = squeeze(pars_bin_TeX(:, 3, :));
tauTeX_decay = squeeze(pars_bin_TeX(:, 4, :));
dt_TeX = squeeze(pars_bin_TeX(:, 5, :));
TeXmax_mod = TeXbg_mod + dTeX_mod;

```

```

%% creating full data sets based on the models:

ne3D0_mod = zeros(8, 47, 42);
ne3DX_mod = zeros(8, 47, 42);
Te3D0_mod = zeros(8, 47, 42);
Te3DX_mod = zeros(8, 47, 42);

for i_el = 1:8
    for i_z = 1:42
        ne3D0_mod(i_el, :, i_z) = modelfunc_wailes(
            pars_bin_ne0(i_el, :, i_z), t_parfit);
        ne3DX_mod(i_el, :, i_z) = modelfunc_wailes(
            pars_bin_neX(i_el, :, i_z), t_parfit);
        Te3D0_mod(i_el, :, i_z) = modelfunc_wailes(
            pars_bin_Te0(i_el, :, i_z), t_parfit);
        Te3DX_mod(i_el, :, i_z) = modelfunc_wailes(
            pars_bin_TeX(i_el, :, i_z), t_parfit);
    end
end

end

%% Deconvolution
HF20141127_deconv

%% Calculating standard deviations, using this to check
deconvolution:
std_beam = std(Enorm_UHF);

std_Xwailes = std(norm_interp_Xwailemod);
std_0wailes = std(norm_interp_0wailemod);

std_deconv_Xwailes = std(norm_deconv_Xwailes);
std_deconv_0wailes = std(norm_deconv_0wailes);

% since both the signal and the beam are *approximately*
gaussian, we can
% use sigma_waile - sigma_beam to see how good our
deconvolution is:
test_deconv_Xwailes = std_beam - std_Xwailes;
test_deconv_0wailes = std_beam - std_0wailes;

%%

exciteelsX = zeros(2, 42);
exciteels0 = zeros(2, 42);
for i_z = 1:42

```

```

[min1X, idx1X] = min(abs(std_deconv_Xwailles(i_z) -
    norm_deconv_Xwailles(1:8, i_z)));
[min2X, idx2X] = min(abs(std_deconv_Xwailles(i_z) -
    norm_deconv_Xwailles(9:16, i_z)));

exciteelsX(:, i_z) = [el_interp(idx1X) el_interp(9+
    idx2X)];

[min10, idx10] = min(abs(std_deconv_0wailles(i_z) -
    norm_deconv_0wailles(1:8, i_z)));
[min20, idx20] = min(abs(std_deconv_0wailles(i_z) -
    norm_deconv_0wailles(9:16, i_z)));

exciteels0(:, i_z) = [el_interp(idx10) el_interp(9+
    idx20)];
end
%%
critanglesX = squeeze(exciteelsX(2, :) - exciteelsX(1, :)
    );
critangles0 = squeeze(exciteels0(2, :) - exciteels0(1, :)
    );
stds = [h(:), std_deconv_Xwailles(:), critanglesX(:),
    std_deconv_0wailles(:), critangles0(:)];

%%
[MX, IX] = max(neXmax_mod(:,30:40) ./ ne_bgavgd(30:40) ',
    [], 2, 'omitnan');
maxheightX = h(IX);

[M0, I0] = max(ne0max_mod(:,30:40) ./ ne_bgavgd(30:40) ',
    [], 2, 'omitnan');
maxheight0 = h(I0);

TmaxX = max(Te3DmX(:, :, 20:30), [], 'all');
Tmax0 = max(Te3Dm0(:, :, 20:30), [], 'all');

nemaxvals = [el_values(:), MX(:), maxheightX(:), M0(:),
    maxheight0(:)];

```

B.2 Superimposed epoch analysis

HF20141127_dataread.m reads the GUISDAP analysed data into matlab and performs the superimposed epoch analysis, sorting the data into a composite set over all scan angles, altitudes and time after heater on.

```
%% Readin attempt 2
```

```

% Notes to self:
%
% Experiment starts at 11:31, ends at 14:45 (alternating
  X/O pulses)
% 150s on, 85 s off = 235s exp time, or 48-5s increments
% X + 0 mode obs time = 470s, or 94-5s increments
%
% median elevation 77.2 (magnetic zenith). 0.3-ish scan
  increments. scan
% over total of 2 degrees
% 8-position 14-step long scan cycle with 5 s dwell-time
  on each
% position.
%
% First 10ish X+0-mode pulses are good data, so end of
  good data run is at
% 235*2*10 = 4700 s --> 12:49:20
%
% amount of scan cycles in usable data window: 14*5 = 70s
  per cycle -->
% 4700/70 = 67.1429 --> 67 full cycles + 2 full steps and
  one partial step (?)
%
% This script requires the guisdap_param2cellregular tool
  to run.
%% Data read-in
cd(ISRdatadir)
mfiles = dir('*.mat');

% Data read:
[h, t, ne, Te, Ti, vi, dne, dTe, dTi, dvi, az, el, T,
  ranges] = guisdap_param2cell2regular(mfiles);

cd(work_dir)
%% Setting up time series and indexes for the experiment,
  so the data merges correctly:

ton_unix = 1417087860; % 20141127 11:31:00 in unix time
T_on = [2014 11 27 11 31 00]; % Heater on for alternating
  X/O-mode experiment
T_off = [2014 11 27 14 45 00]; % End of alternating x/O-
  mode experiment
T_endgooddata = [2014 11 27 12 49 20]; % endpoint of
  usable data

% Decimal hour time:
% Converting from unix time to decimal hours:
t_obs = rem(t/3600, 24);

```

```

% start of heating experiment:
t_on = 10 + 5/60 + [0 : 235 : (21*60)]/3600;

t_off = t_on + 150/3600;

% Finding array indexes corresponding to beginning and
  end of experiment:
idx_Ton_exp = find(T(:, 4)==11 & T(:, 5)==31, 1);
idx_Toff_exp = find(T(:, 4)==14 & T(:, 5)==45, 1);
idx_Tendgooddata = find(T(:, 4)==12 & T(:, 5)==49, 5);
idx_Tendgooddata = idx_Tendgooddata(4);

% Array of elevations:
el_values = [76.3 76.59 76.89 77.19 77.49 77.8 78.09
  78.39];

% One period of scan cycle, starting at heater on:
scancycle = [el(idx_Ton_exp:idx_Ton_exp+13)];

% Creating array that just repeats the period starting
  from heater on, and
% ending at the end of the good data run (removing last
  values manually,
% since experiment ends on partial scan cycle).
el_r = repmat(scancycle, 1, 68);
el_r(941:end) = [];

% Do the same, but using values 1-8 instead for easy
  indexing
idx_scancycle = [4 3 2 1 2 3 4 5 6 7 8 7 6 5];
idx_scan = repmat(idx_scancycle, 1, 68);
idx_scan(941:end) = [];

% making an array to index time scale in terms of length
  of pulses we're
% trying to merge:
idx4dt = repmat((1:94), 1, 10);

%%
nDt = 94;

% Counter for how many measurements we have in each
  position:
n3Dm = zeros(length(el_values), nDt, length(h));

% creating arrays to merge data into:
ne3Dm = zeros(length(el_values), nDt, length(h));

```

```

Te3Dm = zeros(length(el_values), nDt, length(h));
Ti3Dm = zeros(length(el_values), nDt, length(h));

% arrays for merged SD data:
dne3Dm = zeros(8, nDt, length(h));
dTe3Dm = zeros(8, nDt, length(h));
dTl3Dm = zeros(8, nDt, length(h));

% time 0 of experiment, 1 time step before heater on--
% this is so that the
% first step read in for-loop is
t0_exp = idx_Ton_exp - 1;

% Running epoch analysis for 10 pulses (of 94 5s
% increments-- don't panic,
% you were smarter when you wrote this)
for i_exp = 1:(940)

    % Counter for how many measurements we have in each
    % position:
    n3Dm(idx_scan(i_exp), idx4dt(i_exp), :) = squeeze(
        n3Dm(idx_scan(i_exp), idx4dt(i_exp), :)) + ones(
            size(ne(:, t0_exp + i_exp))));

    % Merging in data:
    ne3Dm(idx_scan(i_exp), idx4dt(i_exp), :) = squeeze(
        ne3Dm(idx_scan(i_exp), idx4dt(i_exp), :)) + ne(:,
            t0_exp + i_exp);
    Te3Dm(idx_scan(i_exp), idx4dt(i_exp), :) = squeeze(
        Te3Dm(idx_scan(i_exp), idx4dt(i_exp), :)) + Te(:,
            t0_exp + i_exp);
    Ti3Dm(idx_scan(i_exp), idx4dt(i_exp), :) = squeeze(
        Ti3Dm(idx_scan(i_exp), idx4dt(i_exp), :)) + Ti(:,
            t0_exp + i_exp);

    % Merging SD of data:
    dne3Dm(idx_scan(i_exp), idx4dt(i_exp), :) = squeeze(
        dne3Dm(idx_scan(i_exp), idx4dt(i_exp), :)) + dne
        (:, t0_exp + i_exp);
    dTe3Dm(idx_scan(i_exp), idx4dt(i_exp), :) = squeeze(
        dTe3Dm(idx_scan(i_exp), idx4dt(i_exp), :)) + dTe
        (:, t0_exp + i_exp);
    dTi3Dm(idx_scan(i_exp), idx4dt(i_exp), :) = squeeze(
        dTi3Dm(idx_scan(i_exp), idx4dt(i_exp), :)) + dTi
        (:, t0_exp + i_exp);

end

```

```

% dividing our data sets by the amount of values in each
  position to account for overlapping data:
ne3Dm = ne3Dm./n3Dm;
Te3Dm = Te3Dm./n3Dm;

%% splitting data into separate parts for X- and O-mode
% Time series:
DtX0 = 47;
t_parfit = 0:5:230;

ne3Dm0 = ne3Dm(:, 1:47, :);
ne3DmX = ne3Dm(:, 48:94, :);
Te3Dm0 = Te3Dm(:, 1:47, :);
Te3DmX = Te3Dm(:, 48:94, :);

% splitting up the SD data as well:
dne3Dm0 = dne3Dm(:, 1:47, :);
dne3DmX = dne3Dm(:, 48:94, :);
dTe3Dm0 = dTe3Dm(:, 1:47, :);
dTe3DmX = dTe3Dm(:, 48:94, :);

%% Mean background (taken from last 5 time steps before
  Ton at 11:31)
% Maybe don't do this? Use average values between pulses
  (seems potentially
% risky tho
ne_bgavgd = mean(ne(:, 1088:1091), 2);
Te_bgavgd = mean(Te(:, 1088:1091), 2);

```

B.3 Parameter optimization

modelfunc_wailes.m describes the model function fit to the observed data for each altitude and elevation.

```

function modelfunc = modelfunc_wailes(pars, t)
  % modelfunc_wailes - a model curve with unknown
  % parameters to be fit to
  % WAILE data.
  %
  % Input:
  % pars -- unknown parameters to fit:
  % 1: Background (starting) value
  % 2: excitation/peak value (difference)
  % 3: length/shape of excitation
  % 4: length/shape of decay

```

```

    % 5: start of decay. This should really stay at
    % 150 no matter what
    % t -- time series. Needs to have same dimensions as
    % variable 'Y' in
    % errorfunc_wailes (1x47)

    modelfunc = pars(1) + pars(2)*(1 - exp(-abs(t/pars(3)
    ))) .* exp(-max(0, t-pars(5))/pars(4));

```

```
end
```

errorfunc_wailes.m is the least-mean-square error function used to optimize parameters for each set of observed data.

```

function errorfunc = errorfunc_wailes(pars, Y, t, sigma)
    % Least mean square error of a model function to be
    % fit to WAILE data
    %
    % Input:
    % pars -- unknown fit parameters
    % Y -- WAILE data, Te or ne for a single elevation
    % and altitude in time
    % (in practice, this matrix should be a 1 x 47 matrix
    % )
    % t -- time series. Needs to have same dimensions as
    % variable 'Y' in
    % modelfunc_wailes (1x47)
    % sigma-- sigma data from EISCAT. not very accurate,
    % so made to be
    % optional.

    switch nargin
        case 3
            errorfunc = nansum(Y - (modelfunc_wailes(pars
            , t)).^2);
        case 4
            errorfunc = nansum(((Y - modelfunc_wailes(
            pars, t)).^2)./(sigma.^2));
    end
end
end

```

HF20141127_wailes_paramfitne.m and HF20141127_wailes_paramfitTe.m run `fminsearchbnd` [D'Arrico, 2012a] for the electron density and temperature data for each altitude and elevation.

```

%% Running fminsearch over all altitudes and elevations,
    for ne and Te
% defining the values we need to use for the fit:

```

```

t_parfit = 0:5:230; % time series
tlim = 150; % time limit-- in case we need it

pars_0 = [0; 0; 5; 85; 150]; % initial guesses for the
    parameters we're trying to find
% ne_bgavgd = mean(ne_bg, 2); % average of our background
    (heater off) data, for starting guesses

% setting lower and upper bounds for the parameters:
lb_ne = [0; 0; 0; 0; 100];
ub_ne = [0; 0; 100; 100; 200];

% setting up options for the fminsearch function:
options = optimset('Display', 'off', 'MaxFunEvals', 15e4,
    'MaxIter', 15e4);

%% Electron density, 0-mode
% Creating arrays to store parameters in:
pars_bin_ne0 = zeros(size(ne3Dm0, 1), 5, size(h, 1));
exitflag_bin_ne0 = zeros(size(ne3Dm0, 1), 1, size(h, 1));

% running fminsearch for each altitude and elevation:
for i_el = 1 : size(ne3Dm0, 1) % loop over every
    elevation
    for i_z = 1 : size(h, 1) % then over every altitude

        % filloutliers replaces any extreme outlier values
            with nearest mean:
        data = filloutliers(ne3Dm0(i_el, :, i_z), 'nearest'
            , 'mean');

        % setting the starting guesses that are most easily
            estimated based
        % on the data set:
        pars_0(1) = ne_bgavgd(i_z);
        pars_0(2) = max(data) - pars_0(1);
        ub_ne(1) = 3*pars_0(1);
        ub_ne(2) = 3*pars_0(2);
        % running fit:
        % [pars_final, fval, exitflag, output] = fminsearch
            (@(pars) errorfunc_wailes(pars, data, t_parfit),
            pars_0, options);
        [pars_final, fval, exitflag, output] =
            fminsearchbnd(@(pars) errorfunc_wailes(pars,
            data, t_parfit, dne3Dm0(i_el, :, i_z)), pars_0,
            lb_ne, ub_ne, options);
        pars_bin_ne0(i_el, :, i_z) = pars_final;
    end
end

```

```

    exitflag_bin_ne0(i_el, :, i_z) = exitflag;

    % exitflag 0 means that a sufficient fit was not
    % reached within the
    % amount of iterations allowed. if any sets flag 0,
    % this will spit
    % which altitude-elevation pair was the problem
    % into the command line
    if exitflag == 0
        i_el, i_z, fval, output
    end
end
end

%% Electron density, X-mode:
% storage arrays:
pars_bin_neX = zeros(size(ne3DmX, 1), 5, size(h, 1));
exitflag_bin_neX = zeros(size(ne3DmX, 1), 1, size(h, 1));

for i_el = 1 : size(ne3DmX, 1) % loop over every
    elevation
        for i_z = 1 : size(h, 1) % then over every altitude

            data = filloutliers(ne3DmX(i_el, :, i_z), 'nearest'
                , 'mean');
            pars_0(1) = ne_bgavgd(i_z);
            pars_0(2) = max(data) - pars_0(1);
            ub_ne(1) = 3*pars_0(1);
            ub_ne(2) = 3*pars_0(2);

            % [pars_final, fval, exitflag, output] = fminsearch
            % (@(pars) errorfunc_wailes(pars, data, t_parfit),
            % pars_0, options);
            [pars_final, fval, exitflag, output] =
                fminsearchbnd(@(pars) errorfunc_wailes(pars,
                    data, t_parfit, dne3DmX(i_el, :, i_z)), pars_0,
                    lb_ne, ub_ne, options);
            pars_bin_neX(i_el, :, i_z) = pars_final;
            exitflag_bin_neX(i_el, :, i_z) = exitflag;

            if exitflag == 0
                i_el, i_z, fval, output
            end
        end
    end
end

%% Running fminsearch over all altitudes and elevations,

```

```

    for ne and Te
% defining the values we need to use for the fit:
t_parfit = 0:5:230; % time series
tlim = 150; % time limit-- in case we need it

pars_0 = [0; 0; 5; 85; 150]; % initial guesses for the
    parameters we're trying to find
% parameter 1 and 2 should be dependent on the data, so
    we just set these
% in the for-loops.

% lower and upper bounds for the parameters we're looking
    for:
lb_Te = [0; 0; 0; 0; 0;];
ub_Te = [0; 0; 100; 100; 200];
% setting up options for the fminsearch function:
options = optimset('Display', 'off', 'MaxFunEvals', 15e4,
    'MaxIter', 15e4);

% averageing our background temperature data to have a
    parameter estimate
% to work with:
%Te_bgavgd = mean(Te_bg, 2);

%% Electron temperature, 0-mode:
% storage arrays:
pars_bin_Te0 = zeros(size(Te3Dm0, 1), 5, size(h, 1));
exitflag_bin_Te0 = zeros(size(Te3Dm0, 1), 1, size(h, 1));

for i_el = 1 : size(Te3Dm0, 1) % loop over every
    elevation
    for i_z = 1 : size(h, 1) % then over every altitude

        % using filloutliers to adjust any extreme abnormal
            values and setting
        % our variable starting guesses for this iteration:
        data = filloutliers(Te3Dm0(i_el, :, i_z), 'nearest'
            , 'mean');
        pars_0(1) = Te_bgavgd(i_z);
        pars_0(2) = max(data) - pars_0(1);
        ub_Te(1) = 3*pars_0(1);
        ub_Te(2) = 3*pars_0(2);

        % Running the fit, storing the final parameters and
            exit flag:
        [pars_final, fval, exitflag, output] =
            fminsearchbnd(@(pars) errorfunc_wailes(pars,

```

```

        data, t_parfit), pars_0, lb_Te, ub_Te, options);
    pars_bin_Te0(i_el, :, i_z) = pars_final;
    exitflag_bin_Te0(i_el, :, i_z) = exitflag;

    % if fminsearch isn't able to complete the
    %   calcuation, it'll spit out
    % what altitude-elevation pair was the problem in
    %   the command line
    if exitflag == 0
        i_el, i_z, fval, output
    end
end
end

%% Electron temperature, X-mode:
% storage arrays:
pars_bin_TeX = zeros(size(Te3DmX, 1), 5, size(h, 1));
exitflag_bin_TeX = zeros(size(Te3DmX, 1), 1, size(h, 1));

for i_el = 1 : size(Te3DmX, 1) % loop over every
    elevation
        for i_z = 1 : size(h, 1) % then over every altitude

            % Culling outliers, setting variable start guesses:
            data = filloutliers(Te3DmX(i_el, :, i_z), 'nearest'
                , 'mean');
            pars_0(1) = Te_bgavgd(i_z);
            pars_0(2) = max(data) - pars_0(1);
            ub_Te(1) = 3*pars_0(1);
            ub_Te(2) = 3*pars_0(2);

            % Running fit:
            [pars_final, fval, exitflag, output] =
                fminsearchbnd(@(pars) errorfunc_wailes(pars,
                    data, t_parfit), pars_0, lb_Te, ub_Te, options);
            pars_bin_TeX(i_el, :, i_z) = pars_final;
            exitflag_bin_TeX(i_el, :, i_z) = exitflag;

            % telling me if there's a fit that doesn't run
            %   properly:
            if exitflag == 0
                i_el, i_z, fval, output
            end
        end
    end
end
end

```

B.4 Deconvolution

radar_beampattern.m creates a 2D model circular aperture radar antenna pattern based on an algorithm described in [Mahafza, 2000].

```
function [E, E_norm] = radar_beampattern(d, f, Beta)

% a function that creates a model beam pattern for a
% circular aperture
% radar, adapted from the circ_aperture function
% described in Radar Systems Analysis and design
% using MATLAB by Bassem R. Mahafza
%
% Input:
% d - antenna diameter [m] (diameter of EISCAT UHF:
% 32 m)
% f - frequency of radar [Hz] (EISCAT UHF:
% 926.6-930.5 MHz--> beata runs at 929.9 MHz)
% Beta - desired fr angular range-- optional
% parameter, if not
% included, default is [-pi:0.001:pi]

if nargin < 3 || isempty(Beta)
    Beta = -pi:0.001:pi;
end

% setting up required starting parameters:
c = 299792458; % speed of light in vacuum, [m/s]
lambda = c/f; % wavelength of radar
r = d/2; % radius of the radar
k = (2*pi)/lambda; % angular wavelength
J_1 = besselj(1, k*r*sin(Beta)); % bessel function of
% first kind

E = (2*pi*(r^2))*((2*J_1)./(k*r*sin(Beta)));
E_norm = E./max(abs(E));

end
```

HF_20141127_deconv.m deconvolves the antenna pattern created by radar_beampattern.m from the WAILE amplitude data at each altitude.

```
%% Interpolation of model and deconvolution of model data
% from beam pattern
% the aim of this program is to interpolate the modelled
% data for the
% WAILEs to a higher resolution, and then deconvolve the
```

```

    enhancement from
% the EISCAT UHF beam to find the true size of the WAILE
    in terms of aspect
% angle.
% needs to have the radar_beampattern.m function in
    filepath, and for
% HF20141127_main to have been run (although this might
    eventually get
% included in main)

%% Interpolating model data:
% size of interpolated data and beam pattern array:
n_interp = 16;

% creating an expanded array of elevation sample points
el_interp = linspace(el_values(1), el_values(8), n_interp
    );

% Empty array to write interpolated data to:
interp_Xwailemod = zeros(length(el_interp), 42);
interp_Owailemod = zeros(length(el_interp), 42);

% running interpolation over heights 2-41(1st and last
    range gate data are NaNs, so this is the easiest way
    to deal for now):
for i_z = 2:41
    interp_Xwailemod(:, i_z) = interp1(el_values,
        neXmax_mod(:, i_z), el_interp, 'pchip');
    interp_Owailemod(:, i_z) = interp1(el_values,
        neOmax_mod(:, i_z), el_interp, 'pchip');
end

% normalizing interpolated data:
norm_interp_Xwailemod = interp_Xwailemod./(max(
    interp_Xwailemod));
norm_interp_Owailemod = interp_Owailemod./(max(
    interp_Owailemod));

% Create radar beam pattern of same dimensions:
[E_UHF, Enorm_UHF] = radar_beampattern(32, 929.9e6,
    linspace(-pi/180, pi/180, n_interp));

% Empty array for deconvolved signal:
norm_deconv_Xwailes = zeros(n_interp, 42);
norm_deconv_Owailes = zeros(n_interp, 42);

% Running deconvolution of normalized X- and O-mode data
    over all range

```

```

% gates:
for i_z = 1:42
    [TX, SX] = deconvolution(norm_interp_Xwailemod(:, i_z)
        ), Enorm_UHF ');
    norm_deconv_Xwailes(:, i_z) = SX;

    [TO, SO] = deconvolution(norm_interp_0wailemod(:, i_z)
        ), Enorm_UHF ');
    norm_deconv_0wailes(:, i_z) = SO;
end

```

B.5 Ray tracing

ray_trace_v2.py contains the functions necessary to run a ray tracing simulation for a radio wave in a model ionosphere based on an IRI profile.

```

#!/usr/bin/env python
'''
Ionospheric radio propagation using simple ray-tracing

2019 Juha Vierinen

Minor modificiations made by Zoe Bazilchuk 2019
'''
from datetime import datetime
import matplotlib.pyplot as plt
import numpy as n
import scipy.integrate as si
import scipy.interpolate as sint
import scipy.constants as c
import coord
import pyglow

from mpl_toolkits.mplot3d import Axes3D

def iri_ne(alts=n.linspace(100,1000,num=200),
          lat=69.58,
          lon=19.23,
          dn=datetime(2014, 11, 27, 12, 00)):
    '''
    Get N_e profile from IRI.
    '''
    ne=n.zeros(len(alts))
    for ai,alt in enumerate(alts):
        pt = pyglow.Point(dn, lat, lon, alt)
        pt.run_iri()
        if pt.ne < 0.0:
            pt.ne=1.0
        ne[ai]=pt.ne*1e6 # m^-3
    return(ne)

```

```

def ne_irregularity(x, x0=0.0, d_s=0.1, ne0=1.0):
    """
    Create field aligned irregularities.
    """
    ne=n.zeros(x.shape)
    slope=ne0/d_s
    idx=n.where( ((x-x0)>=-d_s) & ((x-x0)<0.0))
    ne[idx]=slope*(x[idx]-x0) + ne0
    idx=n.where(((x-x0)>=0.0) & ((x-x0)<d_s))
    ne[idx]=-slope*(x[idx]-x0) + ne0
    return(ne)

def ne_depletion(x, x0=0.0, w=1.0, d_s=0.1, ne0=1.0):
    """
    Create field aligned irregularities.
    Depletion with linear gradients in walls
    """
    nefun=sint.interpld(n.array([-1e3,-w/2.0,-w/2.0+d_s,w/2.0-d_s,w
        /2.0,1e3])+x0,[0.0,0.0,ne0,ne0,0.0,0.0])
    ne=nefun(x)
    return(ne)

def ne_irregularity_gaussian(x, x0=0.0, d_s=0.1, ne0=1.0):
    """
    Create field aligned irregularities.
    """
    # ne=n.zeros(x.shape)
    ne=ne0*n.exp(-0.5*(x-x0)**2.0/d_s**2.0)
    return(ne)

def get_ionosphere(lat=69.58, lon=19.23, plot_ne=False, alts=n.linspace
(0,1000,num=200), x=n.linspace(-5,5,num=100000), x0s=n.array([0.0])
, d_s=0.5, depletion_size=1.0, d_ne=0.01):

    """
    Ionosphere in the field-aligned direction.
    lat - latitude
    lon - longitude
    plot_ne - display plots of density profile
    alt - range of altitudes to create
    x - horizontal range for ionosphere
    x0s - horizontal location of perturbations
    d_s - horizontal length scale of perturbations
    depletion_size - size of depletion
    d_ne - perturbation magnitude
    """
    n_alt=len(alts)
    n_x=len(x)
    ne=n.zeros([n_x,n_alt],dtype=n.float64)
    dne=n.zeros([n_x,n_alt],dtype=n.float64)
    x2=n.zeros([n_x,n_alt],dtype=n.float64)
    alts2=n.zeros([n_x,n_alt],dtype=n.float64)

    ne0=iri_ne(alts)*1.86
    fOF2 = n.max(n.sqrt((ne0*3182.107))/(2*n.pi))*1e-6

```

```

for xi in range(len(x)):
    x2[xi,:]=x[xi]
for ai in range(len(alts)):
    alts2[:,ai]=alts[ai]
    ne[:,ai]=ne0[ai]

for x0 in x0s:
    dne0=ne_depletion(x2,x0=x0,w=depletion_size,d_s=d_s,ne0=d_ne)
    dne+=dne0
dne=1.0-dne
ne=ne+ne*dne

if plot_ne:
    plt.subplot(121)
    plt.pcolormesh(x,alts,n.log10(n.transpose(ne)))
    plt.xlabel("Horizontal distance (km)")
    plt.ylabel("Altitude (km)")
    plt.title("$N_e$ (log10)")
    plt.colorbar()
    plt.subplot(122)
    plt.pcolormesh(x,alts,n.transpose(dne))
    plt.colorbar()
    plt.xlabel("Horizontal distance (km)")
    plt.ylabel("Altitude (km)")
    plt.title("$\Delta N_e$ (fraction)")
    plt.show()

return(ne,dne,alts,x,alts2,x2, fOF2)

def ne_interp(x,alt,ne,xs,alts):
    """
    Relatively easy and stable interpolation scheme based on distance
    to nearest four points.
    """
    x0=n.min(xs)
    x1=n.max(xs)
    a0=n.min(alts)
    a1=n.max(alts)
    dx=xs[1]-xs[0]
    da=alts[1]-alts[0]

    xi0=n.min((int(n.floor((x-x0)/dx)),len(xs)-1))
    xi1=n.min((int(n.ceil((x-x0)/dx)),len(xs)-1))
    ai0=n.min((int(n.floor((alt-a0)/da)),len(alts)-1))
    ai1=n.min((int(n.ceil((alt-a0)/da)),len(alts)-1))

    w0=1.0/(n.sqrt((x-xs[xi0])**2.0+(alt-alts[ai0])**2.0)+1e-6)
    w1=1.0/(n.sqrt((x-xs[xi1])**2.0+(alt-alts[ai1])**2.0)+1e-6)
    w2=1.0/(n.sqrt((x-xs[xi0])**2.0+(alt-alts[ai0])**2.0)+1e-6)
    w3=1.0/(n.sqrt((x-xs[xi1])**2.0+(alt-alts[ai1])**2.0)+1e-6)

    nei=(1.0/(w0+w1+w2+w3))*(w0*ne[xi0,ai0]+w1*ne[xi0,ai1]+w2*ne[xi1,
        ai0]+w3*ne[xi1,ai1])
    return(nei)

def ray_trace(ne,dne,alts,x,fOF2,f=929.9e6,dh=0.01,angle=0.3,
    output=True,plot=True):
    """

```

```

Propagate a radio wave using Snell's law in 2d
"""

#   nefun=sint.interp2d(x,alts,n.transpose(ne))

#   initial direction and position
k=n.array([n.sin(n.pi*angle/180.0),n.cos(n.pi*angle/180.0)])
#   position
p=n.array([0.0,1.0])

#   Taylor-expanded AH eqn:
ref_idx=n.sqrt(1-(8.98*n.sqrt(ne)/f)**2.0)
ref_hor_grad=n.zeros(ref_idx.shape)
for i in range(len(alts)):
    ref_hor_grad[:,i]= n.gradient(ref_idx[:,i],x)

#   plt.pcolormesh(x,alts,n.transpose(ref_hor_grad))
#   plt.colorbar()
#   plt.xlabel("Horizontal distance (km)")
#   plt.ylabel("Altitude (km)")
#   plt.title("dn/dx")
#   plt.show()

vg=1.0
ray_in_box=True

xmax=n.max(x)
xmin=n.min(x)
amax=n.max(alts)
amin=n.min(alts)

nes=[]
altss=[]
px=[]
py=[]

thetas=[]
grad_angs=[]

i=0
while ray_in_box:
    p=p+k*dh*vg

    # gradient
    dp_x=p+n.array([1.0,0.0])*0.001
    dp_y=p+n.array([0.0,1.0])*0.001

    # check bounds
    if p[0]>xmax or p[0]<xmin or p[1]>amax or p[1] < amin:
        ray_in_box=False
        break

    # append to position list
    px.append(p[0])
    py.append(p[1])

    # ne at current position
#   ne0=nefun(p[0],p[1])[0]

```

```

ne0=ne_interp(p[0],p[1],ne,x,alts)

#   nedx=nefun(dpx[0],dpx[1])[0]
nedx=ne_interp(dpx[0],dpx[1],ne,x,alts)
#   nedy=nefun(dpy[0],dpy[1])[0]
nedy=ne_interp(dpy[0],dpy[1],ne,x,alts)

# derivative of ne
dne_dx=(nedx-ne0)/dh
dne_dy=(nedy-ne0)/dh
ne_grad=n.array([dne_dx,dne_dy])

# gradient unit vector
if n.linalg.norm(ne_grad) > 1e-99:
    ne_grad0=ne_grad/n.linalg.norm(ne_grad)
else:
    ne_grad0=n.array([0.0,1.0])

grad_angs.append(n.arctan(ne_grad0[1]/ne_grad0[0]))
# ne at displacement
p1 = p + ne_grad0*dh
#   nel=nefun(p1[0],p1[1])[0]
nel=ne_interp(p1[0],p1[1],ne,x,alts)

# refractive index on one side of the "interface"
fp0=8.98*n.sqrt(ne0)
fp1=8.98*n.sqrt(nel)
# refractive index on both sides of the interface
n0=n.sqrt(1.0-(fp0/f)**2)
n1=n.sqrt(1.0-(fp1/f)**2)

# angle between k-vector and gradient
theta0=n.arccos(n.dot(ne_grad0,k))
thetas.append(theta0)

# make sure angle is not more than 90 degrees
if theta0 > n.pi/2.0:
    theta0=n.pi-theta0

# figure out
sin_theta_1=(n0/n1)*n.sin(theta0)
cos_theta_1=n.sqrt(1.0-sin_theta_1**2.0)
k_ref=(n0/n1)*k-((n0/n1)*n.cos(theta0)-cos_theta_1)*ne_grad0

# normalize k-vector
k_try=k_ref/n.sqrt(n.dot(k_ref,k_ref))
if not n.isnan(k_try[0]):
    k=k_try
if i%1000 == 0:
    if output == True:
        print("altitude: %1.1f km horizontal position: %1.1f km
              angle %1.1f fOF2 %1.1f"%(p[1], p[0], angle, fOF2))
nes.append(ne0)
i+=1

px=n.array(px)
py=n.array(py)
nes=n.array(nes)

```

```

thetas=n.array(thetas)
grad_langs=n.array(grad_langs)

plt.rcParams.update({'font.size': 8})
plt.figure()
plt.subplot(121)
plt.pcolormesh(x,alts,n.transpose(dne))
plt.colorbar()
plt.xlabel("Horizontal distance (km)")
plt.ylabel("Altitude (km)")
plt.title("$\Delta N_e/N_e$, fOF2 = %1.1f MHz"%(fOF2))
plt.plot(px,py,color="white", alpha = 0.8, linewidth=3)

plt.subplot(122)
plt.pcolormesh(x,alts,n.transpose(ref_hor_grad))
plt.colorbar()
plt.xlabel("Horizontal distance (km)")
#plt.ylabel("Altitude (km)")
plt.yticks([])
plt.title("$dn/dx$ Horizontal gradient of refractive index")
plt.plot(px,py,color="white", alpha = 0.8, linewidth = 3)

if plot == True:
    plt.show()

return px, py, nes, thetas, grad_langs

"""
# create ionosphere with 50 meter standard deviation horizontal scale
# gaussian field aligned irregularities
# and 5% of background density perturbations
ne,dne,alts,x,alts2,x2=get_ionosphere(d_ne=0.1, d_s=0.1)

angs=[0.2,0.3,0.4,0.5,0.6,0.7]
for a in angs:
    ray_trace(ne,dne,alts,x,dh=0.005,angle=a) # ray-trace with 5 meter
        step size and a deg launch angle
"""

```

raytraceallthethings.py compiles the simulation in ray_trace_v2.py and makes changing input parameters a bit simpler.

```

#!/usr/bin/env python
from datetime import datetime
import matplotlib.pyplot as plt
import numpy as n
import scipy.integrate as si
import scipy.interpolate as sint
import scipy.constants as c
from mpl_toolkits.mplot3d import Axes3D
import h5py
import coord
import pyglow
from ray_trace_v2 import *

"""
# for no striations:

```

```

ne, dne, alts, x, alts2, x2 = get_ionosphere(d_s = 0.0, depletion_size
    = 0.0, d_ne = 0.0)
# Between -1 and +1 degree of zenith:
for a in n.linspace(-1.0, 1.0, 5):
    ray_trace(ne, dne, alts, x, angle = a, plot = False)
plt.show()
"""
#0.01, 0.02, 0.03, 0.04, 0.05, 0.06, 0.07, 0.08, 0.09,
ne, dne, alts, x, alts2, x2, fOF2 = get_ionosphere(x0s = n.linspace
    (-5.0, 5.0, 10), d_s = 0.5, d_ne = 0.11)
a = [0.3, 0.4, 0.5, 0.6, 0.7]
for ang in a:
    ray_trace(ne, dne, alts, x, fOF2, dh = 0.01, angle = ang, output =
        True, plot = False)
    info = 'finalfinalfof210@010angle%s' %str(ang)
    plt.savefig("%s.png" % info)
    #plt.show()

"""
hf = h5py.File("%s" % info, "w")
hf["ne"] = ne
hf["dne"] = dne
hf["x"] = px
hf["y"] = py
hf["theta"] = thetas
hf["grad_angs"] = grad_angs
hf.close()
"""

```

Bibliography

- [Bjørnå, 2005] Bjørnå, N. (2005). Lecture notes in agf-304 radar diagnostics of space plasma. Course compendium in FYS-3002 at UIT.
- [Blagoveshchenskaya et al., 2018] Blagoveshchenskaya, N. F., Borisova, T. D., Kalishin, A. S., Kayatkin, V. N., Yeoman, T. K., and Häggström, I. (2018). Comparison of the effects induced by the ordinary (o-mode) and extraordinary (x-mode) polarized powerful hf radio waves in the high-latitude ionospheric f region. *Cosmic Research*, 56(1):11–25.
- [Blagoveshchenskaya et al., 2014] Blagoveshchenskaya, N. F., Borisova, T. D., Kosch, M., Sergienko, T., Brändström, U., Yeoman, T. K., and Häggström, I. (2014). Optical and ionospheric phenomena at eiscat under continuous x-mode hf pumping. *Journal of Geophysical Research: Space Physics*, 119(12):10,483–10,498.
- [Blagoveshchenskaya et al., 2011a] Blagoveshchenskaya, N. F., Borisova, T. D., Rietveld, M. T., Yeoman, T. K., Wright, D. M., Rother, M., Lühr, H., Mishin, E. V., and Roth, C. (2011a). Results of russian experiments dealing with the impact of powerful hf radiowaves on the high-latitude ionosphere using the eiscat facilities. *Geomagnetism and Aeronomy*, 51(8):1109–1120.
- [Blagoveshchenskaya et al., 2011b] Blagoveshchenskaya, N. F., Borisova, T. D., Yeoman, T. K., Rietveld, M. T., Ivanova, I. M., and Baddeley, L. J. (2011b). Artificial small-scale field-aligned irregularities in the high latitude f region of the ionosphere induced by an x-mode hf heater wave. *Geophysical Research Letters*, 38(8).
- [Brekke, 2013] Brekke, A. (2013). *Physics of the upper polar atmosphere*. Springer.
- [Bryers et al., 2013] Bryers, C. J., Kosch, M. J., Senior, A., Rietveld, M. T., and Singer, W. (2013). A comparison between resonant and nonresonant heating at EISCAT. *Journal of Geophysical Research (Space Physics)*, 118:6766–6776.
- [Chen, 2006] Chen, F. (2006). *Introduction to Plasma Physics and Controlled Fusion: Volume 1: Plasma Physics*. Introduction to Plasma Physics and Controlled Fusion. Springer US.
- [Chisham et al., 2007] Chisham, G., Lester, M., Milan, S. E., Freeman, M. P., Bristow, W. A., Grocott, A., McWilliams, K. A., Ruohoniemi, J. M., Yeoman, T. K., Dyson, P. L., Greenwald, R. A., Kikuchi, T., Pinnock, M., Rash, J. P. S., Sato, N., Sofko, G. J., Villain, J.-P., and Walker, A. D. M. (2007). A decade of the super dual auroral radar network (superdarn): scientific achievements, new techniques and future directions. *Surveys in Geophysics*, 28(1):33–109.

- [D'Arrico, 2012a] D'Arrico, J. (2012a). `fminsearchbnd` matlab function. Retrieved from <https://se.mathworks.com/matlabcentral/fileexchange/8277-fminsearchbnd-fminsearchcon> Jan. 2019.
- [D'Arrico, 2012b] D'Arrico, J. (2012b). `inpaint_nans` matlab function. Retrieved from https://se.mathworks.com/matlabcentral/fileexchange/4551-inpaint_nans?s_tid=srchtitle Jan. 2019.
- [Davies, 1990] Davies, K. (1990). *Ionospheric Radio*. Electromagnetics and Radar Series. Peregrinus.
- [Duly, 2016] Duly, T. (2016). `Pyglow`, upper atmospheric climatological model library for python. Installed from <https://github.com/timduly4/pyglow> Jan. 2019.
- [Frolov et al., 1997] Frolov, V., Erukhimov, L., Metelev, S., and Sergeev, E. (1997). Temporal behaviour of artificial small-scale ionospheric irregularities: review of experimental results. *Journal of Atmospheric and Solar-Terrestrial Physics*, 59(18):2317–2333.
- [Gurevich et al., 2002] Gurevich, A., Fremouw, E., Secan, J., and Zybin, K. (2002). Large scale structuring of plasma density perturbations in ionospheric modifications. *Physics Letters A*, 301(3):307 – 314.
- [Gustavsson and Eliasson, 2008] Gustavsson, B. and Eliasson, B. (2008). Hf radio wave acceleration of ionospheric electrons : Analysis of hf-induced optical enhancements. *Journal of Geophysical Research: Space Physics*, 113(A8).
- [Gustavsson et al., 2010] Gustavsson, B., Rietveld, M. T., Ivchenko, N. V., and Kosch, M. J. (2010). Rise and fall of electron temperatures: Ohmic heating of ionospheric electrons from underdense hf radio wave pumping. *Journal of Geophysical Research: Space Physics*, 115(A12).
- [Huxley and Ratcliffe, 1949] Huxley, L. G. H. and Ratcliffe, J. A. (1949). A survey of ionospheric cross-modulation (wave interaction or luxembourg effect). *Proceedings of the IEE - Part III: Radio and Communication Engineering*, 96(43):433–440.
- [Inan and Gołkowski, 2010] Inan, U. S. and Gołkowski, M. (2010). *Principles of Plasma Physics for Engineers and Scientists*. Cambridge University Press.
- [Kalkan, 2017] Kalkan, D. E. (2017). `deconvolution` matlab function. Retrieved from https://se.mathworks.com/matlabcentral/fileexchange/60644-deconvolution-of-two-discrete-time-signals-in-frequency-domain?s_tid=mwa_osa_a May 2019.
- [Kelley et al., 1995] Kelley, M. C., Arce, T. L., Salowey, J., Sulzer, M., Armstrong, W. T., Carter, M., and Duncan, L. (1995). Density depletions at the 10-m scale induced by the arcibo heater. *Journal of Geophysical Research: Space Physics*, 100(A9):17367–17376.
- [Lagarias et al., 1998] Lagarias, J., Reeds, J., Wright, M., and Wright, P. (1998). Convergence properties of the nelder–mead simplex method in low dimensions. *SIAM Journal on Optimization*, 9(1):112–147.

- [Lehtinen and Häggström, 1987] Lehtinen, M. S. and Häggström, I. (1987). A new modulation principle for incoherent scatter measurements. *Radio Science*, 22(4):625–634.
- [Lehtinen and Huuskonen, 1996] Lehtinen, M. S. and Huuskonen, A. (1996). General incoherent scatter analysis and guisdap. *Journal of Atmospheric and Terrestrial Physics*, 58(1):435 – 452. Selected papers from the sixth international Eiscat Workshop.
- [Leyser, 2001] Leyser, T. (2001). Stimulated electromagnetic emissions by high-frequency electromagnetic pumping of the ionospheric plasma. *Space Science Reviews*, 98(3):223–328.
- [Mahafza, 2000] Mahafza, B. R. (2000). Radar systems analysis and design using matlab, © 2000 by chapman & hall.
- [Rietveld et al., 1993] Rietveld, M., Kohl, H., Kopka, H., and Stubbe, P. (1993). Introduction to ionospheric heating at tromsø—i. experimental overview. *Journal of atmospheric and terrestrial physics*, 55(4-5):577–599.
- [Rietveld et al., 2008] Rietveld, M., Wright, J., Zobotin, N., and Pitteway, M. (2008). The tromsø dynasonde. *Polar Science*, 2(1):55–71.
- [Rietveld et al., 2003] Rietveld, M. T., Kosch, M. J., Blagoveshchenskaya, N. F., Kornienko, V. A., Leyser, T. B., and Yeoman, T. K. (2003). Ionospheric electron heating, optical emissions, and striations induced by powerful hf radio waves at high latitudes: Aspect angle dependence. *Journal of Geophysical Research: Space Physics*, 108(A4).
- [Rietveld and Senior, 2019] Rietveld, M. T. and Senior, A. (2019). Ducting of incoherent scatter radar signals by field aligned irregularities. Manuscript in preparation.
- [Rietveld et al., 2016] Rietveld, M. T., Senior, A., Markkanen, J., and Westman, A. (2016). New capabilities of the upgraded eiscat high-power hf facility. *Radio Science*, 51(9):1533–1546.
- [Rishbeth and Van Eyken, 1993] Rishbeth, H. and Van Eyken, A. (1993). Eiscat: early history and the first ten years of operation. *Journal of atmospheric and terrestrial physics*, 55(4-5):525–542.
- [Robinson, 1989] Robinson, T. (1989). The heating of the high latitude ionosphere by high power radio waves. *Physics Reports*, 179(2):79 – 209.
- [Schunk and Nagy, 2009] Schunk, R. and Nagy, A. (2009). *Ionospheres: Physics, Plasma Physics, and Chemistry*. Cambridge Atmospheric and Space Science Series. Cambridge University Press, 2 edition.
- [Senior et al., 2013] Senior, A., Rietveld, M. T., Häggström, I., and Kosch, M. J. (2013). Radio-induced incoherent scatter ion line enhancements with wide altitude extents in the high-latitude ionosphere. *Geophysical Research Letters*, 40(9):1669–1674.

- [Shoucri et al., 1984] Shoucri, M. M., Morales, G., and Maggs, J. (1984). Ohmic heating of the polar f region by hf pulses. *Journal of Geophysical Research: Space Physics*, 89(A5):2907–2917.
- [Stocker et al., 1992] Stocker, A., Honary, F., Robinson, T., Jones, T., Stubbe, P., and Kopka, H. (1992). Eiscat observations of large scale electron temperature and electron density perturbations caused by high power hf radio waves. *Journal of Atmospheric and Terrestrial Physics*, 54(11):1555 – 1572.
- [Stubbe, 1996a] Stubbe, P. (1996a). Review of ionospheric modification experiments at tromsø. *Journal of Atmospheric and Terrestrial Physics*, 58(1-4):349–368.
- [Stubbe, 1996b] Stubbe, P. (1996b). Review of ionospheric modification experiments at tromsø. *Journal of Atmospheric and Terrestrial Physics*, 58(1):349 – 368. Selected papers from the sixth international Eiscat Workshop.
- [Tellegen, 1933] Tellegen, B. D. H. (1933). Interaction between radio-waves? *Nature*, 131:840 EP –.
- [Thidé et al., 1983] Thidé, B., Derblom, H., Hedberg, Kopka, H., and Stubbe, P. (1983). Observations of stimulated electromagnetic emissions in ionospheric heating experiments. *Radio Science*, 18(6):851–859.
- [Tjulin, 2015] Tjulin, A. (2015). *EISCAT Experiments*. EISCAT Scientific Association. available at https://www.eiscat.se/wp-content/uploads/2019/04/Experiments_v20181205.pdf.
- [Vierinen, 2019] Vierinen, J. (2019). Python ray tracing program. Provided for use in this project by Dr. Vierinen.